ANISOTROPY IN THE ALASKA SUBDUCTION ZONE: SHEAR-WAVE SPLITTING OBSERVATIONS FROM LOCAL AND TELESEISMIC EARTHQUAKES

By

Cole Richards, B.S.

A Thesis Submitted in Partial Fulfillment of the Requirements

for the Degree of

Master of Science

in

Geophysics

University of Alaska Fairbanks

May 2020

APPROVED:

Dr. Carl Tape, Committee Chair
Dr. Michael West, Committee Member
Dr. Jeffrey Freymueller, Committee Member
Dr. Paul McCarthy, Chair
Department of Geosciences
Dr. Kinchel C. Doerner, Dean
College of Natural Science and Mathematics
Dr. Michael Castellini, *Dean of the Graduate School*

Abstract

Shear-wave splitting observations can provide insight to mantle flow due to the link between the deformation of mantle rocks and their direction dependent seismic wave velocities. We identify shear-wave anisotropy in the Cook Inlet segment of the Alaska subduction zone by analyzing splitting parameters of S phases from local intraslab earthquakes between 50 and 200 km depths and SKS waves from teleseismic events. These earthquakes were recorded from 2015–2017 (local S) and 2007–2017 (SKS) by stations from SALMON (Southern Alaska Lithosphere and Mantle Observation Network), TA (EarthScope Transportable Array), MOOS (Multidisciplinary Observations Of Subduction), AVO (Alaska Volcano Observatory), and the permanent network. Automatic phase picking (dbshear) of 12095 local earthquakes ($M_l \geq 1.5$) recorded at 84 stations yielded 678 high-quality splitting measurements (filtered 0.2–1 Hz). Teleseismic SKS phases recorded at 112 stations with 26,143 event–station pairs resulted in 360 high-quality SKS splitting measurements (filtered 0.02–1 Hz and 0.01–1 Hz). Measurements for both datasets were made using the SC91 minimum eigenvalue method with software package MFAST. We compare local S and SKS splitting patterns both from previous studies and our own analysis and find that they are most similar in the far forearc, at the Kenai Peninsula, below which there is no mantle wedge. Anisotropy in the subducting Pacific lithosphere and subslab asthenosphere is likely here as both S and SKS display plate convergence fast directions and SKS measurements exhibit delay times too long (~2 s) to be explained solely by lithospheric anisotropy. Large splitting delay times (~0.5 s) for local measurements that mainly sample slab further indicate that the Pacific slab lithosphere contains significant anisotropy. We also observe anisotropy in the mantle wedge indicated by an increase in delay time as focal depth increases for stations with ray paths dominantly sampling wedge. These measurements display trench-perpendicular and plate convergence fast directions consistent with 2D corner flow in the mantle wedge. Both datasets show trench-parallel splitting directions in select areas of the arc/forearc that overlie parts of the mantle wedge and nose. B-type olivine in the mantle nose, subslab asthenospheric flow, flow around the slab edge, and anisotropy in the Pacific lithosphere all could be invoked to explain this pattern. While we are unable to distill the anisotropy to a single responsible structure, the sharp transition in the local S data splitting pattern from trench-perpendicular in the backarc to trench-parallel across the arc suggests B-type olivine in the mantle nose. For an overall model, we favor 2D corner flow of A-type olivine in the mantle wedge induced by downdip motion of the slab, B-type olivine in the nose, and plate convergence parallel anisotropy in the subslab asthenosphere and subducting Pacific lithosphere to explain the observed splitting patterns. It is clear that the subducting slab's structure and motion are the dominant influence on anisotropy and mantle flow regimes here. The differences in local S and SKS

splitting results motivate further study on frequency dependence of splitting measurements and emphasize the need for a better understanding of which earth structures are responsible for the observed splitting patterns globally. This study constitutes the first comprehensive local splitting study in Alaska and refutes the common interpretation of along arc flow in the mantle wedge proposed by many previous splitting studies in Alaska.

Table of Contents

List of Figures

Page

List of Tables

Page

Acknowledgements

First and foremost I would like to thank Dr. Carl Tape for the providing me with this tremendous opportunity. I would also like to thank my committee members Dr. Michael West and Dr. Jeff Freymueller for their support and teachings. I thank Marta Savage for developing a user-friendly splitting code. I thank all of those involved in the seismic data collection that was utilized in this study. I owe a thank you to all of the Alaska Earthquake Center employees for the behind the scenes view of operations that I gained while working at the Geophysical Institute. I also owe a big thank you to the state of Alaska and its fascinating tectonic settings. Finally, I would like to thank my brother, father, and mother for their lifelong support.

This thesis will use the word "we" in reference to the authors of a manuscript expected to be submitted: Cole Richards, Carl Tape, and Zach Ross. We also acknowledge contributions from committee members. I developed the required scripts to process, organize, and plot the data for interpretation and I wrote this document. Dr. Zach Ross supported this work by providing picks for P and S waves for the entire local dataset. Carl Tape guided the direction of the science, motivated me, and provided many scripts and scientific tools to aid this study.

Chapter 1
General Introduction

Geodynamic processes occurring in Earth's mantle play an important in role in current tectonic behaviors and continued evolution of our planet. Mantle dynamics such as deformation, flow, and interaction with overriding plates are not well understood to this day. Our lack of understanding is largely because we are limited to indirect geophysical observations as the mantle is too deep to sample directly. We can examine exhumed mantle rocks on the surface but in order to probe the mantle in its current state and location, seismic waves provide the most direct observations available. Deformation of mantle rocks can lead to the development of elastic anisotropy and thus by carefully studying the signal of seismic waves that traverse through anisotropic regions of the mantle we can investigate its dynamics.

Shear-wave splitting is probably the most unequivocal expression of anisotropy in seismic data and is analogous to birefringence in optical physics. When a shear wave propagates through a seismically anisotropic structure, it splits into two orthogonal phases that travel at different velocities (Silver & Chan, 1991). These two phases can be recorded at a seismic station and a splitting measurement can be made in attempt to characterize the anisotropy that split the wave. Unlike other methods used to study anisotropy, it is a single-station measurement. A shear-wave splitting measurement consists of two parameters that relate to the orientation and strength of anisotropy that the shear wave encountered. These two parameters are the polarization of the fast phase (ϕ) and the separation in time between the two split phases (δt). Early studies (Keith & Crampin, 1977; Ando et al., 1983; Silver & Chan, 1988) paved the way for splitting to become a popular method for probing anisotropic structures in various regions of the Earth. Specifically, subduction zones are among the most common settings where splitting studies have been focused, due to the expected strong signature of mantle deformation and slab seismicity.

Shear waves produced by local intraslab earthquakes and teleseismic SKS phases travel through various parts of the subduction system and therefore both lend themselves well to studying seismic anisotropy in subduction zones (Figure 1.1). In the case of SKS splitting the path spans the entire mantle with maximum sensitivity of the measurement to structure that is above, within, and below the slab making depth constraints difficult (Sieminski et al., 2008; Long et al., 2008). Local splitting can aid in constraining depth because path is directly between the earthquake and the overlying station (usually within 200 km) and intraslab earthquakes occur at a range of depths. For example, local S and SKS splitting sensitivity kernels are shown in Figure 1.2 and Figure 1.3, respectively. Therefore, when characterizing a subduction system's anisotropic structures it is advantageous to include both phases in the splitting analysis.

Anisotropy in the upper mantle is often attributed to lattice preferred orientation (LPO) of mantle olivine (Karato et al., 2008). When olivine is strained, its crystallographic fast axes can become aligned parallel to (A-type or similar) or orthogonal to (B-type) the direction of maximum strain (Kneller et al., 2005). Anisotropy from LPO in the mantle wedge and subslab asthenosphere are the most commonly cited anisotropic structures in subduction zones (Long & Silver, 2009). Splitting patterns in subduction zones around the the globe show a high amount of variability (Long & Wirth, 2013). This has led to several different models of subduction processes and mantle flow being invoked to explain the observed splitting patterns (Figure 1.4). The seemingly contradicting splitting patterns, interpreted anisotropic structures, and mantle flow models prompts questions regarding what controls anisotropy and mantle flow and whether simple subduction cartoon models do well to predict the range patterns observed globally.

In the furthest north stretches of the Pacific ocean, the Pacific plate subducts beneath the North American plate creating the Aleutian-Alaska subduction zone. Mainland Alaska overlies the eastern end of this 3000 km-long subduction zone, which exhibits changes along strike in convergence geometry, slab dip, and plate structure (Fournelle et al., 1994). The easternmost 500 km contains the Cook Inlet segment, which has a steeply dipping slab and robust volcanic arc and the Denali segment which exhibits "flat" slab subduction and has nearly no volcanic arc (Figure 1.5). The geometry of subduction in Cook Inlet is shown in Figure 1.6.

In the Alaska subduction zone, SKS splitting studies have shown a profound and sharp transition in fast directions from trench-parallel in the backarc to trench-perpendicular in the forearc and beyond (Figure 1.7). These patterns have been attributed to trench-parallel flow in the backarc mantle wedge and subslab asthenospheric flow beneath and/or fossil anisotropy within the subducting oceanic lithosphere (Christensen & Abers, 2010; Perttu et al., 2014; McPherson et al., 2017; Venereau et al., 2019; Hanna & Long, 2012) (Figure 1.8). However, Song & Kawakatsu (2013) suggested instead that both patterns can be explained solely by asthenospheric flow beneath the subducting oceanic lithosphere (Figure 1.9). Furthermore, Jadamec & Billen (2010) and Venereau et al. (2019) proposed 3D corner flow around the slab edge from geodynamic modeling and SKS splitting, respectively (Figure 1.10 and Figure 1.11). Of the local splitting studies in Alaska (Wiemer et al., 1999; Christensen et al., 2003; Hacker & Abers, 2012; Yang et al., 1995), none provide much insight into the various interpreted models as they all lack large data sets. Wiemer et al. (1999) is the only study in Cook Inlet and used only 3 stations. Finally, independent of seismic studies, Mehl et al. (2003) used fabrics from exhumed mantle rocks found in the accreted Talkeetna arc of south central Alaska to advocate for along arc flow in the mantle wedge with an exotic olivine slip system.

The competing models of anisotropy and mantle flow for the Alaska subduction zone and the lack of a comprehensive local splitting analysis greatly incentivizes a local splitting study to be conducted here. In this thesis, we aim to provide new constraints and further clarity on mantle dynamics and subduction processes occurring in the Alaska subduction zone by performing three main tasks:

1. Shear-wave splitting analysis of both local S waves from intraslab earthquakes and SKS waves from teleseismic earthquakes
2. Ray tracing for discerning which anisotropic signals belong to which structures.
3. Combining our observations with previous studies to depict a subduction system model that best explains the various datasets.

1.1 Figures

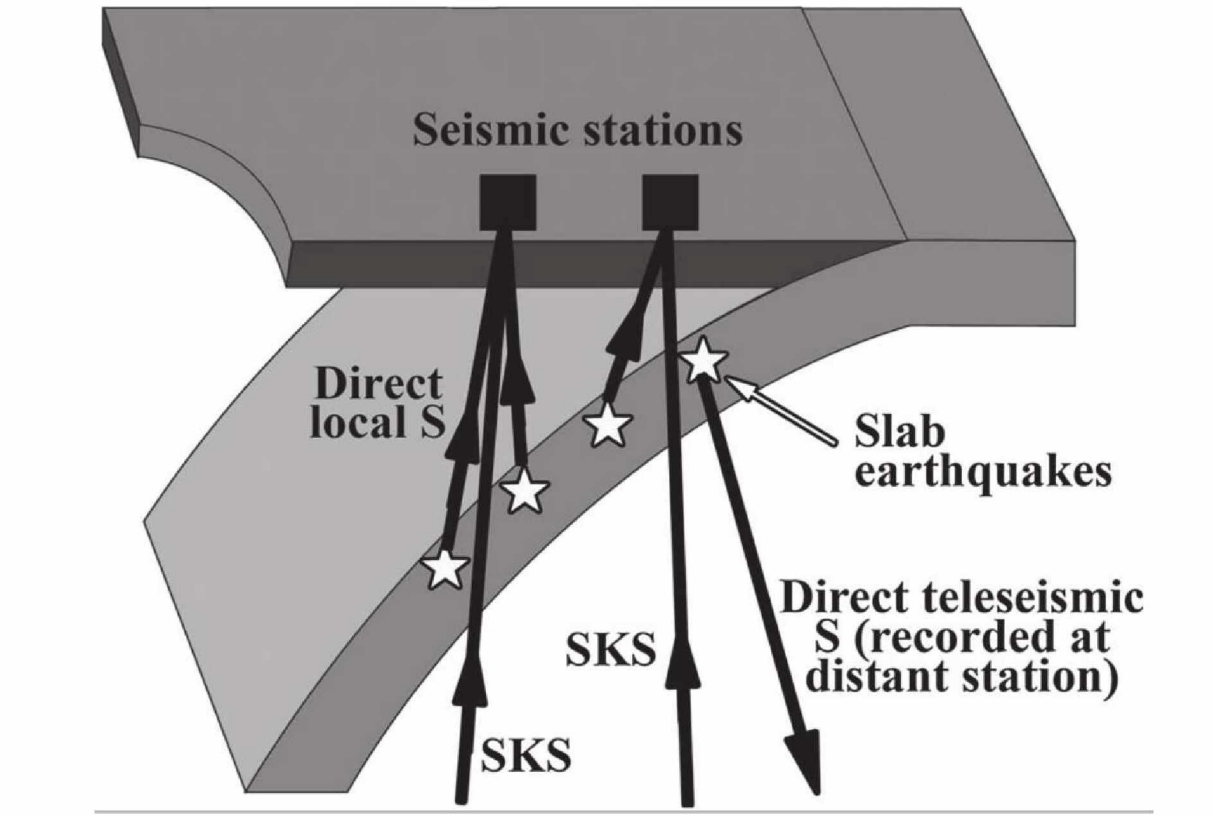

Figure 1.1: Figure from Long (2013) displaying local S and SKS ray paths in a subduction zone.

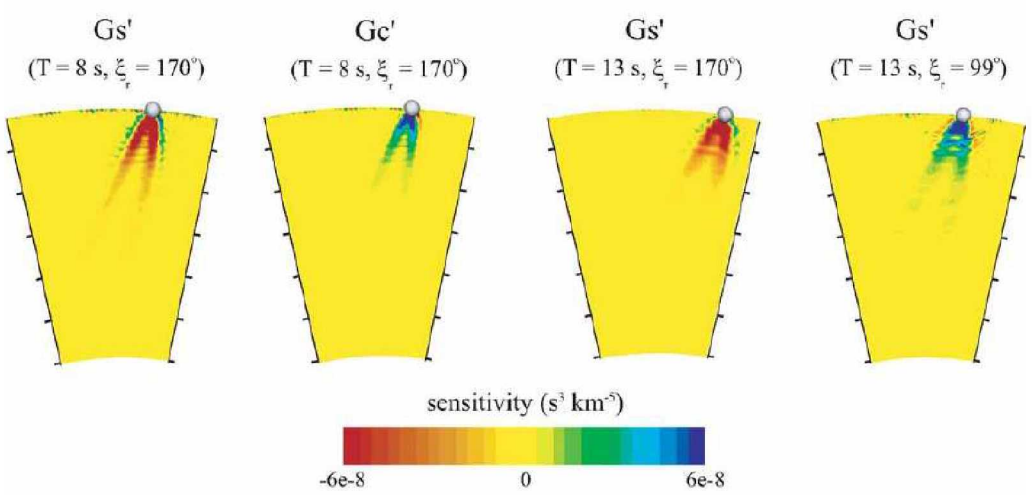

Figure 1.2: Figure from Sieminski et al. (2008) displaying SKS-splitting sensitivity. The depth tick marks are situated every 500km from the core mantle boundary to the surface. The two closest tick mark to the surface are 400 km and 900 km depth, respectively.

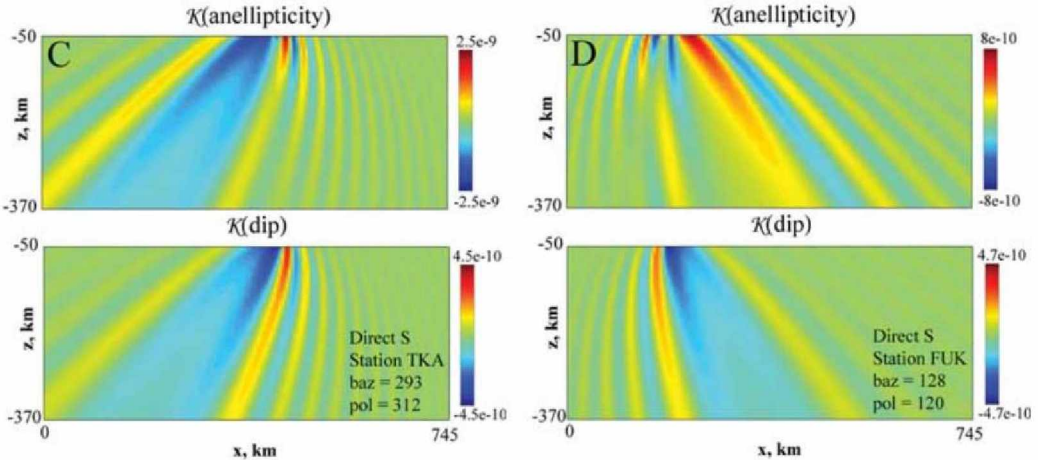

Figure 1.3: Figure from Long et al. (2008) displaying S-splitting sensitivity. Note that this is for an especially deep slab earthquake in Tonga. Most intraslab events will have shallower depths and thus will not be sensitive to these large depths.

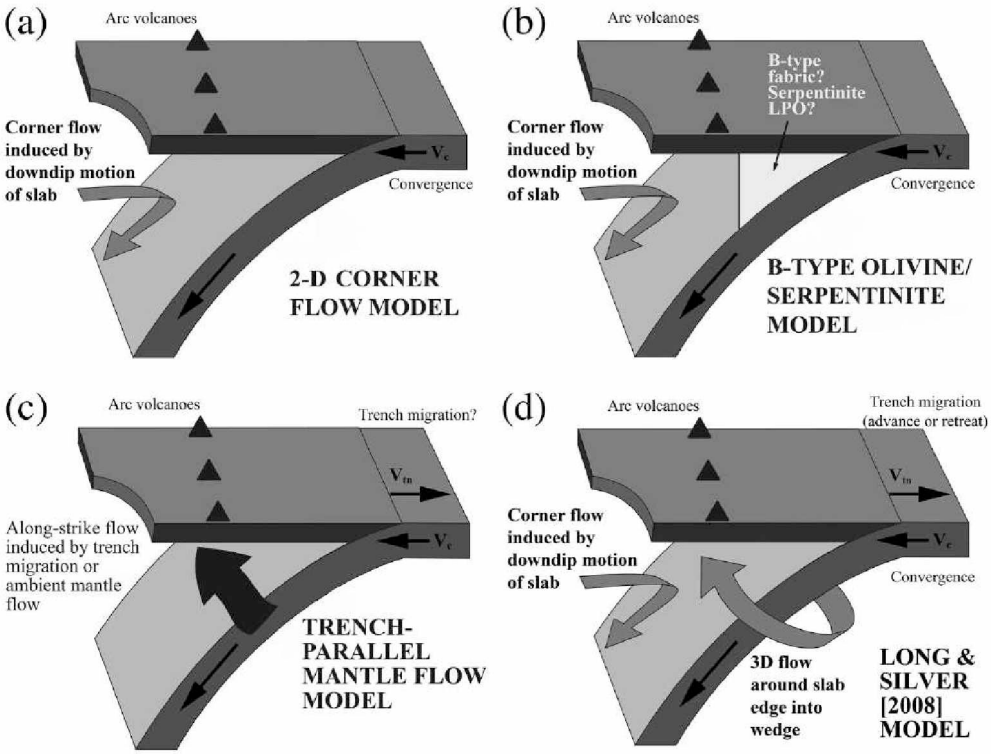

Figure 1.4: Cartoon sketches for commonly invoked models used to explain splitting patterns in subduction zones from Long & Wirth (2013).

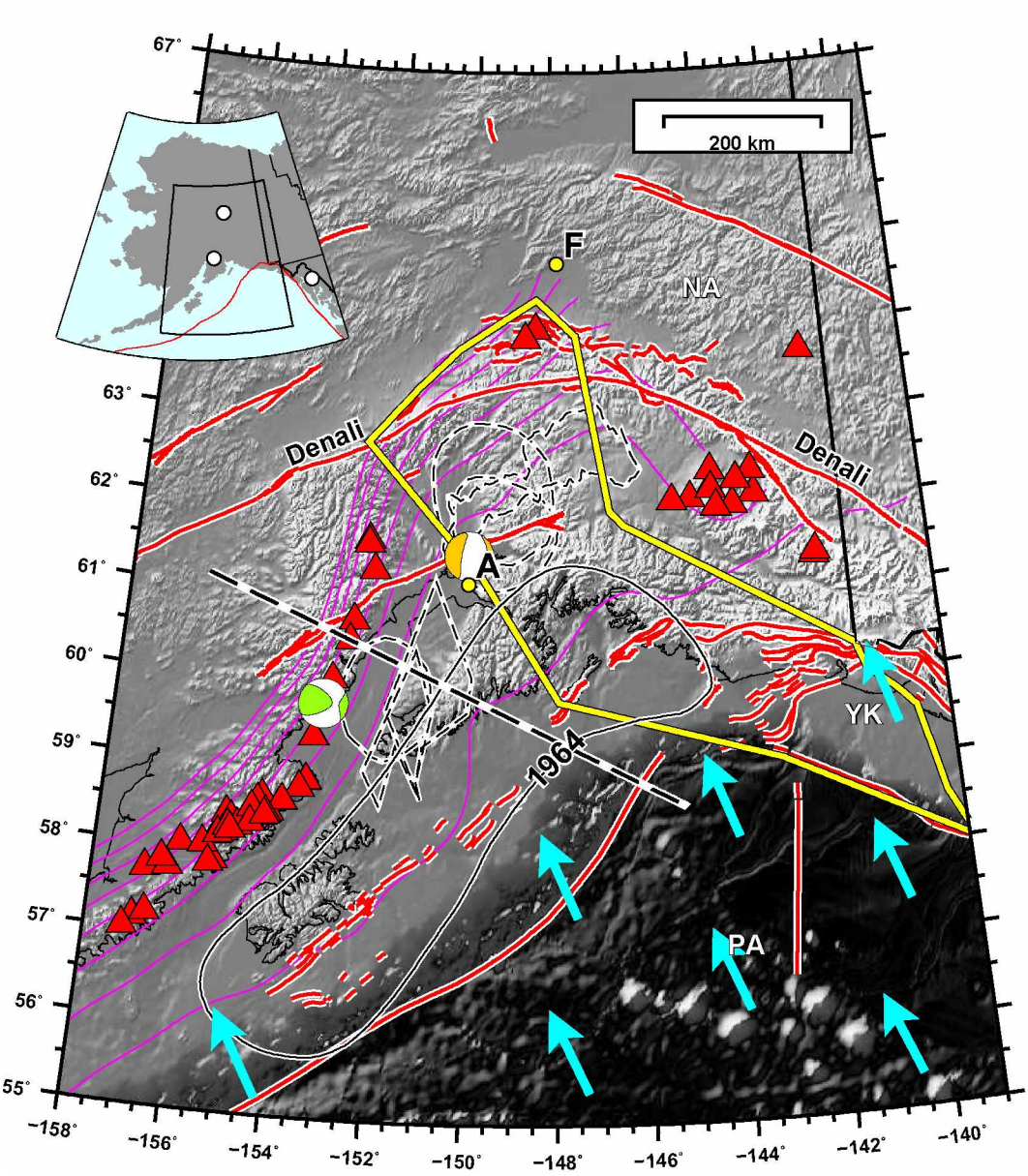

Figure 1.5: Active tectonic setting of the Aleutian-Alaskan subduction zone, south-central Alaska. Cyan arrows show the plate vectors for the subducting Pacific plate (PA) under the North American plate (Argus et al., 2011). Red lines denote active faults (Koehler et al., 2012). Magenta curves are the 40 km to 200 km contours of the subduction interface, i.e., the top of the Pacific plate (Hayes et al., 2018). Yellow bounded region denotes the surface and subsurface extent of the Yakutat block (YK) (Eberhart-Phillips et al., 2006). Red triangles represent active volcanoes. Black dashed lines are inferred slow slip events from various sources (Ohta et al., 2006; Wei et al., 2012; Fu & Freymueller, 2013; Li et al., 2016). Green and white beachball is the seismic moment tensor of the January 24, 2016 M_w7.1 Iniskin earthquake. Yellow and white beachball is the seismic moment tensor of the November 30, 2018 M_w7.1 Anchorage earthquake. Also marked is the aftershock zone of the 1964 M_w9.2 earthquake. Black and white dashed line marks the cross section in Figure 2.5.

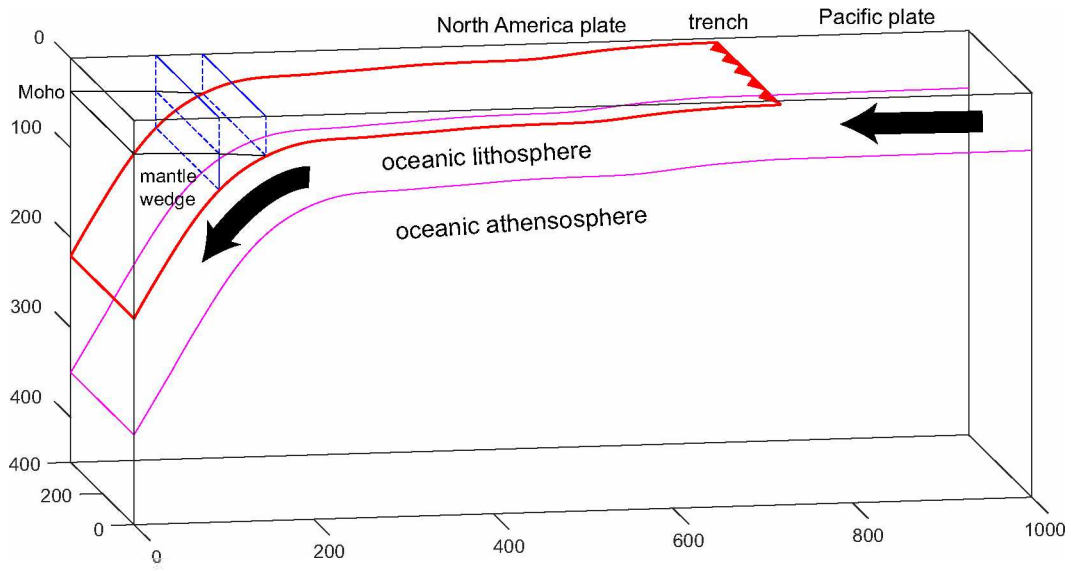

Figure 1.6: Cross section of the Cook Inlet segment of the Alaska subduction zone. Cross section line is shown in Figure 1.5. The slab geometry is slab2.0 (Hayes et al., 2018). The continental Moho is from Miller & Moresi (2018). Components of the subduction system are labeled. The black arrows depict that the Pacific plate is subducting beneath the North American plate.

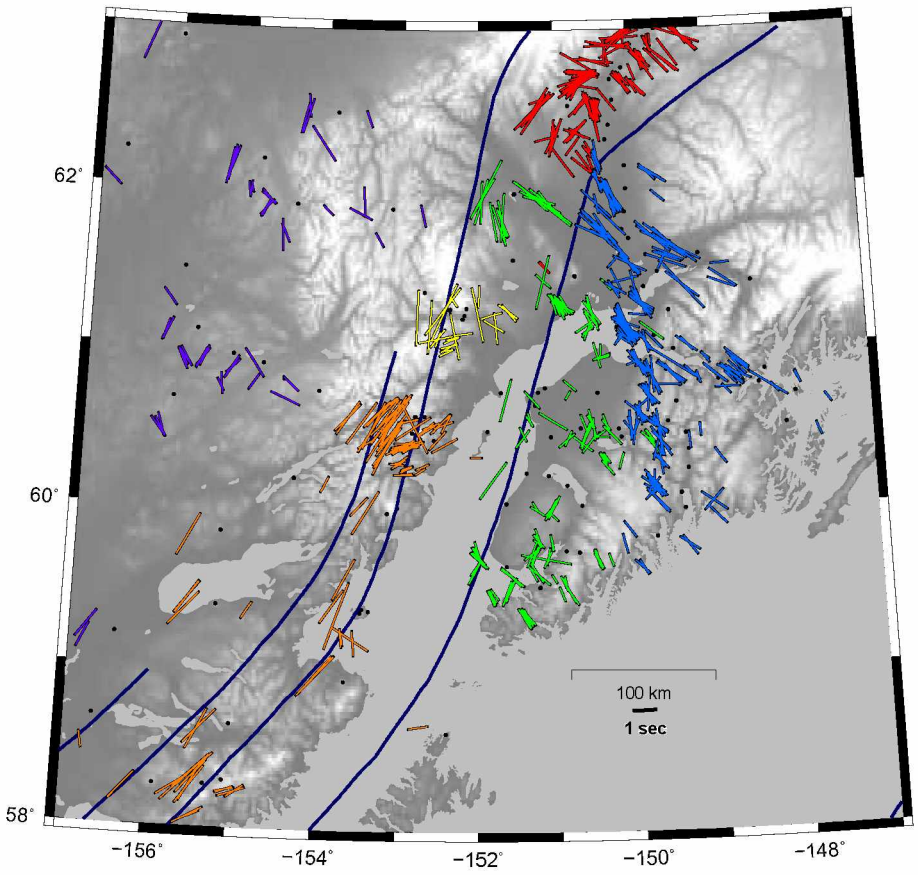

Figure 1.7: McPherson et al. (2017); Christensen & Abers (2010); Perttu et al. (2014) SKS splitting observations plotted at the 100 km projection of the rays paths. The thick blue lines show the depth of the subducting slab at 50, 100, 150, and 200 km depth. Dots indicate station locations.

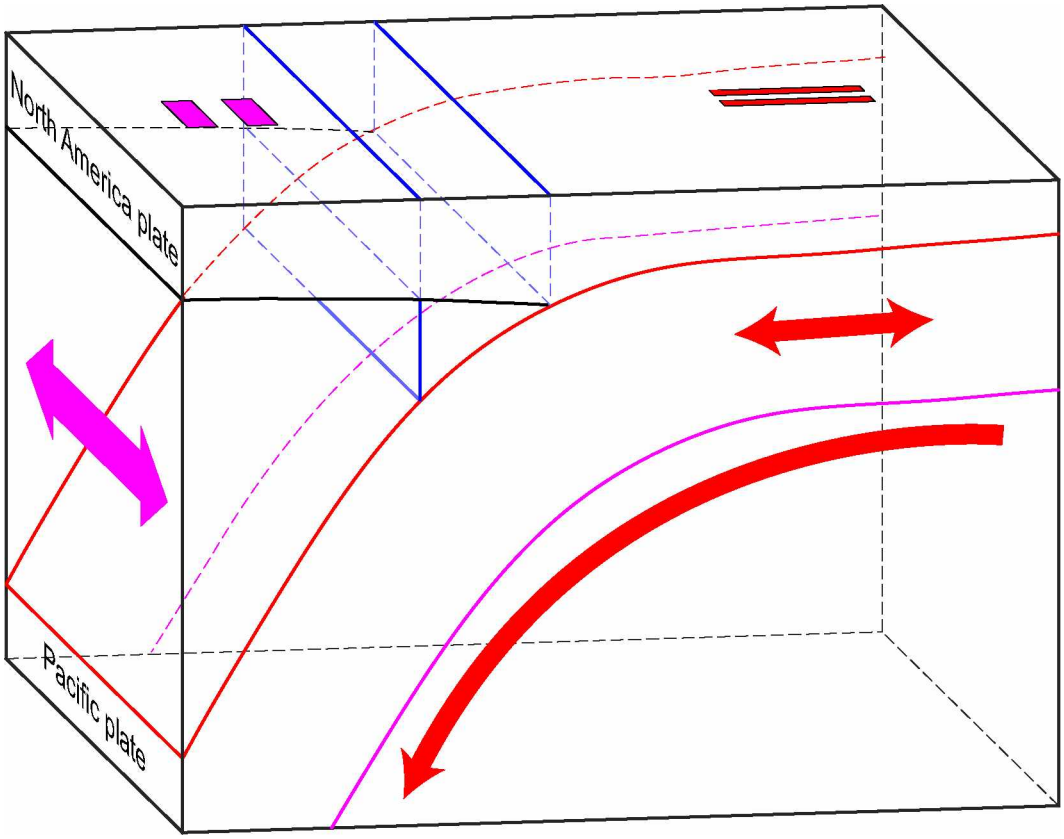

Figure 1.8: 3D Cartoon of the Cook Inlet subduction segment that depicts the observed SKS splitting patterns and interpreted anisotropic structures. The red arrows represent to anisotropy in the slab lithosphere and subslab asthenospheric flow. The overlying red bars represent SKS splitting observations that correspond to the red arrows and thus anisotropy in those regions. The 2-headed magenta arrow is trench-parallel flow in the mantle wedge and the overlying magenta bars are the corresponding SKS splitting measurements. The 2D transect shown in Figure 2.1 and Figure 2.6 was used to interpolate to 3D from a cross-section. The top of Pacific plate is from slab 2.0 (Hayes et al., 2018). The blue region represents the mantle nose.

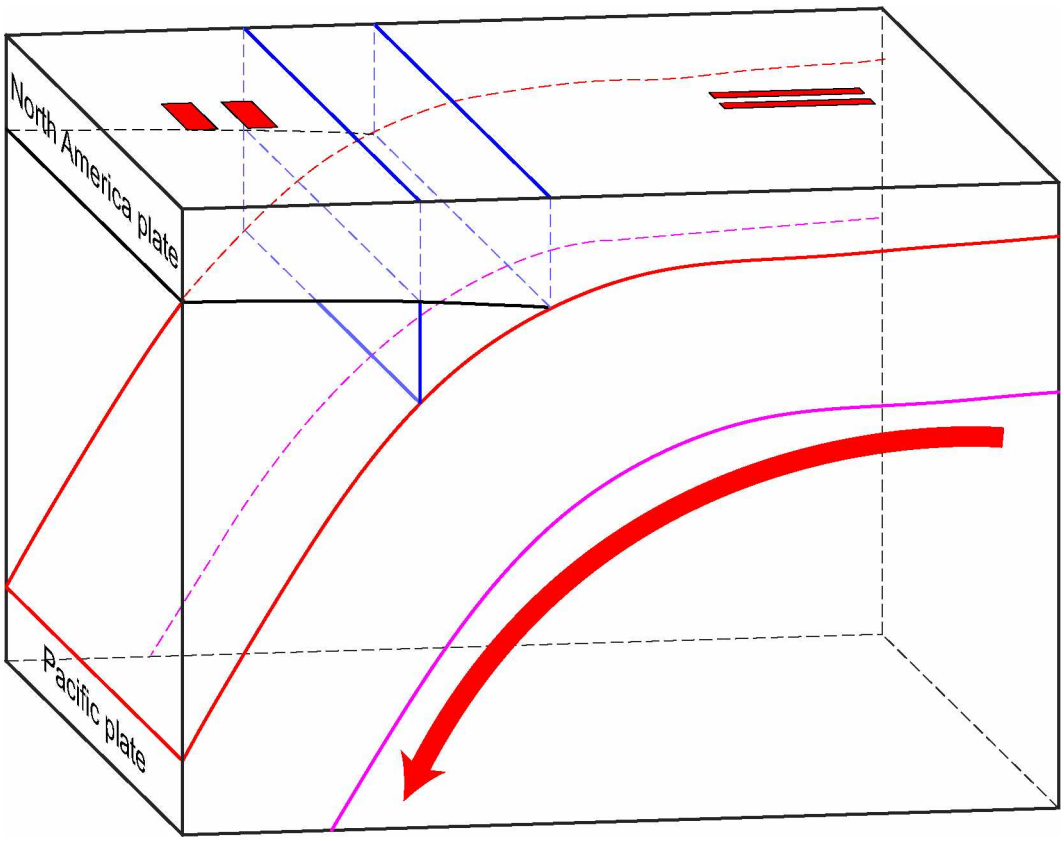

Figure 1.9: 3D Cartoon of the Cook Inlet subduction segment that depicts the observed/predicted SKS splitting patterns and modeled anisotropic structure (Song & Kawakatsu, 2013). The red arrows represent to anisotropy subslab asthenospheric flow. The overlying red bars represent SKS splitting observations and predictions that correspond to the red arrows and thus anisotropy in those regions. Note that the 90° change in observed splitting is due to the change in dip of the subslab asthenospheric anisotropy including a strong assumed radial anisotropy component with no anisotropy in the wedge or Pacific lithosphere. The 2D transect shown in Figure 2.1 and Figure 2.6 was used to interpolate to 3D from a cross-section. The top of Pacific plate is from slab 2.0 (Hayes et al., 2018). The blue region represents the mantle nose.

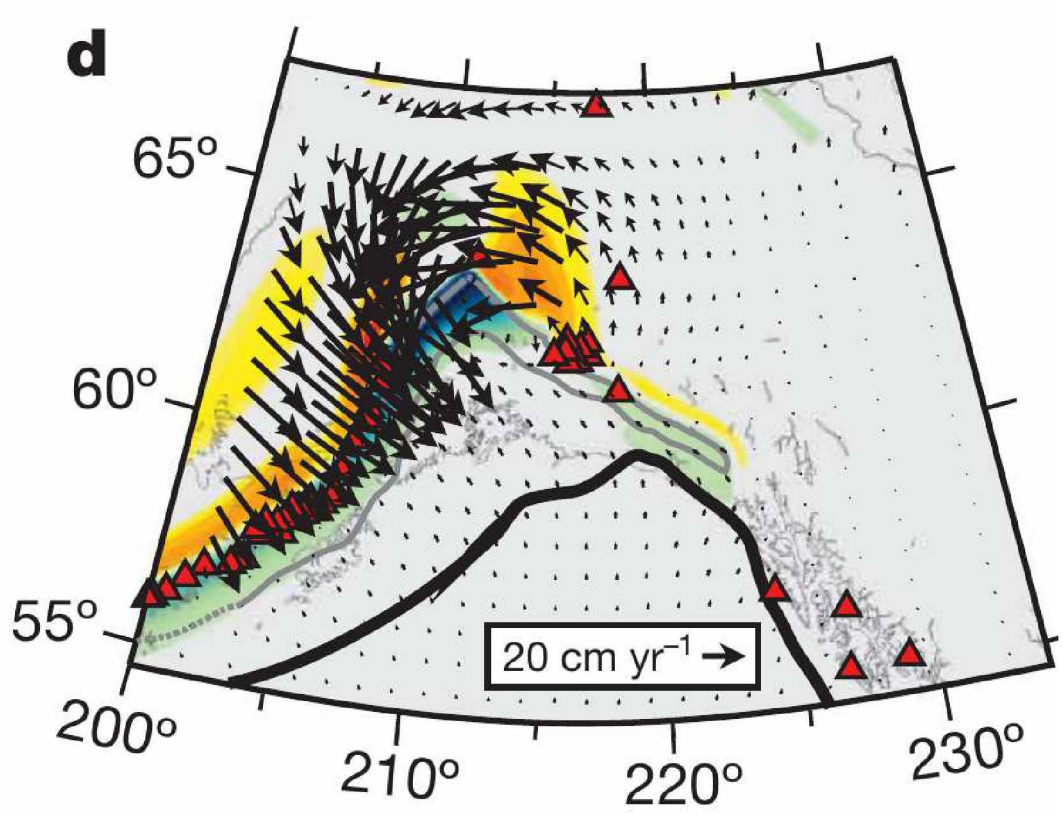

Figure 1.10: Jadamec & Billen (2010) predicted mantle flow field at 100 km depth. Warm and cold colors represent upward and downward velocities, respectively.

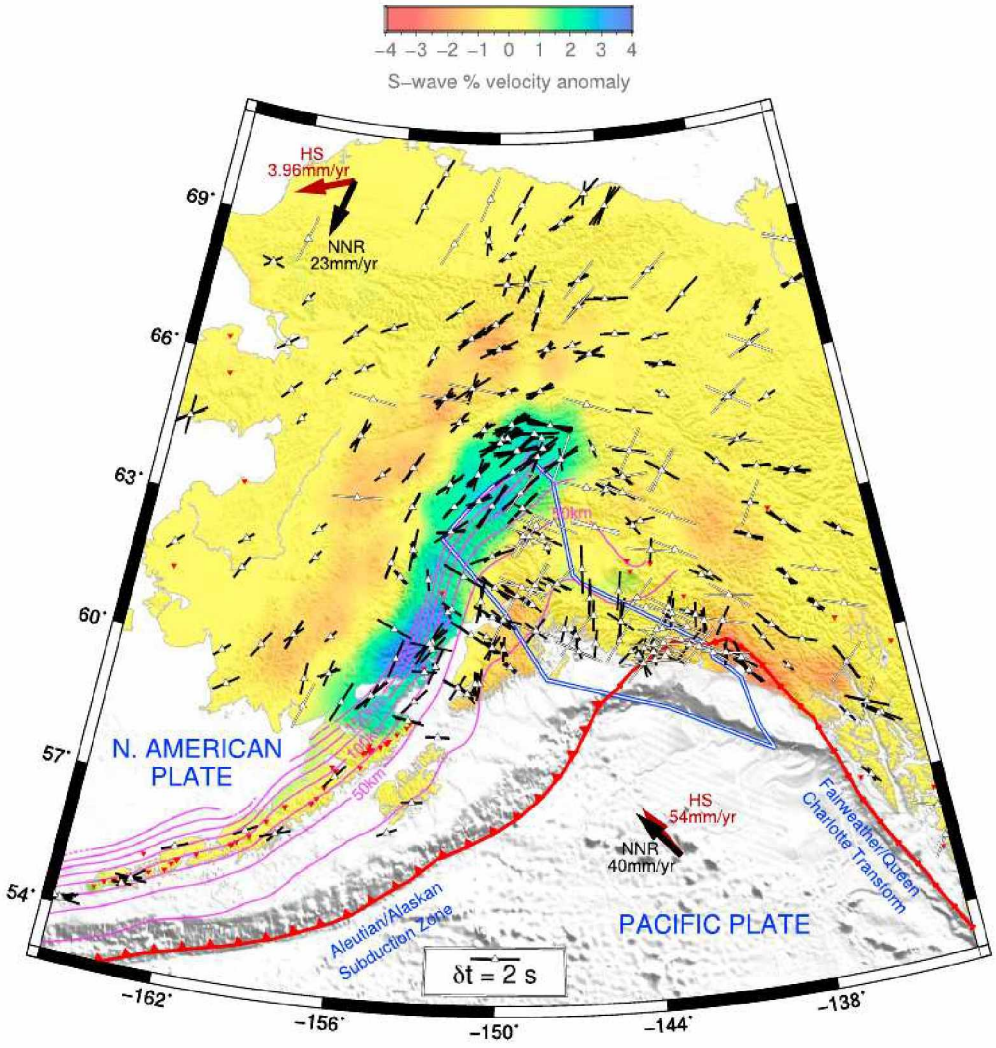

Figure 1.11: Venereau et al. (2019) SKS splitting observations overlain on an S wave velocity model (Martin-Short et al., 2016) depth slice at 200-km depth. White bars are null measurements. Thick blue line is the Yakutat terrane. Solid arrows show the direction of absolute plate motion in both HS and NNR reference frames (Gripp & Gordon, 2002). Subducting slab depth contours in magenta (Hayes et al., 2018). Solid thick red line marks the North American-Pacific Plate boundary. NNR and HS refer to the no-net rotation and hot spot reference frames.

1.2 References

Ando, M., Ishikawa, Y., & Yamazaki, F., 1983. Shear wave polarization anisotropy in the upper mantle beneath honshu, japan, *Journal of Geophysical Research: Solid Earth*, **88**(B7), 5850–5864, doi: 10.1029/JB088iB07p05850.

Argus, D. F., Gordon, R. G., & DeMets, C., 2011. Geologically current motion of 56 plates relative to the no-net-rotation reference frame, *Geochem. Geophy. Geosyst.*, **12**, Q11001, doi: 10.1029/2011GC003751.

Christensen, D. H. & Abers, G. A., 2010. Seismic anisotropy under central Alaska from SKS splitting observations, *J. Geophys. Res.*, **115**, B04315, doi: 10.1029/2009JB006712.

Christensen, D. H., Abers, G. A., & McKnight, T. L., 2003. Mantle anisotropy beneath the Alaska range inferred from *S*-wave splitting observations: Results from BEAAR, in *Eos Trans. Am. Geophys. Un.*, vol. 84(46), Abstract S31C-0782.

Eberhart-Phillips, D., Christensen, D. H., Brocher, T. M., Hansen, R., Ruppert, N. A., Haeussler, P. J., & Abers, G. A., 2006. Imaging the transition from Aleutian subduction to Yakutat collision in central Alaska, with local earthquakes and active source data, *J. Geophys. Res.*, **111**, B11303, doi: 10.1029/2005JB004240.

Fournelle, J. H., Marsh, B. D., & Myers, J. D., 1994. Age, character, and significance of Aleutian arc volcanism, in *The Geology of Alaska*, Geological Society of America.

Fu, Y. & Freymueller, J. T., 2013. Repeated large Slow Slip Events at the south central Alaska subduction zone, *Earth Planet. Sci. Lett.*, **375**, 303–311.

Gripp, A. E. & Gordon, R. G., 2002. Young tracks of hotspots and current plate velocities, *Geophys. J. Int.*, **150**, 321–361.

Hacker, B. R. & Abers, G. A., 2012. Subduction Factory 5: Unusually low Poisson's ratios in subduction zones from elastic anisotropy of peridotite, *J. Geophys. Res.*, **117**, B06308, doi: 10.1029/2012JB009187.

Hanna, J. & Long, M. D., 2012. SKS splitting beneath Alaska: Regional variability and implications for subduction processes at a slab edge, *Tectonophysics*, **530-531**, 272–285.

Hayes, G. P., Moore, G. L., Portner, D. E., Hearne, M., Flamme, H., Furtney, M., & Smoczyk, G. M., 2018. Slab2, a comprehensive subduction zone geomety model, *Science*, doi: 10.1126/science.aat4723.

Jadamec, M. A. & Billen, M. I., 2010. Reconciling surface plate motions with rapid three-dimensional mantle flow around a slab edge, *Nature*, **465**, 338–342, doi: 10.1038/nature09053.

Karato, S., Jung, H., Katayama, I., & Skemer, P., 2008. Geodynamic significance of seismic anisotropy of the upper mantle: New insights from laboratory studies, *Annu. Rev. Earth Planet. Sci.*, **36**, 59–95.

Keith, C. M. & Crampin, S., 1977. Seismic body waves in anisotropic media: synthetic seismograms, *Geophysical Journal of the Royal Astronomical Society*, **49**(1), 225–243, doi: 10.1111/j.1365-246X.1977.tb03710.x.

Kneller, E., van Keken, P., Karato, S.-i., & Park, J., 2005. B-type olivine fabric in the mantle wedge: Insights from high-resolution non-newtonian subduction zone models, *Earth and Planetary Science Letters*, **237**, 781–797, doi: 10.1016/j.epsl.2005.06.049.

Koehler, R. D., Farrell, R.-E., Burns, P. A. C., & Combellick, R. A., 2012. Quaternary faults and folds in Alaska: A digital database, Alaska Div. Geol. Geophys. Surv. Miscellaneous Publication 141, 31 p., 1 sheet, scale 1:3,700,000.

Li, S., Freymueller, J., & McCaffrey, R., 2016. Slow slip events and time-dependent variations in locking beneath Lower Cook Inlet of the Alaska-Aleutian subduction zone, *J. Geophys. Res. Solid Earth*, **121**, 1060–1079, doi: 10.1002/2015JB012491.

Long, M. D., 2013. Constraints on subduction geodynamicws from seismic anisotropy, *Rev. Geophys.*, **51**, 76–112, doi: 10.1002/rog.20008.

Long, M. D. & Silver, P. G., 2009. Shear wave splitting and mantle anisotropy: Measurements, interpretations, and new directions, *Surv. Geophys.*, **30**, 407–461.

Long, M. D. & Wirth, E. A., 2013. Mantle flow in subduction systems: The mantle wedge flow field and implications for wedge processes, *J. Geophys. Res. Solid Earth*, **118**, 583–606, doi: 10.1002/jgrb.50063.

Long, M. D., de Hoop, M. V., & van der Hilst, R. D., 2008. Wave-equation shear wave splitting tomography, *Geophys. J. Int.*, **172**, 311–330.

Martin-Short, R., Allen, R. M., & Barstow, I. D., 2016. Subduction geometry beneath south central Alaska and its relationship to volcanism, *Geophys. Res. Lett.*, **43**, 9509–9517, doi: 10.1002/2016GL070580.

McPherson, A., Christensen, D. H., Abers, G. A., Tape, C., & Moore-Driskell, M. M., 2017. Shear Wave Splitting and Mantle Flow in Alaska, in *AGU Fall Meeting Abstracts*, vol. 2017, pp. DI43B–0365.

Mehl, L., Hacker, B. R., Hirth, G., & Kelemen, P. B., 2003. Arc-parallel flow within the mantle wedge: Evidence from the accreted Talkeetna arc, south central Alaska, *J. Geophys. Res.*, **108**(B8), 2375, doi: 10.1029/2002JB002233.

Miller, M. S. & Moresi, L., 2018. Mapping the Alaska Moho, *Seismol. Res. Lett.*, **89**(6), 2430–2436, doi: 10.1785/0220180222.

Ohta, Y., Freymueller, J. T., Hreinsdóttir, S., & Suito, H., 2006. A large slow slip event and the depth of the seismogenic zone in the south central Alaska subduction zone, *Earth Planet. Sci. Lett.*, **247**, 108–116.

Perttu, A., Christensen, D., Abers, G., & Song, X., 2014. Insights into mantle structure and flow beneath Alaska based on a decade of observations of shear wave splitting, *J. Geophys. Res. Solid Earth*, **119**, 8366–8377, doi: 10.1002/2014JB011359.

Sieminski, A., Paulssen, H., Trampert, J., & Tromp, J., 2008. Finite-frequency *SKS* splitting: Measurement and sensitivity kernels, *Bull. Seismol. Soc. Am.*, **98**(4), 1797–1810.

Silver, P. & Chan, W., 1988. Implications for continental structure and evolution from seismic anistropy, *Nature*, **335**, 34–39, doi: 10.1038/335034a0.

Silver, P. G. & Chan, W. W., 1991. Shear wave splitting and subcontinental mantle deformation, *J. Geophys. Res.*, **96**(B10), 16,429–16,454.

Song, T.-R. A. & Kawakatsu, H., 2013. Subduction of oceanic asthenosphere: A critical appraisal in central Alaska, *Earth Planet. Sci. Lett.*, **367**, 82–94.

Venereau, C., Martin-Short, R., Bastow, I., Allen, R., & Kounoudis, R., 2019. The role of variable slab dip in driving mantle flow at the eastern edge of the alaskan subduction margin: insights from sks shear-wave splitting, *Geochemistry, Geophysics, Geosystems*, doi: 10.1029/2018GC008170.

Wei, M., McGuire, J. J., & Richardson, E., 2012. A slow slip event in the south central Alaska Subduction Zone and related seismicity anomaly, *Geophys. Res. Lett.*, **39**, L15309, doi: 10.1029/2012GL052351.

Wiemer, S., Tytgat, G., Wyss, M., & Duenkel, U., 1999. Evidence for shear-wave anisotropy in the mantle wedge beneath south central Alaska, *Bull. Seismol. Soc. Am.*, **89**(5), 1313–1322.

Yang, X., Fischer, K., & Abers, G., 1995. Seismic anisotropy beneath shumagin island segment of the aleutian-alaska subduction zone, *Journal of Geophysical Research*, **100**, doi: 10.1029/95JB01425.

Chapter 2

Anisotropy in the Alaska subduction zone: shear-wave splitting observations from local and teleseismic earthquakes[1]

2.1 Abstract

Shear-wave splitting observations can provide insight to mantle flow due to the link between the deformation of mantle rocks and their direction dependent seismic wave velocities. We identify shear-wave anisotropy in the Cook Inlet segment of the Alaska subduction zone by analyzing splitting parameters of S phases from local intraslab earthquakes between 50 and 200 km depths and SKS waves from teleseismic events. These earthquakes were recorded from 2015–2017 (local S) and 2007–2017 (SKS) by stations from SALMON (Southern Alaska Lithosphere and Mantle Observation Network), TA (EarthScope Transportable Array), MOOS (Multidisciplinary Observations Of Subduction), AVO (Alaska Volcano Observatory), and the permanent network. Automatic phase picking (dbshear) of 12095 local earthquakes ($M_l \geq 1.5$) recorded at 84 stations yielded 678 high-quality splitting measurements (filtered 0.2–1 Hz). Teleseismic SKS phases recorded at 112 stations with 26,143 event–station pairs resulted in 360 high-quality SKS splitting measurements (filtered 0.02–1 Hz and 0.01–1 Hz). Measurements for both datasets were made using the SC91 minimum eigenvalue method with software package MFAST. We compare local S and SKS splitting patterns both from previous studies and our own analysis and find that they are most similar in the far forearc, at the Kenai Peninsula, below which there is no mantle wedge. Anisotropy in the subducting Pacific lithosphere and subslab asthenosphere is likely here as both S and SKS display plate convergence fast directions and SKS measurements exhibit delay times too long (~2 s) to be explained solely by lithospheric anisotropy. Large splitting delay times (~0.5 s) for local measurements that mainly sample slab further indicate that the Pacific slab lithosphere contains significant anisotropy. We also observe anisotropy in the mantle wedge indicated by an increase in delay time as focal depth increases for stations with ray paths dominantly sampling wedge. These measurements display trench-perpendicular and plate convergence fast directions consistent with 2D corner flow in the mantle wedge. Both datasets show trench-parallel splitting directions in select areas of the arc/forearc that overlie parts of the mantle wedge and nose. B-type olivine in the mantle nose, subslab asthenospheric flow, flow around the slab edge, and anisotropy in the Pacific lithosphere all could be invoked to explain this pattern. While we are unable to distill the anisotropy to a single responsible structure, the sharp transition in the local S data splitting pattern from trench-perpendicular in the backarc to trench-parallel across the arc suggests B-type olivine in the mantle nose. For an overall model, we favor 2D corner flow of A-type olivine in the mantle

[1]To be published as: Richards, C., Tape, C., and Ross, Z., 2020. Anisotropy in the Alaska subduction zone: shear-wave splitting observations from local and teleseismic earthquakes, *Earth and Planetary Science Letters*.

wedge induced by downdip motion of the slab, B-type olivine in the nose, and plate convergence parallel anisotropy in the subslab asthenosphere and subducting Pacific lithosphere to explain the observed splitting patterns. It is clear that the subducting slab's structure and motion are the dominant influence on anisotropy and mantle flow regimes here. The differences in local S and SKS splitting results motivate further study on frequency dependence of splitting measurements and emphasize the need for a better understanding of which earth structures are responsible for the observed splitting patterns globally. This study constitutes the first comprehensive local splitting study in Alaska and refutes the common interpretation of along arc flow in the mantle wedge proposed by many previous splitting studies in Alaska.

2.2 Introduction

When a shear wave propagates through a seismically anisotropic structure it splits into two orthogonal phases that travel at different velocities (Silver & Chan, 1991). These two phases can be recorded at a seismic station and a splitting measurement can be made in attempt to characterize the anisotropy that split the wave. A shear-wave splitting measurement consists of two parameters that relate to the orientation and strength of anisotropy that the shear wave encountered. These two parameters are the polarization of the fast phase (ϕ) and the separation in time between the two split phases (δt). Shear-wave splitting measurements are path integrated and thus the anisotropy responsible for the splitting may be located at any point along the ray path. Therefore, any interpretation regarding the origin of the anisotropy must consider all structures that the shear wave encountered as possible anisotropic sources. In complex tectonic settings such as subduction zones, where anisotropy can exist in all parts of the system (the overriding plate, subducting slab, mantle wedge, and subslab mantle), multiple approaches ought to be used when trying to characterize the anisotropic structures.

Shear-wave splitting has been utilized to study anisotropy in both the crust (Bamford & Crampin, 1977; Crampin et al., 1984; Crampin & Peacock, 2008; Okaya et al., 2016) and upper mantle in various regions around the globe (Silver & Chan, 1991; Savage, 1999). In the case of the upper mantle, anisotropy is most commonly attributed to lattice preferred orientation (LPO) of mantle olivine (Karato et al., 2008). When olivine is strained, its crystallographic fast axes can become aligned parallel to (A-type or similar) or orthogonal to (B-type) the direction of maximum strain. A-type olivine is dominant in typical upper mantle conditions while B-type olivine is found in wet, low temperature regimes like those found in the nose of the mantle wedge (Karato et al., 2008; Kneller et al., 2005). This implies that for a single mantle flow direction, you may observe shear-wave splitting fast directions that are parallel (A-type) and/or orthogonal (B-type) to the flow direction depending on the types of olivine fabrics that are present.

In subduction zones it is predicted that multiple types of olivine may be present, including B-type in the cold nose of the mantle wedge. This has been used to explain sharp transitions of shear-wave splitting fast directions from trench-parallel in the arc/forearc to trench-perpendicular in the back arc without requiring a change in mantle flow direction (Nakajima & Hasegawa, 2004; Kneller et al., 2005). Although there are exceptions (Hammond et al., 2010; Schlaphorst et al., 2017), most local splitting studies around the globe have suggested that the mantle wedge is the main anisotropic structure in the subduction system (Wiemer et al., 1999; Nakajima & Hasegawa, 2004; León Soto & Valenzuela, 2013; Long & van der Hilst, 2006; Abt et al., 2009). In the Alaska subduction zone specifically, anisotropy has been suggested to be present in the mantle wedge as well as in the subducting Pacific lithosphere and subslab asthenosphere. (Christensen & Abers, 2010; Perttu et al., 2014; McPherson et al., 2017; Venereau et al., 2019; Hanna & Long, 2012; Song & Kawakatsu, 2013).

Shear waves produced by local intraslab earthquakes and teleseismic SKS phases travel through various parts of the subduction system and therefore both lend themselves well to studying seismic anisotropy in subduction zones. An advantage to local events is that the path is directly between the slab earthquake and the overlying station (usually within 200 km). Additionally, for most subduction geometries, the majority of the ray path for deep intraslab earthquakes will be within the mantle wedge for arc/backarc stations. The forearc stations will have ray paths that mostly sample the slab and all rays will travel through the overriding plate. Thus all components of the subduction system other than the subslab mantle ought to be thoroughly sampled by local S waves. Conveniently, SKS waves do sample the subslab mantle. In the case of SKS splitting the path spans the entire mantle with maximum sensitivity of the measurement to structure that is above, within, and below the slab making depth constraints difficult (Sieminski et al., 2008; Long et al., 2008). Intraslab earthquakes originate from a range of depths and can aid in interpreting which structures and depths the anisotropy belongs to. Local splitting measurements are made at much higher frequencies and thus are more susceptible to influence from small-scale structures and topography. As a result, local splitting studies typically display more scatter in their resulting splitting patterns than SKS. Lastly, the initial polarization of the SKS wave is known to be in the plane parallel to the radial direction as it exits the core while the initial local S wave polarization is unknown and depends on the focal mechanism. Knowing the initial polarization removes one unknown from the splitting measurement inversion and also allows for multiple methods of measurement to be used. These advantages and disadvantages promote the utilization of both phases when characterizing a subduction system's anisotropic structures.

Globally, the two most common splitting patterns for local splitting studies are trench-parallel and trench-parallel in the forearc transitioning to trench-perpendicular in the backarc (Long &

Wirth, 2013). There have been very few local splitting studies in Alaska, all of which lack large datasets, robust backarc station coverage, and they show a range of different splitting patterns for various sections of the subduction zone. Wiemer et al. (1999) used only three stations and showed trench-parallel fast directions in the forearc, along with several trench-parallel measurements in the backarc near Redoubt volcano. Christensen et al. (2003) published preliminary results in an abstract that shows roughly the opposite transition (trench-perpendicular to trench-parallel) occurs further northeast where the slab dip is shallow. Hacker & Abers (2012) showed only a single example. Yang et al. (1995) showed a mostly trench-parallel pattern in the Shumagin Islands. Conversely, there have been numerous thorough SKS splitting studies done in Alaska and its subduction zone over the past decade (Christensen & Abers, 2010; Perttu et al., 2014; McPherson et al., 2017; Venereau et al., 2019; Hanna & Long, 2012). These studies mainly focused on the flat slab subduction segment that includes subduction of the thick Yakutat terrane and a gap in arc volcanism (Figure 2.1). All of these studies display an SKS splitting pattern that abruptly transitions from trench-perpendicular southeast of the 70 km depth contour of the subduction interface to trench-parallel northwest of the 70 km contour. The trench-parallel pattern is usually attributed to along arc flow in the mantle wedge (Figure 2.2), while the trench-perpendicular pattern is attributed to a combination of plate convergence direction entrained asthenospheric flow beneath and fossil anisotropy within the subducting Pacific plate (Figure 2.2). However, Song & Kawakatsu (2013) argued that both patterns can be explained solely by asthenospheric flow beneath the subducting slab and that the sharp change in fast directions is due to the change in the dip of slab and flow beneath it (Figure 2.3). This change results in part from an assumption of a strong radial anisotropic component.

The lack of a comprehensive local splitting study combined with the fact that SKS studies have shown varied anisotropy patterns in multiple parts of the subduction system greatly motivates a thorough local splitting study in the Alaska subduction zone. This is emphasized by the competing interpretations of the coherent trench-perpendicular and trench-parallel patterns observed by all previous SKS studies. If this pattern is due to subslab asthenospheric flow and not lithospheric structure, shear-wave splitting from local events should be able to discern this. Local S waves will not travel through the subslab asthenosphere and thus any splitting observed can not be attributed to asthenospheric flow. Furthermore, splitting from local events that sample the mantle wedge may help distinguish whether or not the trench-parallel splitting northwest of the 70 km contour is from along-arc flow in the mantle wedge as suggested by SKS splitting studies or asthenospheric flow beneath the subducting slab as suggested by Song & Kawakatsu (2013). In this study we present the first large scale local shear-wave splitting analysis in Alaska and combine

this with SKS splitting from teleseismic events in attempt to characterize the main anisotropic components of the Cook Inlet segment of the Alaska subduction zone.

The Cook Inlet segment is located towards the eastern end of the 3000 km-long Aleutian-Alaskan subduction zone and exhibits "normal" subduction with a robust volcanic arc and abundant seismicity down to approximately 200 km depth (Figure 2.1 and Figure 2.4). The 45-55 Ma Pacific plate subducts under the North American plate and and this general configuration has been stable for the last 40-50 Ma (Figure 2.5). Plate motion has often been linked to shearing and flow in the upper mantle (Long & Wirth, 2013) including viscous coupling between the downgoing slab and the overlying mantle (van Keken, 2003). In order to attempt to relate plate motion to mantle deformation and dynamics, a reference frame for plate motion must be defined. Early studies in the development of plate motion reference frames include Lliboutry (1974); Solomon & Sleep (1974); Kaula (1975); Minster & Jordan (1978). In an effort to move towards a generalized plate motion reference frame, Becker et al. (2015) examined 11 different reference frames with Euler vectors that add to the no-net-rotation plate model (NNR-MORVEL) of Argus et al. (2011). The five that we consider in this study include NNR-MORVEL (Argus et al., 2011), spreading alignment (Becker et al., 2015), a reference frame related to global SKS splitting (SKS5) (Becker et al., 2015), a hot spot reference frame (MM07-M) (Morgan & Morgan, 2007; Doubrovine et al., 2012), and a fixed North America reference frame. While considering a fixed North America reference frame, we acknowledge that the region of south-central Alaska is not actually fixed to interior North America but in fact moves a few mm/yr (Freymueller et al., 2008). In general, for these reference frames, at $(-150^\circ, 59^\circ)$ the Pacific plate moves northwest at $\sim$52 mm/yr and at $(-155.3^\circ, 60.5^\circ)$ the North American plate south-southwest at $\sim$10–20 mm/yr (e.g., Figure 2.12).

2.3 Data and Methods

2.3.1 Local S

For the local shear-wave splitting analysis we examined earthquakes recorded from 2015-01-01–2017-11-30 by stations from SALMON (Southern Alaska Lithosphere and Mantle Observation Network), TA (EarthScope Transportable Array), AVO (Alaska Volcano Observatory), and the permanent network (Figure 2.6). In total there are 84 stations that were active for all or part of this period. The SALMON array was an arc-normal line of broadband receivers traversing the Cook Inlet segment of the Alaska subduction zone near Redoubt volcano. This combination of networks, specifically SALMON, provides robust station coverage of the forearc, arc, and backarc. Our region of interest is bounded by longitudes -156° to -148° and latitudes 59° to 62°. 12095 earthquakes located at depths ≥ 50 km and with magnitudes $M_l \geq 1.5$ were selected for shear-

wave splitting analysis. The depth constraint puts an emphasis on events that sample the mantle wedge and subducting slab and excludes shallow crustal events. The magnitude limit is an attempt to allow for a reasonable sized catalog of events and sufficient signal in the frequency band of interest (0.2–1 Hz). Only ray paths with angles of incidence smaller than 37° were considered in order to avoid contamination of particle motions (Nuttli, 1961). For reference, vertical incidence is defined as 0° and Figure 2.7 shows the geometric constraints of the ray paths that were considered for shear-wave splitting analysis. Incidence angles and ray paths were determined using TauP (Crotwell et al., 1999) and a velocity model (scak) that includes improved velocities for the crust of southern Alaska (Table 2.1). Automatic S phase picking (Ross et al., 2016) yielded 678 high-quality splitting measurements (filtered 0.2–1 Hz) using the software package MFAST (Savage et al., 2010; Teanby et al., 2004; Wessel, 2010). MFAST utilizes the method of Silver & Chan (1991) over many time windows following Teanby et al. (2004) to determine a fast polarization direction (ϕ) and delay time (δt) for each event station pair. This involves minimizing the second eigenvalue of the covariance matrix which is equivalent to finding the most linearized particle motion for a specific rotation and time-shift of the horizontal components. As measurements are made over many varied time windows, clusters of measurements with similar ϕ and δt are gathered. Error in ϕ and δt are determined with an F-test which calculates the 95% confidence interval for both parameters. The best solution (pair of ϕ and δt) is chosen to be the one with the smallest errors within the best cluster. Each measurement is assigned a grade based on its signal to noise ratio (SNR), uncertainty in fast direction, and whether or not other very different ϕ and δt produce a similar quality solution. Furthermore, if the determined initial polarization of the shear wave is within 20° of ϕ (or the orthogonal slow direction), the measurement is considered null. Null measurements indicate that the shear wave was polarized parallel to either the fast or slow axis or that no splitting occurred. We do not consider null results as there is much ambiguity in interpreting them. We only considered the highest-quality measurements (grade A) and also manually inspected each measurement, discarding those that showed signs of cycle skipping or non-linear particle motions. Figure 2.8 shows an example of a grade A local splitting measurement made at backarc SALMON station HLC5.

2.3.2 SKS

The teleseismic dataset includes earthquakes from 2007-01-01 to 2017-12-31 recorded by SALMON, MOOS (Multidisciplinary Observations Of Subduction), TA, AVO, and the permanent network. All teleseismic data was pulled from the IRIS Data Management Center. In total there are 111 stations that were active for all or part of this period. The same region of interest used for the local S dataset was used here, and most of the stations are the same as well. The largest addition is that of

MOOS (2006–2009) stations. MOOS provides dense station coverage on the Kenai Peninsula, especially the eastern portion, below which there is no mantle wedge. We include earthquakes with magnitudes $M_w \geq 6.0$ occurring at epicentral distances between 80° and 140°, where the SKS-wave is isolated from other phases. SKS arrivals and ray paths were determined using TauP with velocity model scak (Table 2.1). The same measurement and quality control methods that were used for the local S splitting were applied to the SKS dataset except that here we filter for either 0.01–1 Hz or 0.02–1 Hz and use larger windows when making the measurement. Seismograms for 26,143 event station pairs were analyzed, resulting in 360 high-quality SKS splitting measurements. Figure 2.9 shows an example of a grade A SKS splitting measurement made at backarc SALMON station WFLS.

2.4 Results

2.4.1 Local S

Starting with ~1,000,000 event-station pairs we end up with 678 high-quality grade A local S shear-wave splitting results. Many measurements were discarded due to shallow incidence angles, null measurements, and low SNR. Low SNR seems to be the main factor in measurements failing to meet the grade A criteria. For instance, our input dataset contains 11024 $M_l \leq 2.5$ earthquakes but only 109 high-quality measurements have $M_l \leq 2.5$ (Figure 2.10 and Figure 2.11). The average magnitude of the input dataset (M_l 1.92) and grade A measurements (M_l 3.20) is drastically different. Conversely, the average depth of events for both the input dataset and the passing grade A measurements is similar at 95.33 km and 99.32 km, respectively. Lastly, the measured δt for grade A measurements ranges from 0.06–0.79 s with an average of 0.33 s.

Figure 2.12 and Figure 2.16 show all 678 grade A local S shear-wave splitting results superimposed on a map of the Cook Inlet as well as their rays traced through a cross section profile of the subduction zone. Red contours represent the depth to the subduction interface ranging from 40 to 180 km (20 km intervals) (Hayes et al., 2018). Each measurement is plotted as a bar with its orientation parallel to the fast direction (ϕ) and length proportional to its delay time (δt). We show two types of projections for the local splitting measurements, midpoint and event location projection (Figure 2.7). For midpoint projection, each shear-wave splitting measurement is plotted at the surface directly above the midpoint of the ray path. This is not to suggest that this is where the anisotropic structure lies, but rather helps show coherent spatial patterns and back azimuthal dependence. Event location projection plots the splitting measurement at the epicenter of the event. This projection can help show whether or not shear waves originating from the same area have similar splitting parameters.

Ray tracing shows that some of the measurements have largely horizontal ray paths before steepening via refraction in shallow depths to meet the 37° incidence angle requirement. Due to this, many rays sample the wedge at angles more horizontal than the 37°. As is shown in Figure 2.12 and Figure 2.16, the local shear waves densely sample the subducting slab, shallow mantle wedge, and parts of the overriding plate. The region of the mantle wedge deeper than ∼100 km is sparsely sampled and no part of the wedge deeper than∼ 150 km is sampled, nor is the subslab mantle. In general, the forearc stations have ray paths through the slab and/or mantle nose and arc/backarc stations have paths through the mantle wedge and nose. All ray paths travel through the overriding plate.
Local splitting maps and measurements for all stations and measurements used in this study are shown in Richards (2020).

2.4.2 SKS

Figure 2.19 shows all 360 grade A SKS measurements superimposed on a map of Cook Inlet as well as each measurement's ray traced through a cross section profile of the subduction zone. All of the map's features are the same as the local S splitting maps other than the delay time scale (length of bar, see legend) and the splitting measurement projection. The projection used here plots the splitting measurement at the surface directly above the 100 km depth point of the ray path. The 100 km depth point is shown as a green dashed line in the cross section profile. Again, this is not to suggest that this is the depth where the anisotropic structure lies, but rather helps show coherent spatial patterns and back azimuthal dependence.

Due to the nature of teleseismic ray paths all the rays travel nearly vertically and this is seen in the ray tracing cross section of Figure 2.19. The most densely sampled region by the SKS measurements is the Kenai Peninsula where the slab dip is very shallow and there is no underlying mantle wedge. The steeply dipping section of the slab and mantle wedge above the 75–150 km slab depth contours is sparsely sampled. No SKS rays travel through the furthest corner mantle of the wedge/nose (50–75 km slab depth). The furthest back arc stations sparsely sample the mantle/wedge beyond where the slab depth reaches 200 km.
Teleseismic splitting maps and measurements for all stations and measurements used in this study are shown in Richards (2020).

2.4.3 Classification of local S splitting regions

To facilitate discussion and interpretations, we distill the local S splitting observations into regions. We use two approaches for this purpose: (1) careful examination of patterns found in individual

station maps, and (2) examination of spatially smoothed dataset. The full dataset for local S is shown in Figure 2.12 and Figure 2.16. Our procedure for spatial smoothing is as follows:

1. Define each splitting measurement as a complex number $z = re^{i\alpha}$, where r is the magnitude (δt) and α is the polar angle (counterclockwise from east).

2. Calculate $z^2 = r^2 e^{i2\alpha}$ and define $Z = z^2 = A + iB$.

3. Since z vary with colatitude θ and longitude ϕ, we have $Z(\theta,\phi) = A(\theta,\phi) + iB(\theta,\phi)$.

4. Apply a multiscale spherical wavelet estimation procedure (Tape et al., 2009, 2012) to obtain the spatially continuous scalar functions $A'(\theta,\phi)$ and $B'(\theta,\phi)$, which in turn give $Z'(\theta,\phi)$, where the prime-notation denotes an estimated quantity.

   For our dataset we used spherical grid orders $q = 6, 7$, and 8 to estimate the continuous functions.

5. Evaluate $Z'(\theta,\phi)$ at the input values of (θ,ϕ) and convert back to r' and α'.

Figure 2.13 and Figure 2.17 show the spatially smoothed datasets derived from Figure 2.12 and Figure 2.16, respectively. Figure 2.14 and Figure 2.18 show direct comparisons.

Using the spatially smoothed dataset, in addition to individual station maps, we identify four splitting regions as shown in Figure 2.15. From west to east, these regions are:

- Region L1b, plate convergence parallel pattern (north-northwest to south-southeast) for the deepest events ($\geq\sim$150 km) recorded at backarc stations (Figures 2.25, 2.28, 2.29, and 2.34).

- Region L1a, clear trench-perpendicular pattern in the arc and backarc (Figures 2.25, 2.28, and 2.29).

- Region L2, the forearc region ($\sim$60–80 km subduction interface contour) displays a mostly trench-parallel pattern (Figures 2.25, 2.33, and 2.34).

- Region L3, the western portion of the Kenai Peninsula shows fast directions sub-parallel to the plate convergence direction.

The label L is a reminder that these classifications are based on local S data.

2.4.4 Classification of SKS splitting regions

Based on our SKS data in Figure 2.19 and smoothed datasets in Figure 2.20 and Figure 2.21, we qualitatively define three regions containing different SKS splitting patterns (Figure 2.24). From west to east, these regions are:

- Region T1, west of the ~180 km subduction interface contour and while the majority of measurements have trench-perpendicular fast directions, this region has the highest amount scatter. Region T1 does not have much overlap with the local regions.
- Region T2, between the ~40 and ~180 km subduction interface contours and displays a trench-parallel splitting pattern along with some scatter. Region T2 roughly aligns with region L1a, region L1b, and parts of region L2.
- Region T3, east of the ~40 km subduction interface contour (Kenai Peninsula), contains most of the SKS measurements, and displays a strongly coherent plate-convergence-parallel splitting pattern. Region T3 roughly aligns with region L3.

The label T is a reminder that these classifications are based on teleseismic SKS data.
Figure 2.22 and Figure 2.23 show direct comparisons between data and smoothed estimates.

2.5 Discussion

We discuss and interpret our results in the context of the splitting regions in Sections 2.4.3 and 2.4.4.

2.5.1 Local S

The dominant pattern of the local S data set is one of trench-perpendicular fast directions, characterizing region L1a. This can best be seen in the midpoint projection map (Figure 2.12) and backarc station maps (Figures 2.28, 2.29, and 2.30). Region L1a has splitting measurements with the majority of their ray path in the mantle wedge. Due to the slab and station array geometry, these ray paths only exist for stations in the arc and backarc (Figure 2.25). Examining the relationship between δt and focal depth for stations with at least ~50 km of wedge beneath them reveals that δt slightly increases as focal depth increases (Figure 2.27). The event depths were binned into 10-km bins and an average δt was calculated from all delay times corresponding to that bin. The grouping of stations with ~50 km of underlying wedge was chosen in attempt to select those whose ray paths are dominantly in the mantle wedge. The Moho depth is approximately 40–50 km here and thus once the underlying wedge is ~50 km thick, more of the ray path will be in the wedge than in the overriding plate for most event-station pairs. For measurements at these stations, an increase in focal depth typically corresponds to a longer ray path in the mantle wedge and thus a longer delay time. For example, ray paths at station N19K show that the path through the wedge is ~110 km for focal depths near 150 km ($\delta t \approx 0.5s$) and only ~75 km for focal depths near 85 km ($\delta t \approx 0.2s$) (Figure 2.29). Among other splitting studies at various subduction zones around the globe, both Wiemer et al. (1999) and Christensen & Abers (2010) suggest an anisotropic wedge

and show δt increases with path length in the wedge in the Alaska subduction zone. Although it is only based on two measurements, Wiemer et al. (1999) show very minor crustal splitting in our study region ($\delta t \leq 0.1s$) which further supports that the long delay times we observe in the back arc stations is due to anisotropy in the wedge with only minor crustal contributions.

This trench-perpendicular style of splitting pattern observed in region L1a is often interpreted as 2D corner flow as A-type olivine LPO is expected in the hot dehydrated mantle wedge. (Hall et al., 2000; Long & Wirth, 2013; Kneller et al., 2005; Long & Silver, 2008). Our observations support the common finding that the mantle wedge is a major contributing anisotropic structure in the subduction system and we interpret the clear trench-perpendicular pattern in the arc and backarc to be 2D corner flow of A-type olivine.

Many of the trench-parallel measurements in the forearc (region L2) have ray paths that sample the nose of the mantle wedge (Figures 2.25, 2.26, 2.32, 2.33, 2.34, 2.35, 2.36). These observations fit the predicted 90° rotation in fast directions that occurs in 2D corner flow with B-type olivine LPO in the cold hydrated nose of the mantle wedge (Kneller et al., 2005; Karato et al., 2008). Wiemer et al. (1999) also show a trench-parallel local splitting pattern in region L2 as well as some evidence of the sharp 90° transition across the arc. While trench-parallel flow of A-type olivine in the mantle nose beneath would exhibit a trench-parallel splitting pattern, it seems unlikely to dominate the flow here as our pattern in region L1a matches well with 2D corner flow. The ray paths that sample the nose all originate in the slab and inherently have some path length in the slab. Furthermore, for this subset of measurements, the path lengths in the overriding plate are as larger or larger than paths in the nose. It is difficult to say whether the main contributor to this splitting pattern is the nose, the slab, the overriding plate, or all three. However, we favor that the trench-parallel splitting pattern observed here is due to B-type olivine in the mantle nose because of the strong evidence of 2D corner flow observed in region L1a. This can be seen by plotting splitting measurements for single stations with ray paths in the nose and wedge (Figures 2.34 and 2.35) as well as the grouping of stations with wedge/nose paths shown previously (Figures 2.25 and 2.26). The transition appears to take place at about the 80 km subduction interface contour.

We also observe fairly large delay times for some ray paths that sample no mantle wedge at all. Rays from deep events traveling to stations in the forearc sample entirely the slab and overriding plate, and yet can have δt comparable to the measurements with similar path lengths but in the mantle wedge (Figure 2.31). The measurements with paths in the slab display a complex splitting pattern (Figure 2.37). However, at the northern end of region L2 where the slab dip is more shallow there is a decently coherent trench-parallel pattern. Naugler & Wageman (1973) show consistent north-south magnetic lineations related to ancient Farallon ridge spreading. These lineations are located immediately adjacent to the Alaska subduction zone and are roughly parallel

to these northern splitting fast directions (ϕ) in region L2. Chen et al. (2015) also show a distinct anisotropic signature (δt = 0.13–0.45 s) in the subducting Philippine Sea plate from intraslab earthquakes with similar slab ray paths to ours. The fast directions are roughly trench-parallel and are interpreted to originate from a fossil spreading fabric of the Philippine Sea plate. The semi-coherent pattern that we observe in the north may be due to anisotropic structure within the subducting Pacific plate related to its fossil spreading direction, but this would only explain this small subset of measurements. The complexity may be arising from the change in dip of the slab and therefore anisotropy within the slab and/or anisotropy in the overriding plate. While it is difficult to interpret the resulting complex fast directions of the slab measurements, the long delay times provide strong evidence that the lithosphere in the subducting slab is significantly anisotropic.

The western portion of the Kenai Peninsula (region L3) shows fast directions sub-parallel to the plate convergence direction, has shallow focal depths ($\sim$ 50–60 km), and exhibits short delay times ($\delta t \approx$ 0.2s). There is no mantle wedge beneath this region, but rather these rays sample the the subducting lithosphere and the overriding plate (Figure 2.38). While these measurements could have been influenced by anisotropy in the overriding plate, we interpret the splitting to be in the subducting lithosphere because we have shown that the slab is substantially anisotropic. This interpretation is further supported by Wiemer et al. (1999) showing that crustal contributions to splitting are minimal near this region.

Our observations require a model that can explain splitting patterns of trench-perpendicular and plate convergence parallel in the backarc, trench-parallel in the forearc, and plate convergence parallel in the furthest forearc. With the addition of an anisotropic slab, some commonly invoked subduction zone mantle flow models could explain the observed splitting patterns (Long & Wirth, 2013). These models include 2D corner flow, 2D corner flow with B-type olivine in the mantle nose, and a model proposed by Long & Silver (2008). The Long & Silver (2008) model predicts both 2D corner flow induced by downdip motion of the slab in the back arc and 3D flow around the slab edge producing trench-parallel flow in the forearc near the edge. 3D flow around the slab edge has been suggested by previous SKS (Venereau et al., 2019) and geodynamic modeling (Jadamec & Billen, 2010) in Alaska. Geodynamic modeling predicts mantle flow around the slab edge but only shows trench-parallel flow proximal to the edge. The predicted mantle flow at 100 km depth for most of our region is approximately trench-perpendicular and becomes closer to the plate convergence direction further north and further into the back arc. The 2D corner flow part of the Long & Silver (2008) model depicts mantle wedge flow parallel to the dip and convergence direction of the slab in the backarc. We note that our observed trench-perpendicular pattern in the arc and backarc (region L1a) is parallel to the dip direction of the slab but not quite to the convergence

direction. This may be due to the two flow regimes competing near the arc (Long & Silver, 2008). However, most our region is far enough from the slab edge that we do not expect much influence of trench-parallel flow from around the edge. At the furthest backarc stations (region L1b) we do see splitting directions become parallel to the plate convergence direction. This seems to indicate that this region is far enough into the backarc for the 2D corner flow induced by the motion of the subducting slab to dominate the flow regime. The Long & Silver (2008) model could also explain the splitting pattern in region L2 if type-B olivine is present in the nose with 2D corner flow or if the along arc flow coming from around the slab edge has an influence further along the arc than is predicted. Some of the northern most trench-parallel measurements in region L2 would be the most susceptible to influence of the trench-parallel flow as they are nearest the slab edge. Furthermore, Mehl et al. (2003) identify fabrics from exhumed mantle rocks found in the nearby Talkeetna arc and advocate that they are a product of along arc flow in the mantle wedge. However, the sharp transition from trench-perpendicular in the backarc to trench-parallel in the forearc seems to favor B-type olivine in the nose as the source of trench-parallel anisotropy. This is further supported by the large distance from the slab edge to most of the trench-parallel measurements in region L2. We do not have observations near the slab edge that would provide insight into the existence or nonexistence of 3D flow, but the geodynamic 3D mantle flow predictions align well with the fast directions of regions L1a, L2 (if B-type olivine), and L1b. This seems to favor the Long & Silver (2008) model with contributions of B-type olivine in the nose and anisotropic slab lithosphere. Without considering the geodynamic modeling (Jadamec & Billen, 2010) nor the previous SKS splitting study of Venereau et al. (2019), we would not include 3D corner flow in our preferred model. Thus, the local splitting observations alone would support simple 2D corner flow with B-type olivine in the nose and anisotropy in the slab lithosphere (Figure 2.39).

2.5.2 SKS

The pattern in region T3 (see Section 2.4.4) has been observed in all the previous SKS studies in Alaska (Christensen & Abers, 2010; Hanna & Long, 2012; Perttu et al., 2014; McPherson et al., 2017; Venereau et al., 2019; McPherson et al., 2020) and persists northwest toward the ~70 km subduction interface contour in the flat slab region northwest of Cook Inlet. The ray paths in region T3 do not travel through the mantle wedge but rather have major parts in the subslab mantle and minor parts in the slab and overriding plate. Therefore, the splitting must be related to one or some combination of anisotropy beneath (Song & Kawakatsu, 2012, 2013) or within the subducting Pacific plate or structure in the overriding plate. This splitting pattern does not parallel the north-south magnetic lineations of the Pacific sea floor that we used as evidence to potentially attribute anisotropy in the slab to some of the trench-parallel local measurements. Furthermore,

crustal contributions to SKS splitting are generally thought to be minimal (∼0.1 s) (Savage, 1999) whereas upper mantle contribution is much larger (∼ 1 s) (Silver, 1996; Fouch & Rondenay, 2006). Nearly all of the measurements here have $\delta t \geq 1$ s and some are longer than 2 s. The long delay times suggest that the main source of anisotropy is not in the overriding plate nor the lithosphere of the subducting slab. Song & Kawakatsu (2012) show that oceanic asthenosphere characterized by weak azimuthal and strong radial anisotropy will have fast directions parallel to the plate motion direction where the slab dip is shallow. The long delay times, nearly horizontal slab, and parallel relationship between ϕ and the plate convergence direction suggest that the mostly likely source of anisotropy beneath region T3 is flow in the asthenosphere related to subduction of the Pacific plate (Figures 2.2 and 2.3). However, we do not rule out contribution from the subducting lithosphere and overriding plate, especially because of the similar fast directions observed from local events (L3) in this region that do not sample subslab asthenosphere (Figures 2.38 and 2.39).

Most measurements in region T2 are trench-parallel although there is some scatter in the fast directions. The most coherent trench-parallel pattern is seen south of the SALMON transect. The scatter increases to the north and is strongest at Spurr volcano (-152.25° 61.30°). The trench-parallel pattern is certainly less coherent in the Cook Inlet back arc for the SKS datasets in the study and previous studies (Figure 2.19). Previous SKS studies interpret trench-parallel flow in the mantle wedge here and for nearly all of the Alaska subduction zone, but seem to extrapolate this interpretation to Cook Inlet from the consistent trench-parallel fast directions in the adjacent backarcs (flat slab subduction region to the northeast and the Aleutians to the southwest) (McPherson et al., 2017; Venereau et al., 2019). The ray paths for region T2 travel through all components of the subduction system (overriding plate, mantle wedge/nose, subducting plate, and subslab mantle). Region T2 roughly corresponds to parts of regions L1a and L2 from the local splitting dataset. Just as previously discussed in local region L2, the trench-parallel splitting pattern can be explained by many different anisotropic sources. Both our local and SKS splitting results here could be explained by any combination of trench parallel anisotropy in the slab, along arc flow in the wedge, 2D corner flow with B-type olivine in the mantle nose, etc. 2D corner flow with B-type olivine in the mantle nose was suggested by the local splitting pattern in this region and could potentially contribute to the SKS splitting here. However, several measurements have significantly large delay times ($\delta t \geq 3s$) and this requires more anisotropy than can be found in the subducting slab, mantle wedge, and overriding plate. This emphasizes the importance of the subslab segment of the SKS ray path to these splitting observations. The anisotropy, at least for the larger delay times, likely lies in the subslab asthenosphere/mantle. This is fortified by results from region T3 suggesting strong anisotropy from flow in the subducting Pacific asthenosphere. The paradox in this interpretation is that the fast directions in regions T3 and T2 are nearly perpendicular to each other

yet have the same source of anisotropy. This would mean that the fast directions in the subducting asthenosphere would need to change by 90° over a short distance. In region T2 the dip of the subducting slab is much steeper than in region T3. Song & Kawakatsu (2012) show that a change in slab dip can rotate the fast axis in the subslab asthenosphere by 90° with the assumption of a strong radial anisotropy component. Furthermore, Song & Kawakatsu (2013) use this model to explain the sharp 90° transition of SKS splitting fast directions in the flat slab portion of the Alaska subduction zone. An important observation is that the sharp transition in SKS datasets is near the ~75 km slab depth contour in the flat slab region and moves back to ~50 km in Cook Inlet. The transition in Cook Inlet is less prominent in our dataset compared to the previous SKS studies, but appears to exist at ~50 km as well (Figure 2.19). The slab dip is steeper in Cook Inlet and thus Song & Kawakatsu (2012) would predict the sharp change in splitting pattern to occur closer to the trench than in the flat slab region. This is exactly what the jump in splitting transition from ~75 km to ~50 km in the SKS datasets show. Therefore, we agree with Song & Kawakatsu (2013) and interpret the splitting pattern observed in region T2 to have main contributions from flow in the dipping subslab asthenosphere related to Pacific plate motion (Figure 2.3). We also expect minor contributions from anisotropy in the subducting lithosphere and mantle wedge. Any wedge and lithospheric contribution in region T2 would be corroborated by our local splitting results and the notable number of trench-perpendicular measurements all SKS datasets.

Region T1 has ray paths that are strictly in the mantle wedge and overriding plate. While the splitting pattern here is complex, the longest splits and majority of the splits are roughly trench-perpendicular. Leaning on the strong evidence of trench-perpendicular anisotropy from 2D corner flow in the mantle wedge that was observed in the local dataset, we attribute the trench-perpendicular SKS measurements here to the same 2D corner flow. We therefore refute the interpretations from the previous SKS studies for along arc flow in the wedge. Rather, we favor a change in dip of the subslab asthenospheric flow (Song & Kawakatsu, 2013) to explain the transition from plate convergence parallel fast directions in region 1 to trench-parallel fast directions in region 2. However, as was discussed in the local splitting section, we do not rule out potential contributions to trench-parallel splitting from B-type olivine in the mantle nose. Finally, we do not dispute trench-parallel flow in the wedge near the slab edge but our study region is too far away from the edge to see significant influence of this flow (Song & Kawakatsu, 2013; Venereau et al., 2019).

2.5.3 Comparison of local S and SKS

Combining our local S and SKS splitting observations and preferred models leads to our final interpretation of the mantle flow and anisotropic structures in the Cook Inlet segment of the Alaska

subduction zone. For an overall model, we favor 2D corner flow induced by downdip motion of the slab and B-type olivine in the mantle nose combined with flow in the subslab asthenosphere parallel to the subducting plate (Song & Kawakatsu, 2013) and Pacific slab lithosphere anisotropy (Figure 2.40).

Throughout this study we compare SKS and local S results and must acknowledge the many challenges in effectively doing so. The main challenge is that the measurements are typically made in drastically different frequency ranges. It has been well documented that shear-wave splitting parameters are frequency dependent (Marson-Pidgeon & Savage, 1997; Wirth & Long, 2010; Long & van der Hilst, 2006). Other difficulties arise from the different paths that the waves take. Even for overlapping S and SKS ray paths, the SKS wave has traveled the entirety of the mantle before reaching the point where the S wave originates. Allowing the local S rays to have up to 37° incidence angles further increases the difficulty in comparing with SKS splitting because splitting parameters can vary depending on the angle at which the shear wave propagates through an anisotropic material. Thus when comparing non-vertical ray paths of local events to vertical SKS paths in the same region, there may be differences in ϕ and δt. For a given station the ray paths for local and SKS waves may not be at all similar. Therefore, it does not always make sense to compare a single station's measurements for the two phases unless the local rays are nearly vertical, SKS rays overlap, and the anisotropy is thought lie between the local event and the station. Even in the ideal case of overlapping vertical ray paths the SKS waves have much larger Fresnel zones due to their lower frequency energy content. For example, the first Fresnel zone for an SKS wave(dominant period 8-10s) at 50 km depth is ~80km wide (Favier & Chevrot, 2003). This would be much smaller for a 1 second period local S wave. We try to mitigate the issues that arise from attributing anisotropy to specific locations and comparing splitting measurements of the two different phases through the various ways that we project the splitting measurements to the surface and by carefully using the different phases in attempt to constrain anisotropic depth.

Many studies that compare local S and SKS splitting do not perform both of the analyses themselves. Rather they cite previous studies done by other authors at different times and even using different methods. Here we compare SKS and local S splitting results within the same study and using the same method of measurement. In general, our ray paths for local S and SKS phases sample different regions of the mantle wedge and subduction system. When comparing the ray paths for all stations we see some overlap in the ray paths of the two phases, but local waves sample much more slab and wedge than the SKS waves (Figures 2.12 and 2.19). The majority of the SKS measurements are far enough into the forearc that their paths see no mantle wedge. Instead, their ray paths sample the subslab mantle with minor parts in the slab and overriding plate.

Our SKS results do not display the same dominant trench-perpendicular splitting pattern that the local S shows. However, there are several measurements with ray paths dominantly in the mantle wedge along the SALMON line (mostly T1) that are trench-perpendicular. This is also true for previous SKS studies (Venereau et al., 2019; McPherson et al., 2017). The trench-parallel measurements from region L2 and T2 are somewhat consistent for both local S and SKS. However, we favor that the local measurements here are influenced by B-type olivine in the mantle nose while the SKS are dominantly influenced by subslab asthenosphere. Lastly, we note that region L3 and T3 have plate convergence parallel fast directions. Previous SKS studies and this study attribute the pattern in region T3 to subslab flow in the asthenosphere beneath the subducting Pacific plate. The local events (L3) do not sample the asthenosphere and thus there is likely some contribution from the Pacific plate lithosphere and/or overriding crust in both the local and SKS measurements. While region L3 and T3 do have similar splitting patterns, the local dataset only has measurements for the western part of the Kenai Peninsula so we are unable to say how well the rest of region T3's splitting pattern would match with local data.

2.6 Conclusion

We have performed shear-wave splitting analyses in the Cook Inlet region of the Alaska subduction zone for both local S waves from intraslab earthquakes and teleseismic SKS waves. This constitutes the first comprehensive local splitting study in Alaska comprised of a large collection of seismic networks, including SALMON, MOOS, TA, AVO, and permanent stations. Most splitting studies in Alaska have focused on the flat slab subduction region and here we focus on the Cook Inlet subduction region. From these analyses we provide new constraints on mantle flow and anisotropic structures in this region. We note that both the local S and SKS splitting measurements were made with the same method and mostly the same stations. Comparison of our local S and SKS splitting patterns show that they best match where there is no influence from the anisotropic mantle wedge. In general, the two datasets do not show comparable splitting patterns and are likely influenced by different anisotropic structures. Due to the interpretation that the main source of anisotropy in the SKS dataset is beneath the slab lithosphere, it is not surprising that we do not have great agreement between the two phases.

While there is ambiguity in interpreting both of the datasets in terms of a single subduction system model, some concrete conclusions can be made about anisotropy in the Alaska subduction zone. First, the correlation between depth of local event and δt for stations overlying $\geq$50 km of wedge indicates that the mantle wedge is anisotropic. The dominantly trench-perpendicular and plate convergence fast directions for local measurements that sample the wedge suggest 2D corner flow in the arc/backarc (Figure 2.39). The sharp transition to trench-parallel fast directions for

local events sampling the nose indicates the presence of B-type olivine. The trench-parallel forearc and trench-perpendicular back arc local splitting patterns corroborate the observations of Wiemer et al. (1999) and provide much improved data coverage for this region. The large splitting delay times for local ray paths that mainly sample slab indicate that the subducting Pacific lithosphere contains significant anisotropy. Both datasets show plate convergence fast directions at the Kenai Peninsula where there is no underlying mantle wedge. The long delay times, plate convergence parallel fast directions, and sharp 90° rotation coinciding with a change in slab dip observed in the SKS measurements here suggest that the anisotropy is related to subslab Pacific asthenosphere with flow induced by and parallel to the motion of the subducting slab (Song & Kawakatsu, 2013) (Figure 2.3). However, there seems be some contribution from the Pacific lithosphere and/or overriding plate because the local measurements do not sample the subslab region and have similar fast directions. B-type olivine in the mantle nose, subslab asthenospheric flow, trench-parallel flow around the slab edge, and anisotropy in the Pacific lithosphere could all contribute to the trench-parallel pattern proximal to the forearc observed in both datasets. However, B-type olivine and subslab asthenospheric flow most likely explain the local and SKS trench-parallel observations, respectively.

For an overall model, we favor 2D corner flow induced by downdip motion of the slab and B-type olivine in the mantle nose combined with flow in the subslab asthenosphere parallel to the subducting plate (Song & Kawakatsu, 2013) and Pacific slab lithosphere anisotropy to explain the splitting patterns observed in the two datasets (Figure 2.40). Evidence for 3D flow around the slab edge is weak in our dataset, due no data near the slab edge. However, we do not rule out this possibility because of evidence from geodynamic modeling (Jadamec & Billen, 2010), a previous SKS study (Venereau et al., 2019), and our observation of potential competing flow regimes (Long & Silver, 2008) and trench-parallel splitting in the forearc.

Our disagreement with previous SKS studies' interpretation of along arc flow in the wedge is founded on the strong evidence for 2D corner flow in our local splitting dataset. This greatly motivates a local splitting study in the flat slab subduction region of Alaska. The differences in the two phases' splitting patterns and interpreted mantle dynamics sheds light on the importance of combining local and teleseismic datasets when studying subduction zone anisotropy. It also emphasizes the need for a better understanding of the frequency dependence of splitting measurements and sensitivities of each phase.

2.7 Figures

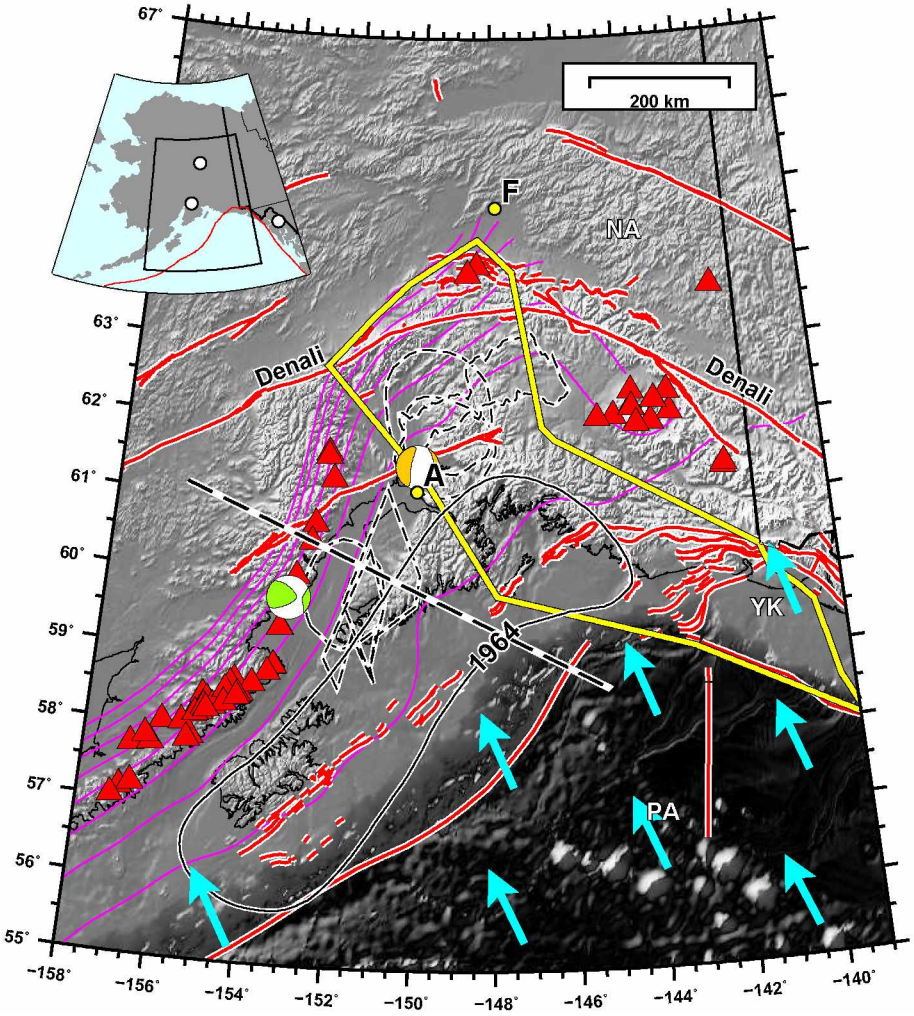

Figure 2.1: Active tectonic setting of the Aleutian-Alaskan subduction zone, south-central Alaska. Cyan arrows show the plate vectors for the subducting Pacific plate (PA) under the North American plate (Argus et al., 2011). Red lines denote active faults (Koehler et al., 2012). Magenta curves are the 40 km to 200 km contours of the subduction interface, i.e., the top of the Pacific plate (Hayes et al., 2018). Yellow bounded region denotes the surface and subsurface extent of the Yakutat block (YK) (Eberhart-Phillips et al., 2006). Red triangles represent active volcanoes. Black dashed lines are inferred slow slip events from various sources (Ohta et al., 2006; Wei et al., 2012; Fu & Freymueller, 2013; Li et al., 2016). Green and white beachball is the seismic moment tensor of the January 24, 2016 M_w7.1 Iniskin earthquake. Yellow and white beachball is the seismic moment tensor of the November 30, 2018 M_w7.1 Anchorage earthquake. Also marked is the aftershock zone of the 1964 M_w9.2 earthquake. Black and white dashed line marks the profile for all cross sections shown in this study.

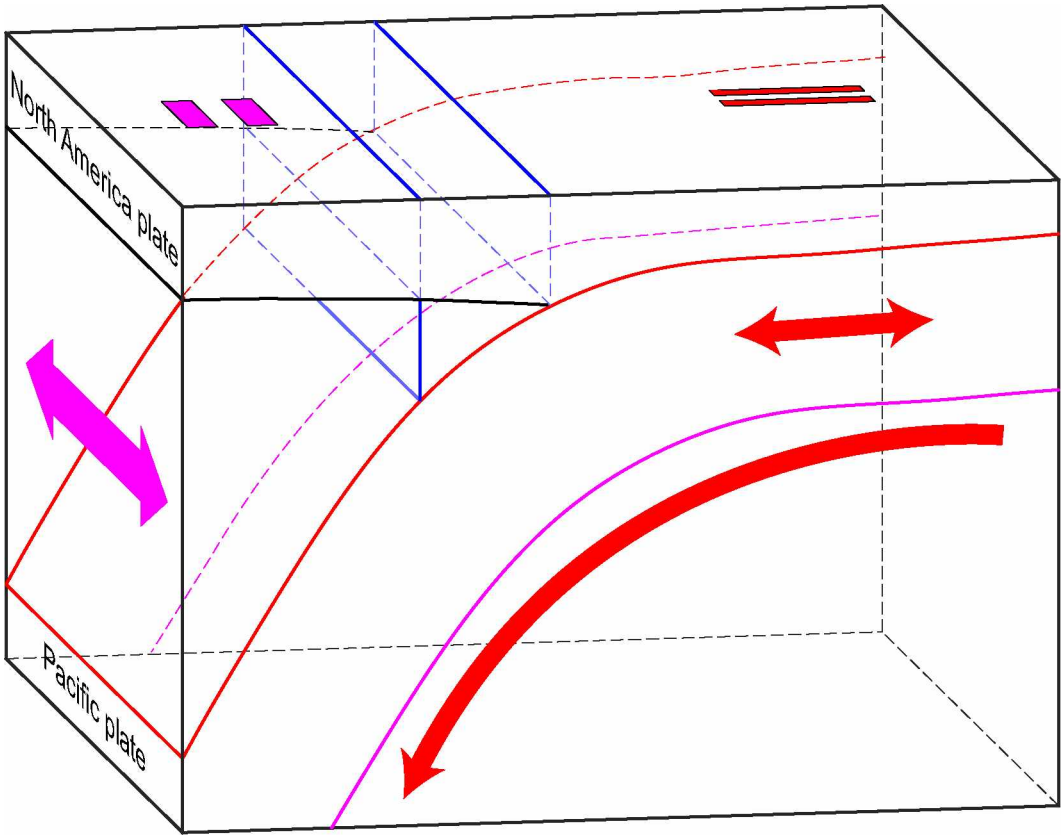

Figure 2.2: 3D Cartoon of the Cook Inlet subduction segment that depicts the observed SKS splitting patterns and interpreted anisotropic structures. The red arrows represent anisotropy in the slab lithosphere and subslab asthenospheric flow. The overlying red bars represent SKS splitting observations that correspond to the red arrows and thus anisotropy in those regions. The 2-headed magenta arrow is trench-parallel flow in the mantle wedge and the overlying magenta bars are the corresponding SKS splitting measurements. The 2D transect shown in Figure 2.1 and Figure 2.6 was used to interpolate to 3D from a cross-section. The top of Pacific plate is from slab 2.0 (Hayes et al., 2018). The blue region represents the mantle nose.

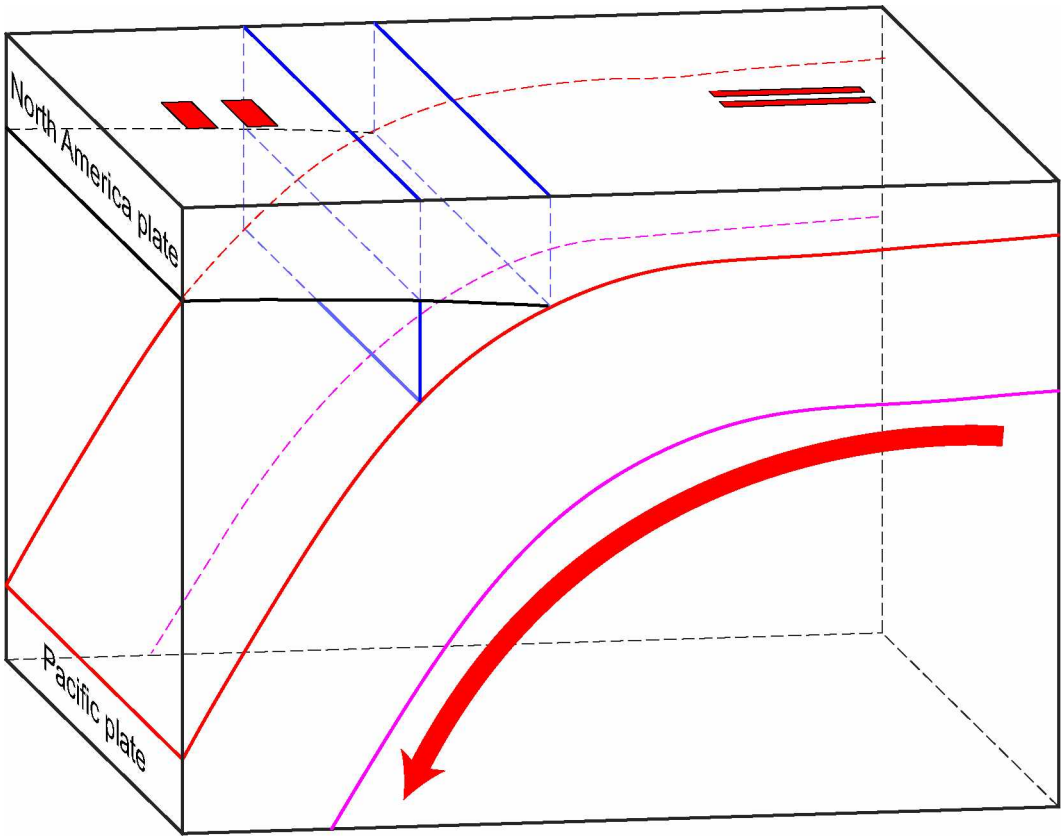

Figure 2.3: 3D Cartoon of the Cook Inlet subduction segment that depicts the observed/predicted SKS splitting patterns and modeled anisotropic structure (Song & Kawakatsu, 2013). The red arrows represent subslab asthenospheric flow. The overlying red bars represent SKS splitting observations and predictions that correspond to the red arrows and thus anisotropy in those regions. Note that the 90° change in observed splitting is due to the change in dip of the subslab asthenospheric anisotropy and that there is no anisotropy in the wedge or Pacific lithosphere. The 2D transect shown in Figure 2.1 and Figure 2.6 was used to interpolate to 3D from a cross-section. The top of Pacific plate is from slab 2.0 (Hayes et al., 2018). The blue region represents the mantle nose.

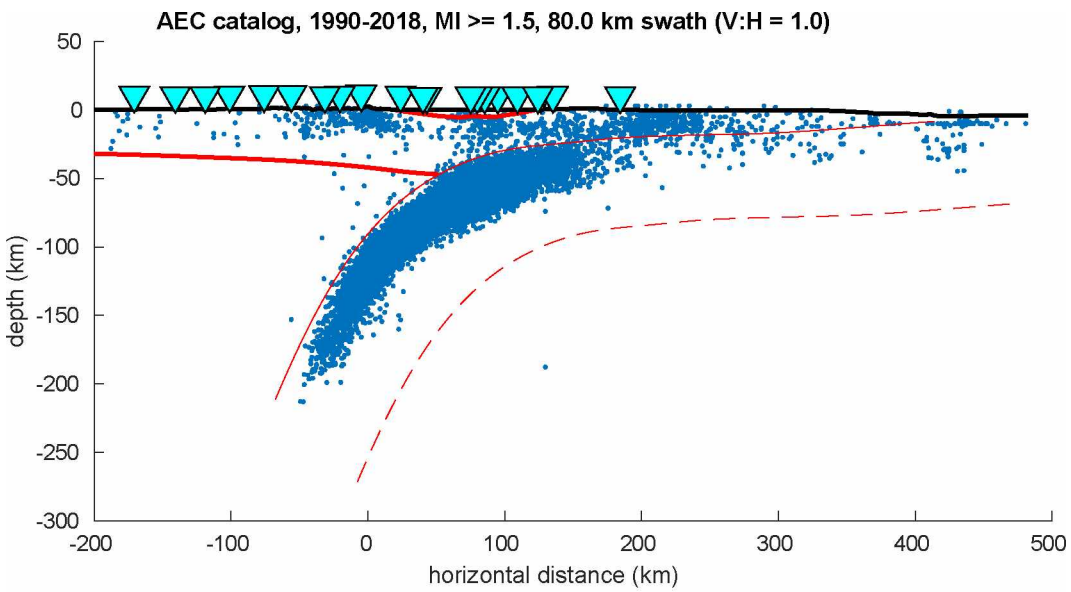

Figure 2.4: Seismicity in Cook Inlet from 1990-2018 shows abundant slab earthquakes. Cyan inverted triangles are SALMON stations. The slab-station geometry provides robust sampling of the mantle wedge and subducting slab. Cross-section line is shown in Figure 2.1 and Figure 2.6.

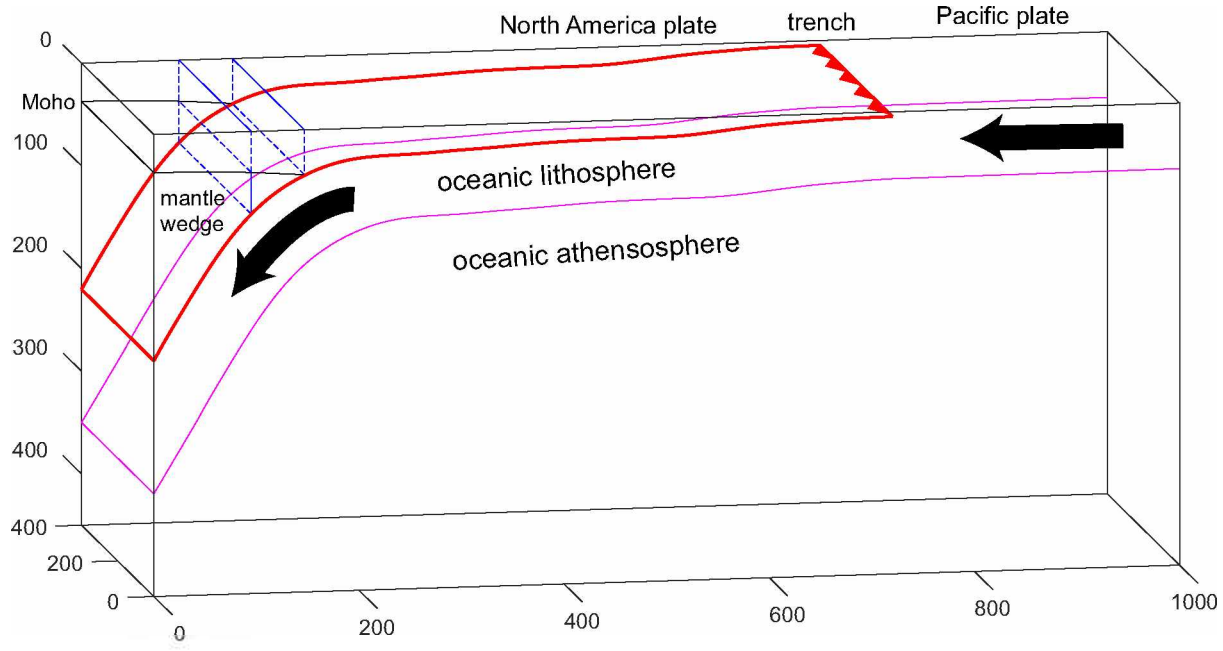

Figure 2.5: Cross section of the Cook Inlet segment of the Alaska subduction zone. Cross section line is shown in Figure 2.1 and Figure 2.6. The slab geometry is slab2.0 (Hayes et al., 2018). Components of the subduction system are labeled and the black arrows depict that the Pacific plate is subducting beneath the North American plate.

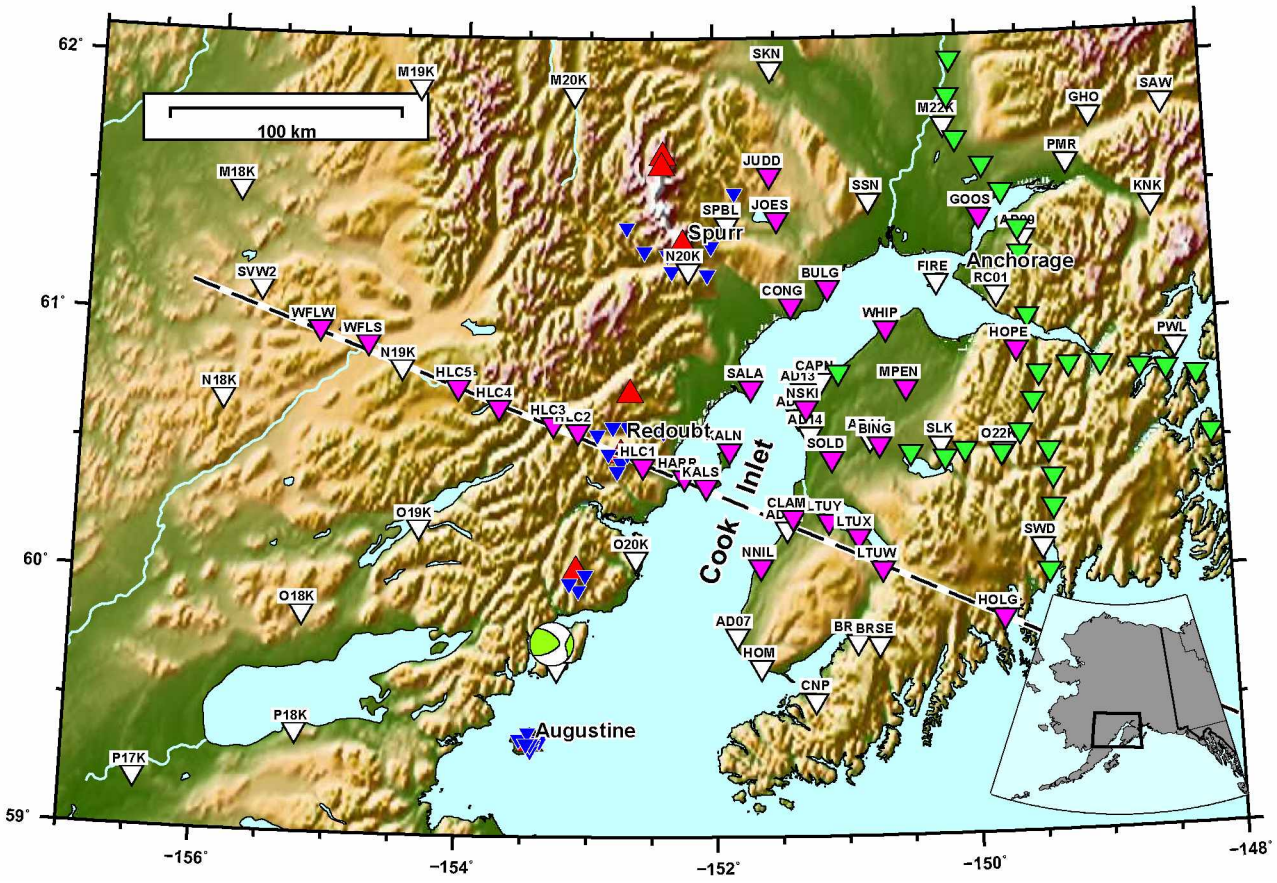

Figure 2.6: SALMON (magenta), MOOS (green), AVO (blue), and TA and permanent network (white) stations in the Cook Inlet region. Red triangles are active volcanoes. Black and white dashed line represents the profile for cross-sections in other figures. Green and white beachball is the seismic moment tensor of the 2016 M_w7.1 Iniskin earthquake.

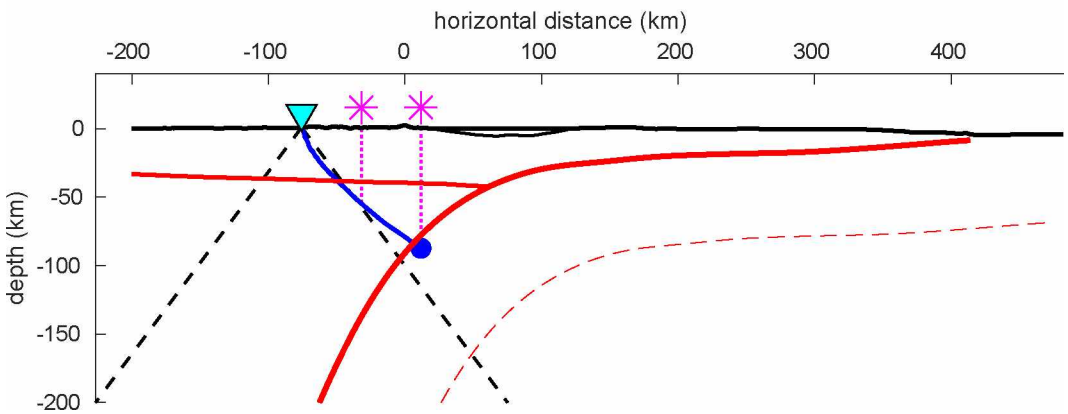

Figure 2.7: Cross section showing each plotting projection and the allowable 37° incidence angle at station HLC5. The pink stars are where the measurements would project for midpoint and event location projection. The blue dot and curve are an earthquake and ray path for a grade A measurement. The black dashed lines mark 37° incidence angles. Note that the event can start outside of 37° but its arriving ray's incidence angle must be $\leq 37°$.

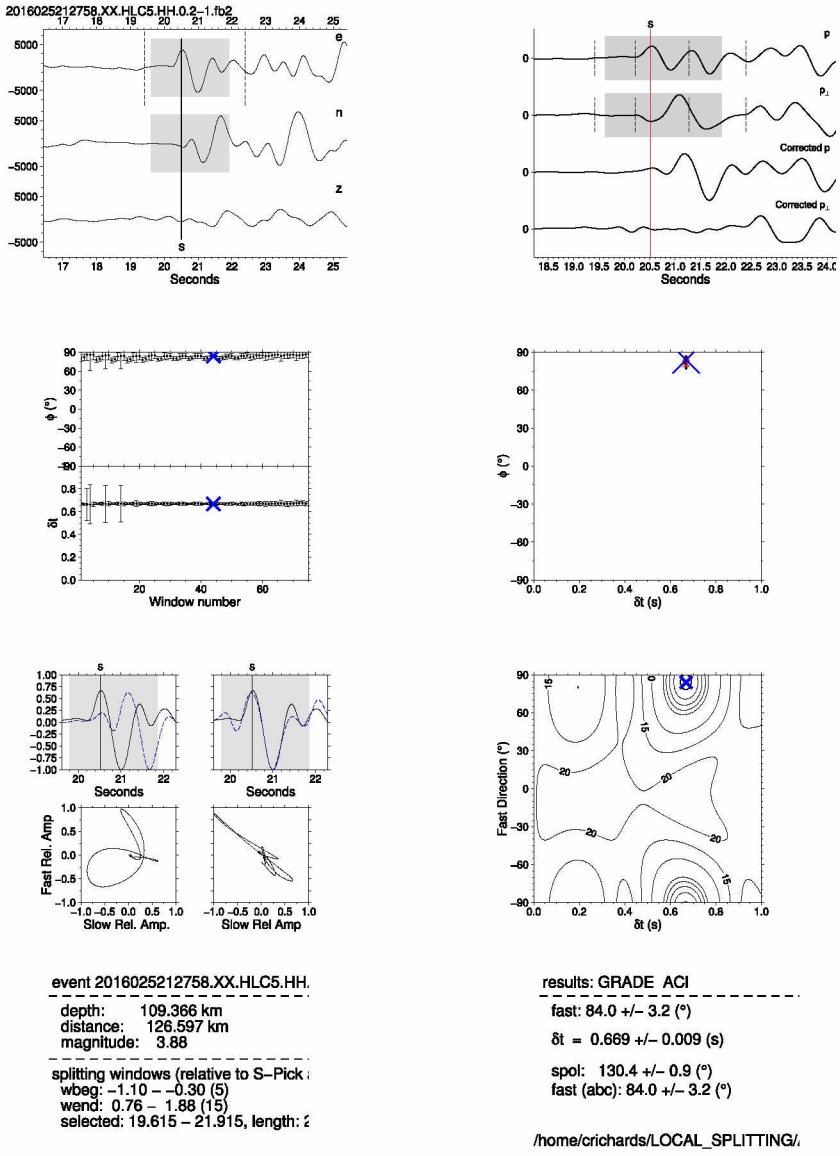

Figure 2.8: High quality, A grade local splitting measurement. Top left is (TL), etc. The grey boxes in panels (TL), (TR) and (BL) delineate the time window used for the final measurement. (TL) filtered East (BL) North (N) and vertical (Z) waveforms. The solid line is the S arrival. The dashed lines are the minimum start and maximum end times for windows used in the processing, as in (TR) . (TR) the waveforms rotated into the SC91-determined (Silver & Chan, 1991) incoming polarization direction (p) and its perpendicular value (p $\perp$), for the original filtered waveform (top) and the waveforms corrected for the SC91-determined dt (bottom) for the window shown in grey. (ML) ϕ and dt determined for each measurement window as a function of window number. (MR) all the clusters of 5 or more measurements, with the large X being the chosen cluster. (BL) waveforms (top) and particle motion (bottom) for the original (left) and corrected (right) waveform according to the final chosen SC91 window. (BR) contours of the smallest eigenvalue of the covariance matrix for the final chosen SC91 measurement.

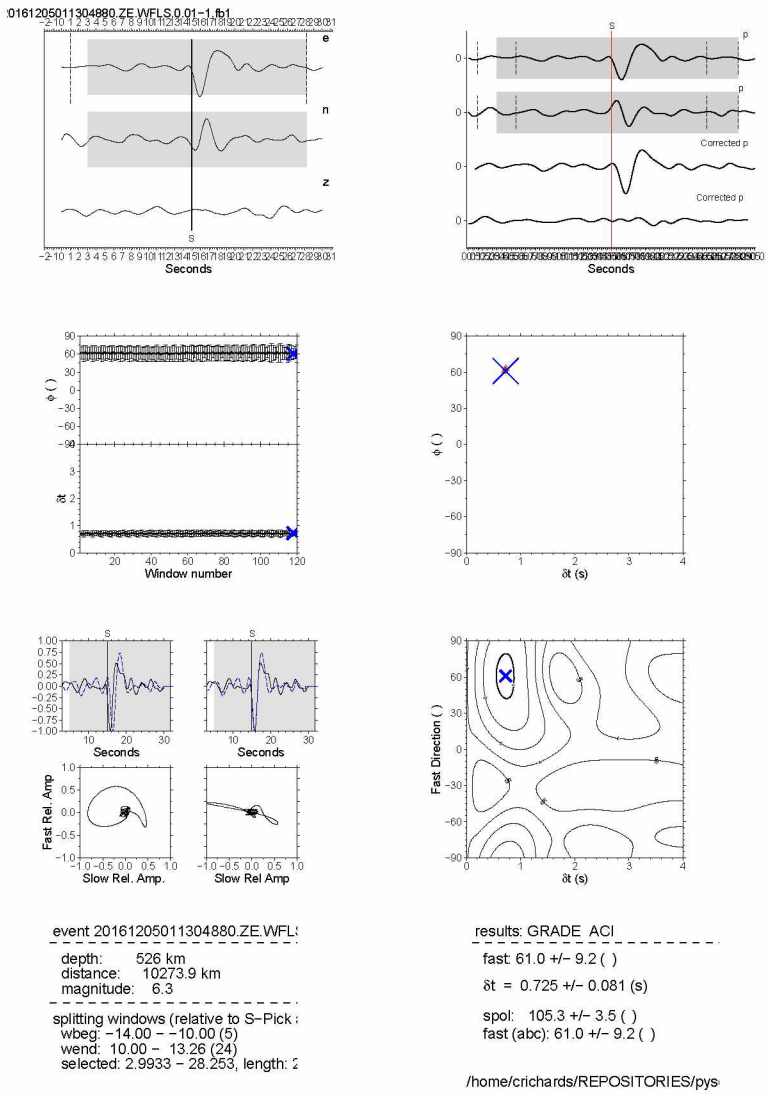

Figure 2.9: High quality, A grade SKS splitting measurement. Top left is (TL), etc. The grey boxes in panels (TL), (TR) and (BL) delineate the time window used for the final measurement. (TL) filtered East (BL) North (N) and vertical (Z) waveforms. The solid line is the S arrival. The dashed lines are the minimum start and maximum end times for windows used in the processing, as in (TR) . (TR) the waveforms rotated into the SC91-determined (Silver & Chan, 1991) incoming polarization direction (p) and its perpendicular value (p $\perp$), for the original filtered waveform (top) and the waveforms corrected for the SC91-determined dt (bottom) for the window shown in grey. (ML) ϕ and dt determined for each measurement window as a function of window number. (MR) all the clusters of 5 or more measurements, with the large X being the chosen cluster. (BL) waveforms (top) and particle motion (bottom) for the original (left) and corrected (right) waveform according to the final chosen SC91 window. (BR) contours of the smallest eigenvalue of the covariance matrix for the final chosen SC91 measurement.

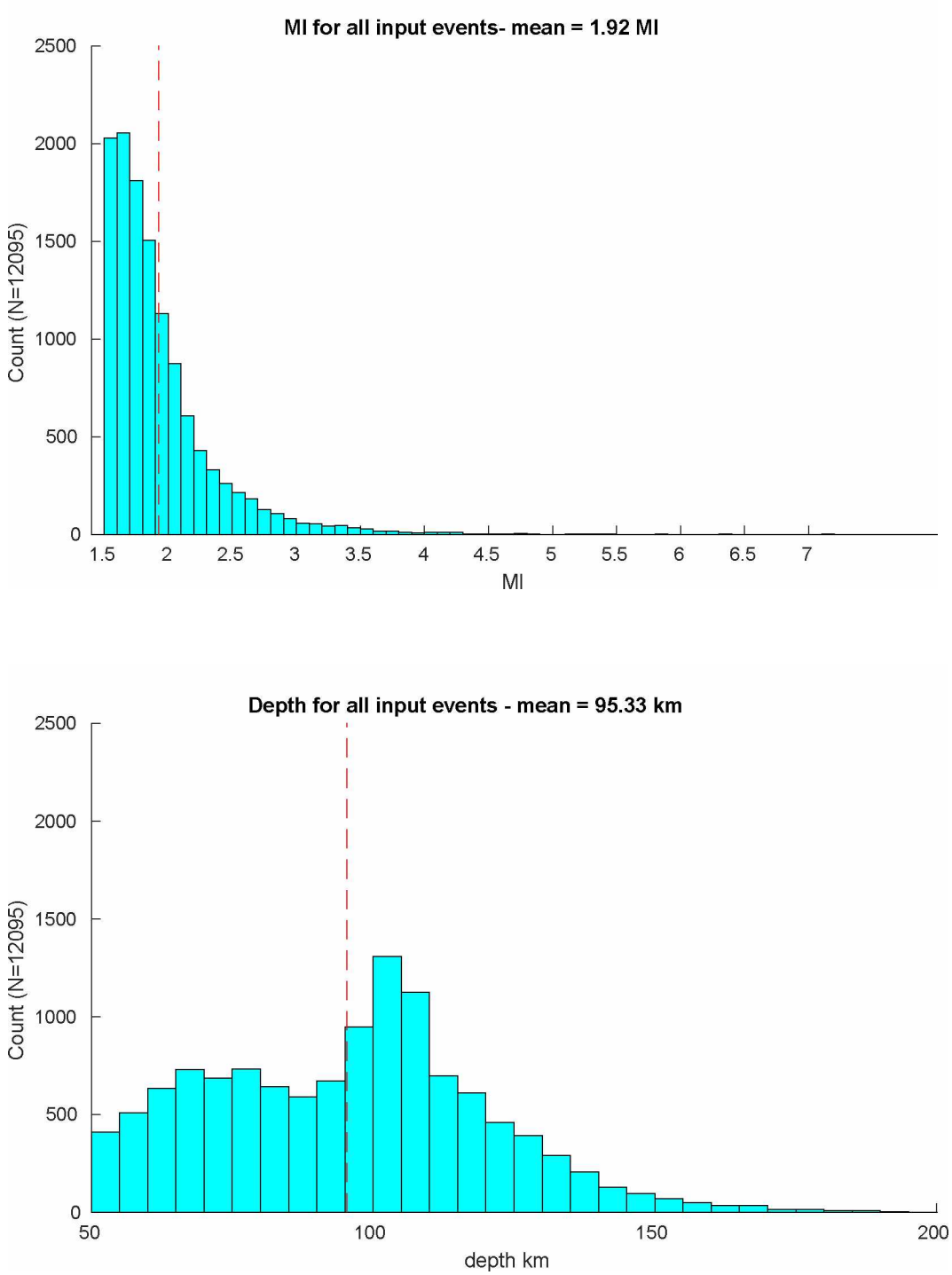

Figure 2.10: Magnitudes (top) and depths (bottom) for all 12095 local S earthquakes considered for splitting analysis. Vertical red dashed lines mark the means.

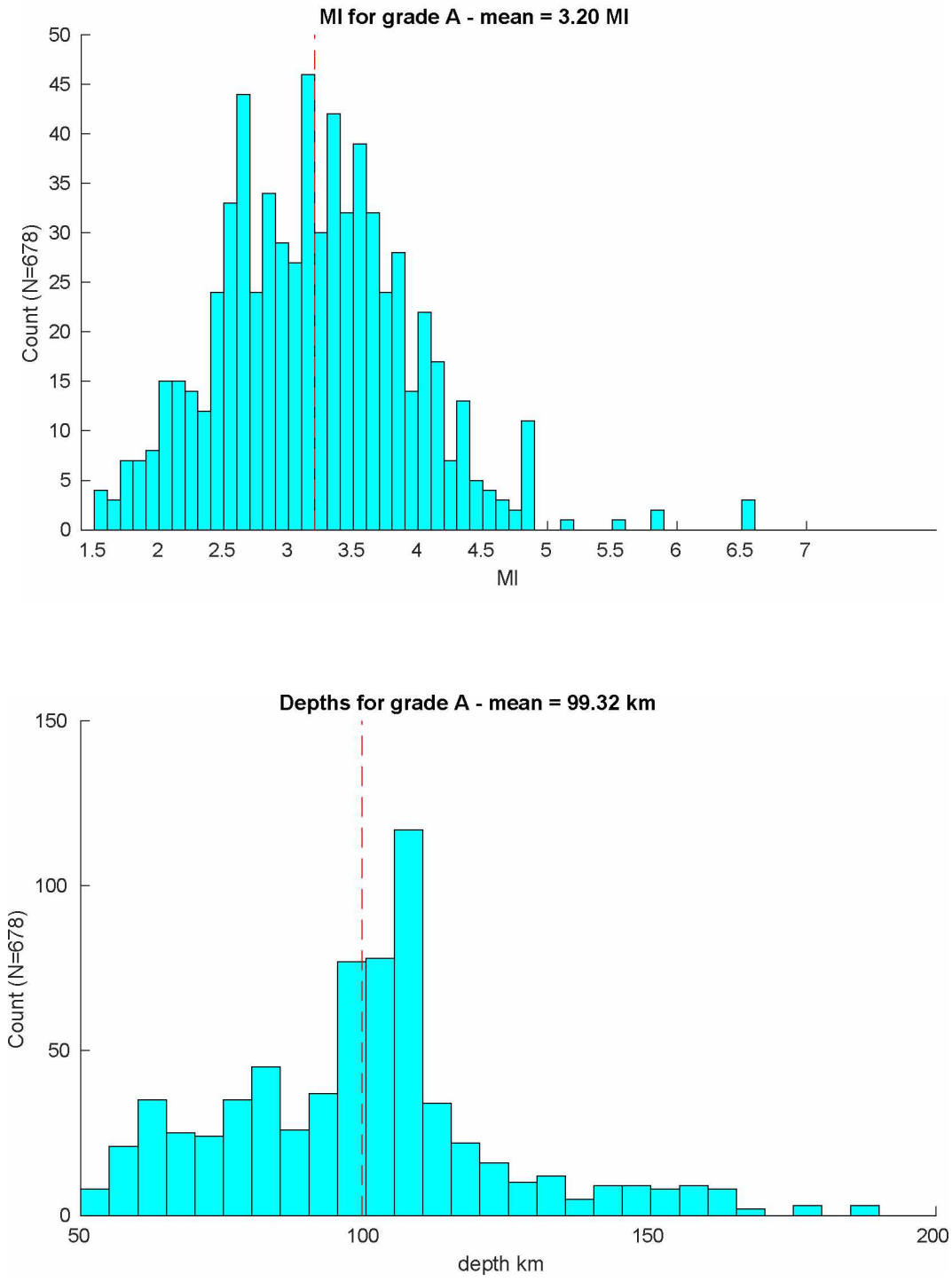

Figure 2.11: Magnitudes (top) and depths (bottom) for all 678 high-quality local S measurements that pass the grading criteria (high SNR, low uncertainty in ϕ, unique solution, and incidence angles $\leq 37^{\circ}$). Vertical red dashed lines mark the means.

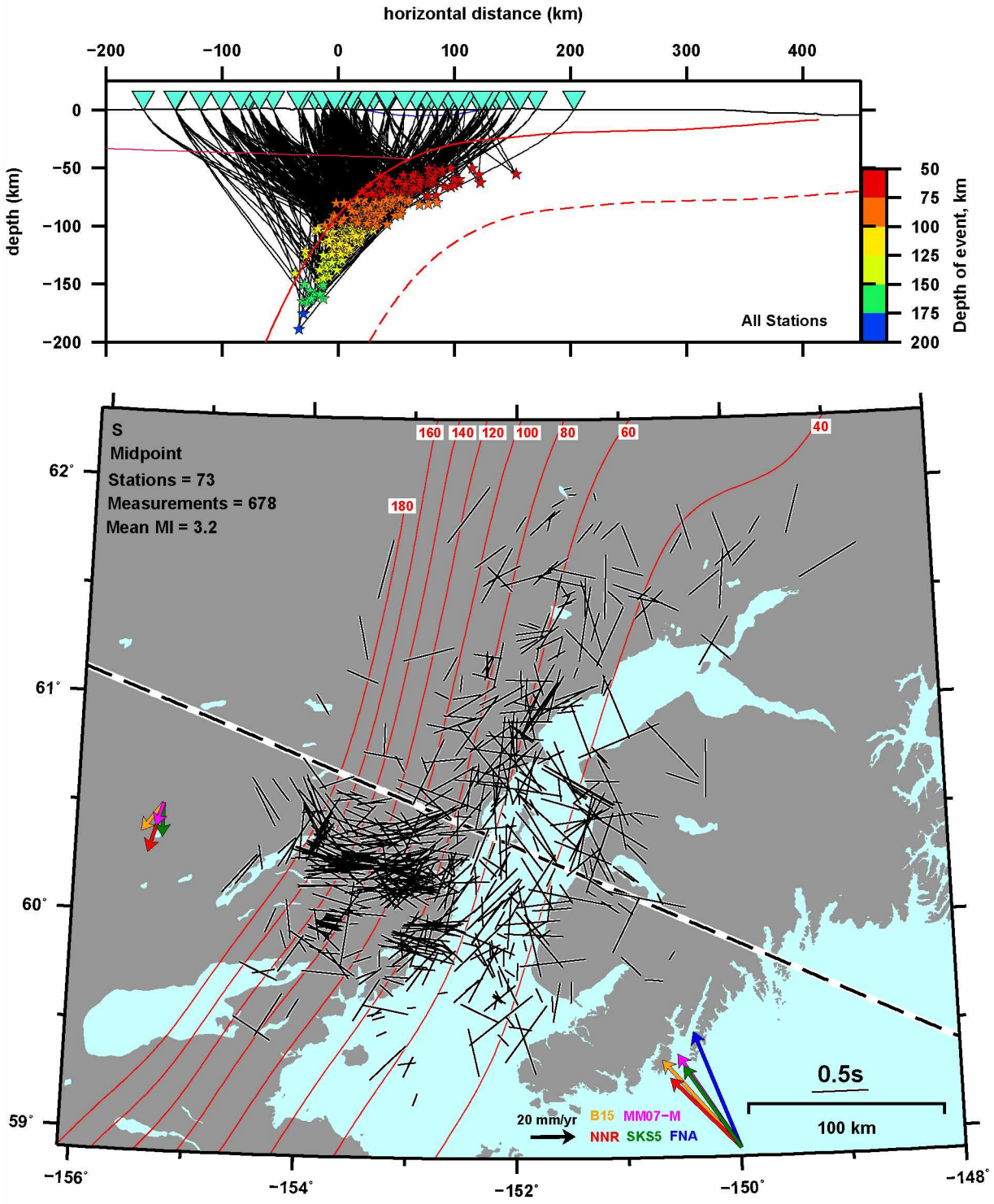

Figure 2.12: Splitting measurements from local intraslab earthquakes in this study.

Figure 2.12: (Continued) (top) Ray paths for all measurements, projected into the cross section shown at bottom. The solid red line is the subduction interface (Hayes et al., 2018). Magenta line is the continental Moho (Miller & Moresi, 2018). Blue line is the Cook Inlet sedimentary basin (Shellenbaum et al., 2010). Inverted triangles are stations. Stars are earthquakes colored by depth. Black lines leading from event to station are ray paths. Dashed red line is the approximate bottom of the subducting oceanic lithosphere. (bottom) Midpont projection of all local splitting measurements. Black bars are individual splitting measurements with orientation parallel to ϕ and length scaled to δt. The red contours indicated the depth to the slab interface and range from 40 km to 180 km. Black and white dashed line represents the cross section seen above. Plate motion vectors: B15 (yellow) spreading alignement (Becker et al., 2015), MM07-M (magenta) modified hotspot (Morgan & Morgan, 2007; Doubrovine et al., 2012), NNR (red) no-net-rotation MORVEL (Argus et al., 2011), SKS5 (green) SKS shear-wave splitting (Becker et al., 2015), FNA (blue) fixed North America in MORVEL (Argus et al., 2011).

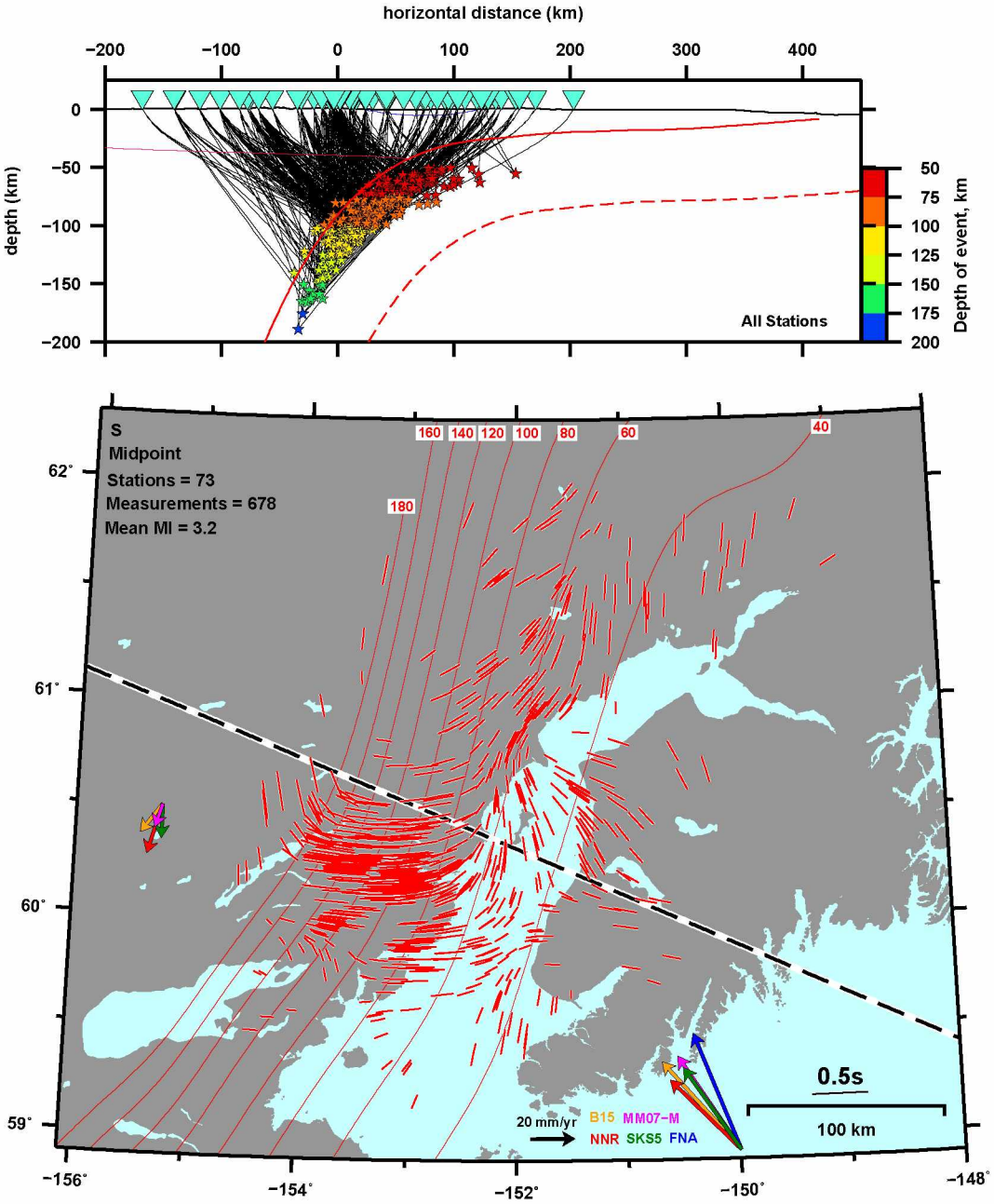

Figure 2.13: Spatially averaged local splitting measurements plotted at the station-event midpoints.

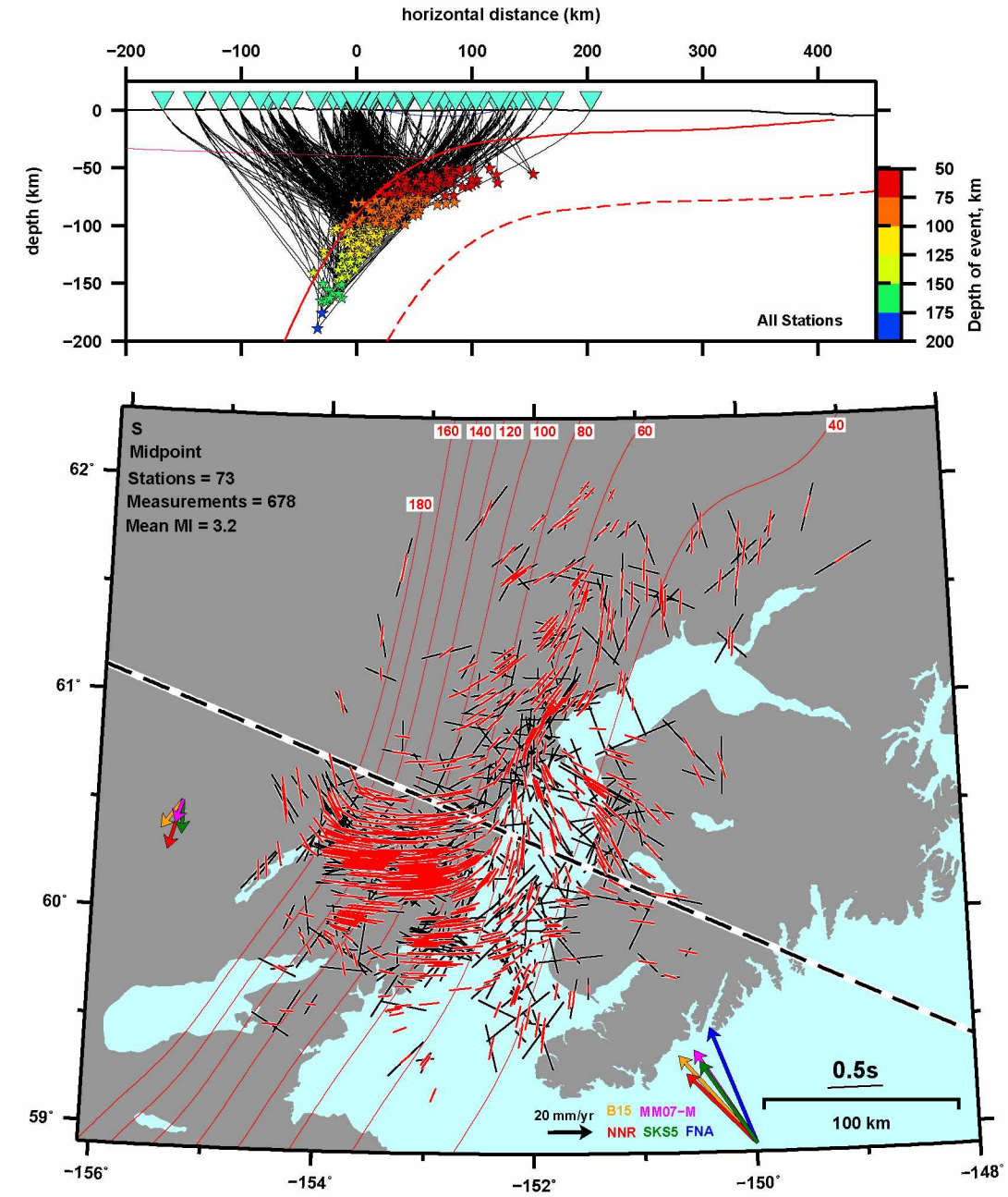

Figure 2.14: Local splitting measurements with spatially averaged measurements in red and data in black.

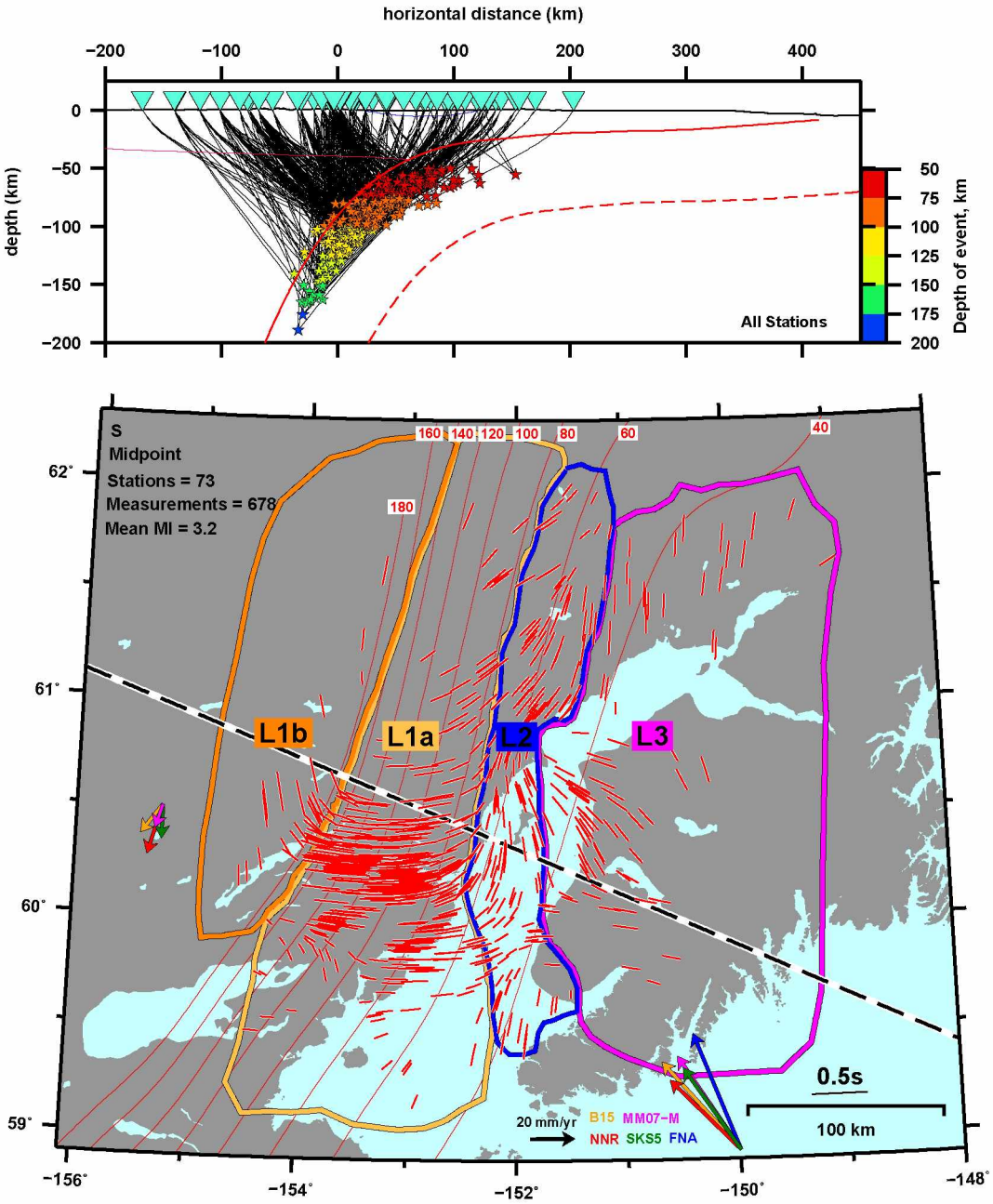

Figure 2.15: Spatially averaged local splitting measurements with interpreted regions outlined. The regions, from west to east, are: L1b (orange), L1a (yellow), L2 (blue), L3 (magenta).

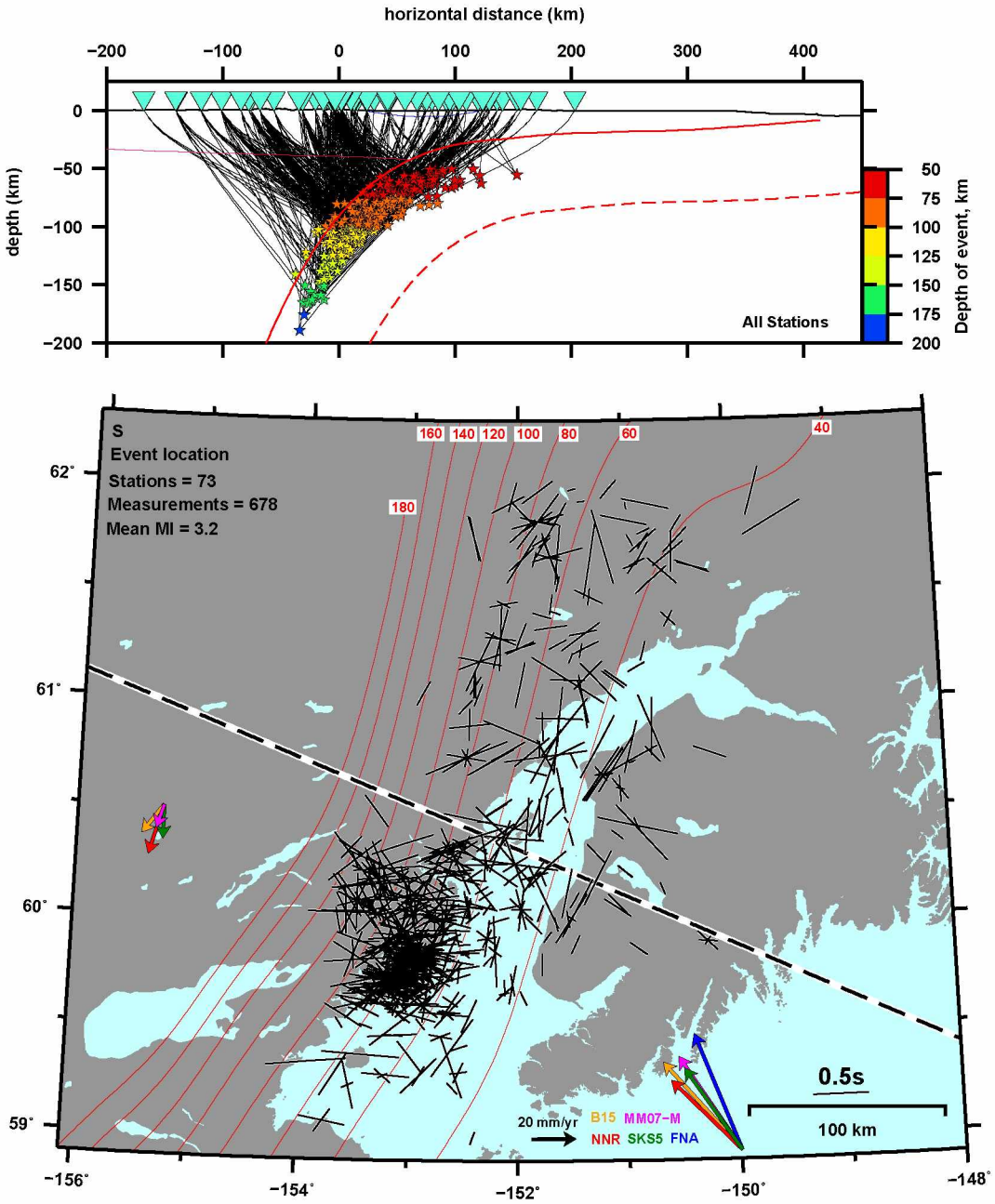

Figure 2.16: Local splitting measurements plotted at events rather than at the event-station midpoints.

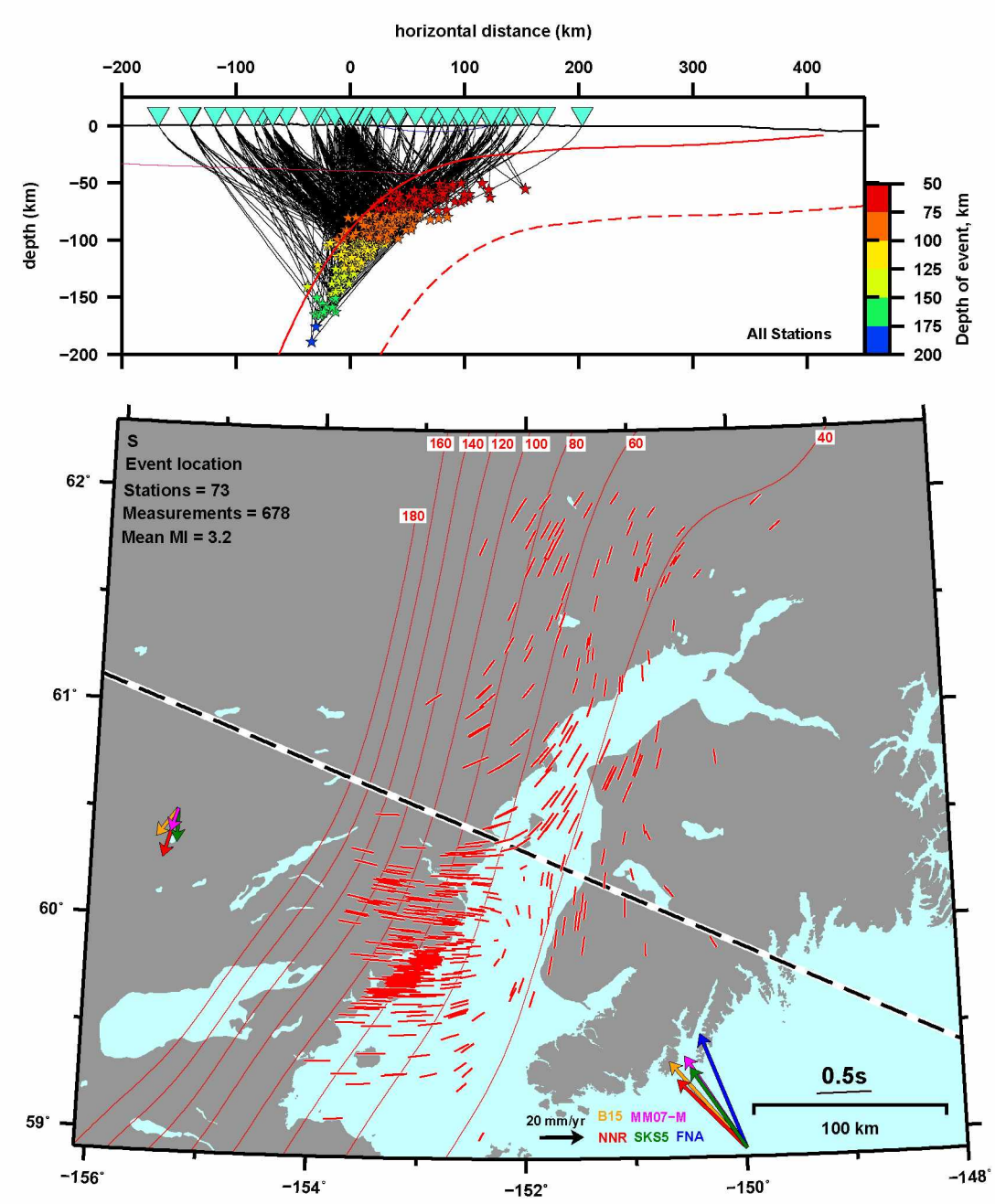

Figure 2.17: Spatially averaged local splitting measurements plotted at the event rather than at the event-station midpoint.

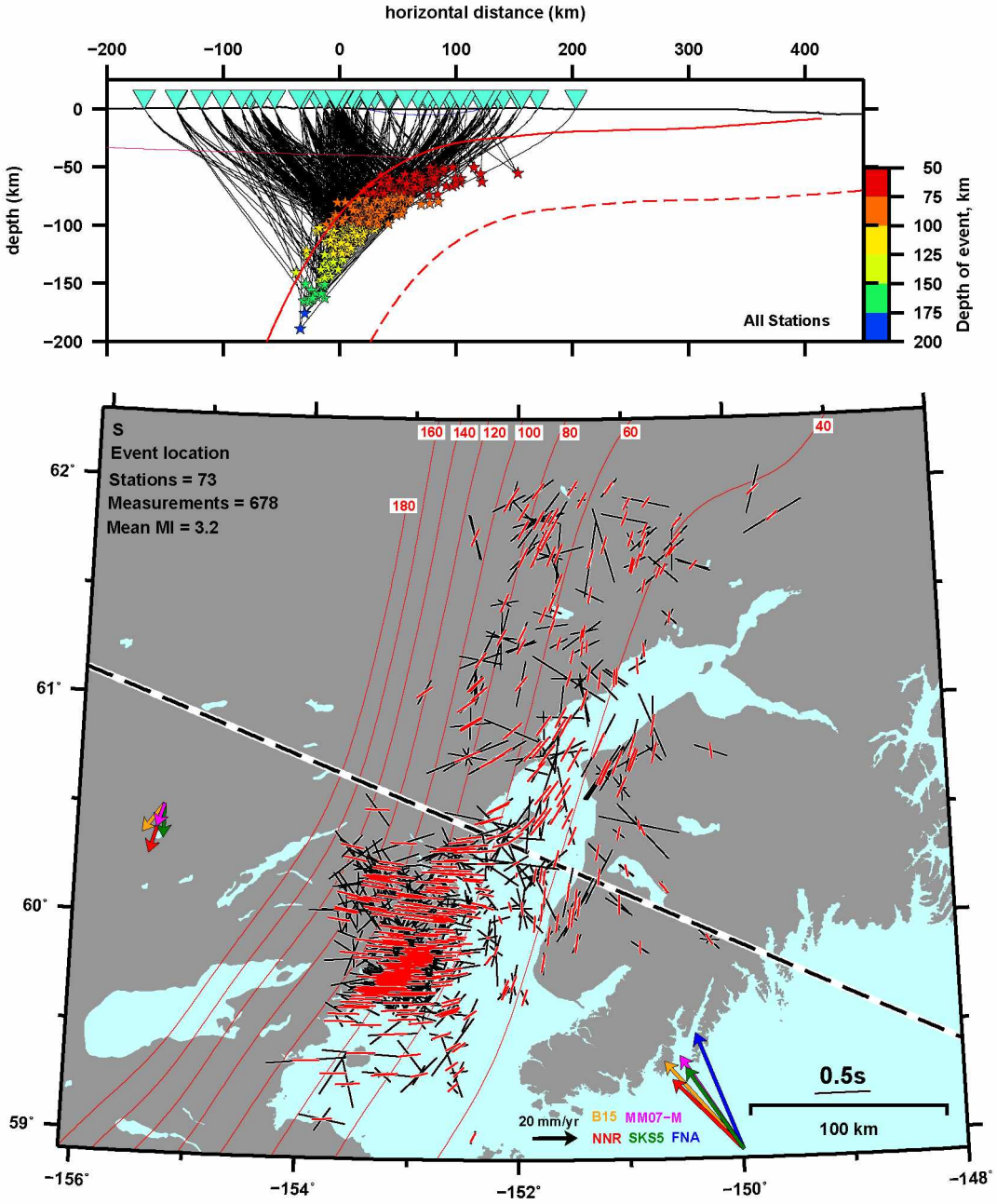

Figure 2.18: Local splitting measurements plotted at the event rather than at the event-station midpoint with spatially averaged measurements in red and data in black.

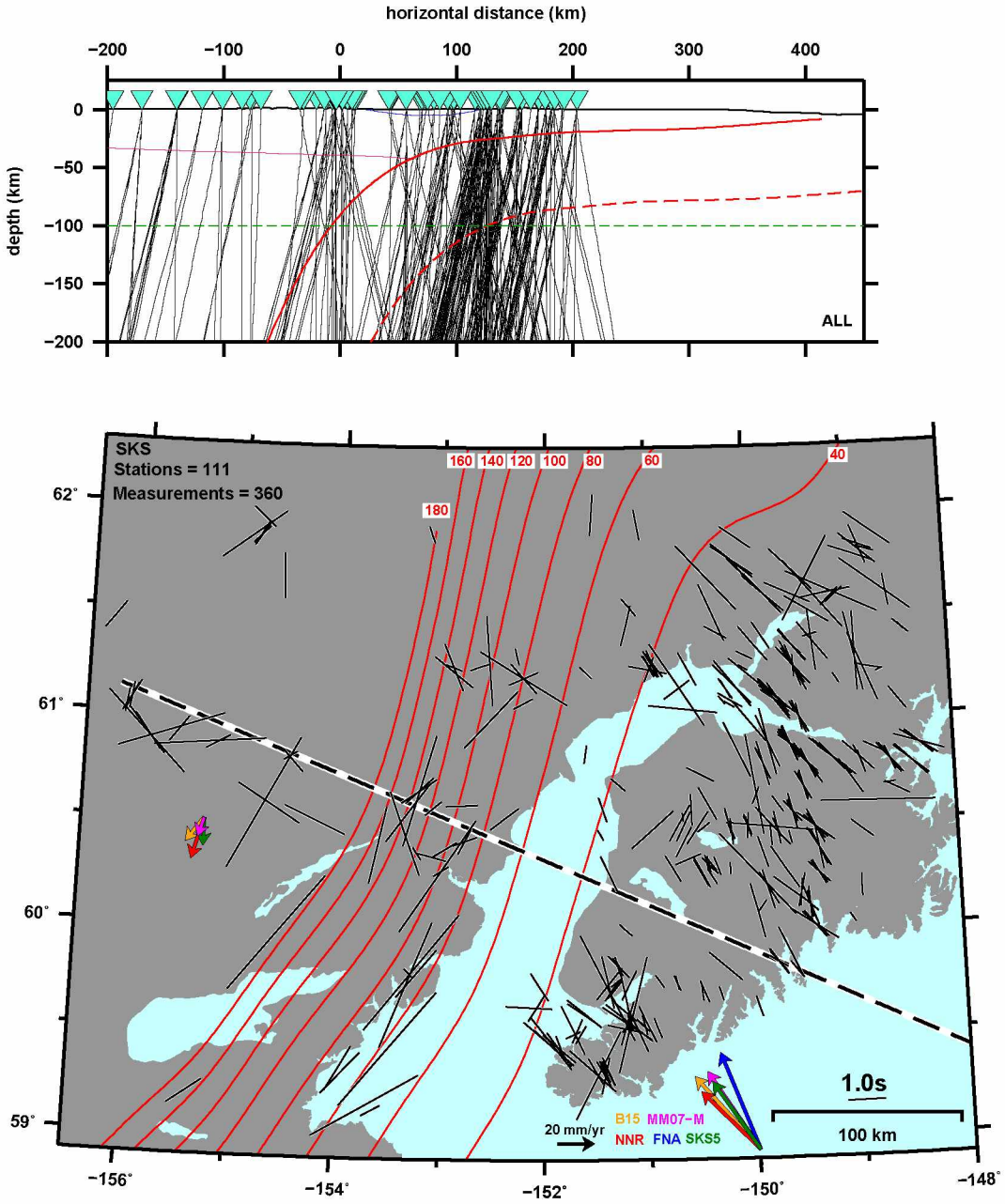

Figure 2.19: (Top) Cross section for showing the subduction profile and the ray paths for high quality SKS splitting measurements. The solid red line is the the slab. Pink line is the Moho. Blue line is the Cook Inlet basin. Rough black line is the surface topography. Inverted triangle is the station with its name displayed to the left. Black lines leading to station are ray paths. Dashed red line is the approximate bottom of the subducting oceanic lithosphere. The green dashed line at 100 km depth shows where the splitting measurement is projected to in the map below. (Bottom) Black bars are individual SKS splitting measurements with orientation parallel to ϕ and length scaled to δt. Black and white dashed line represents the cross section seen above.

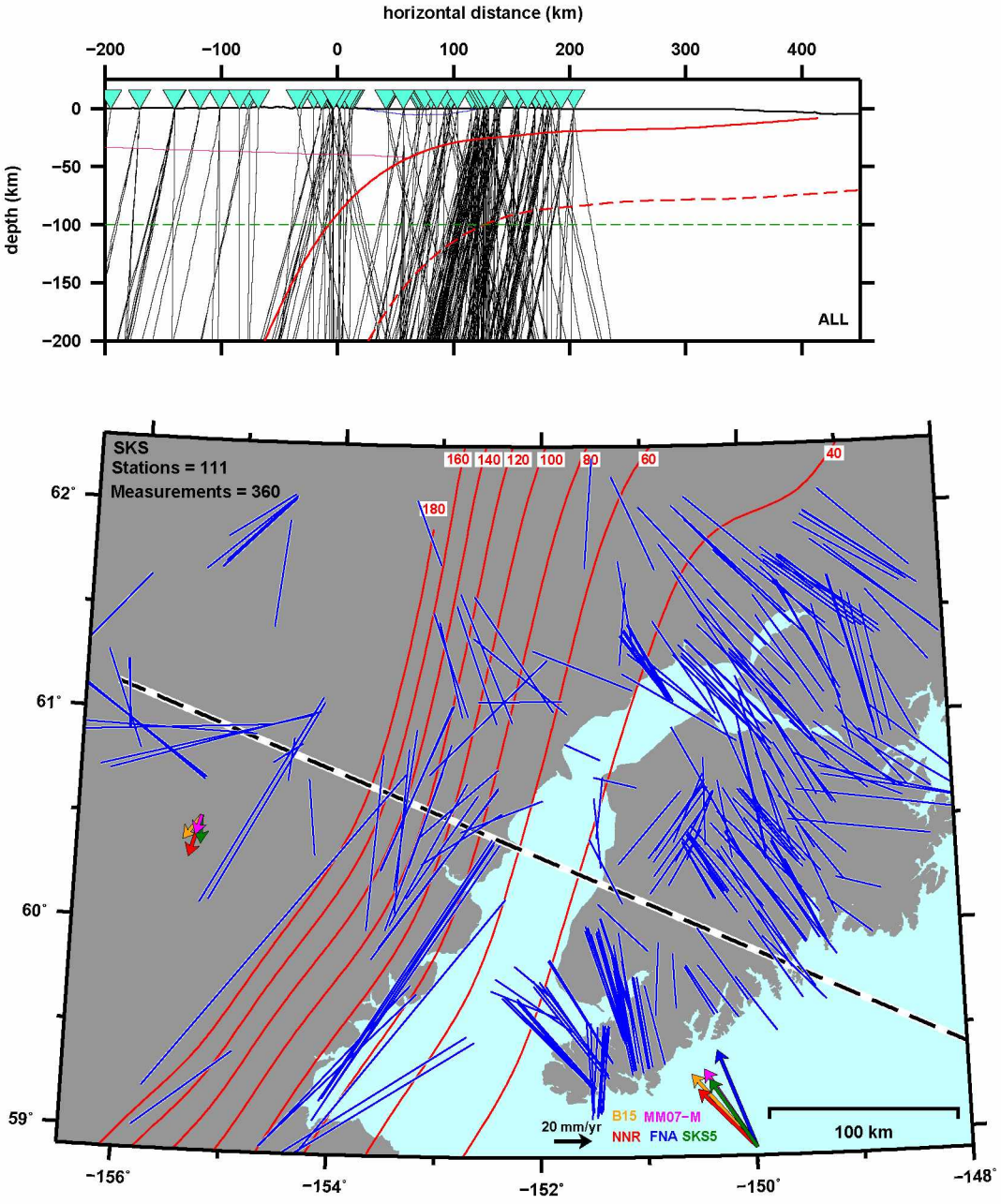

Figure 2.20: Spatially averaged SKS splititng measurements projected to 100 km depth.

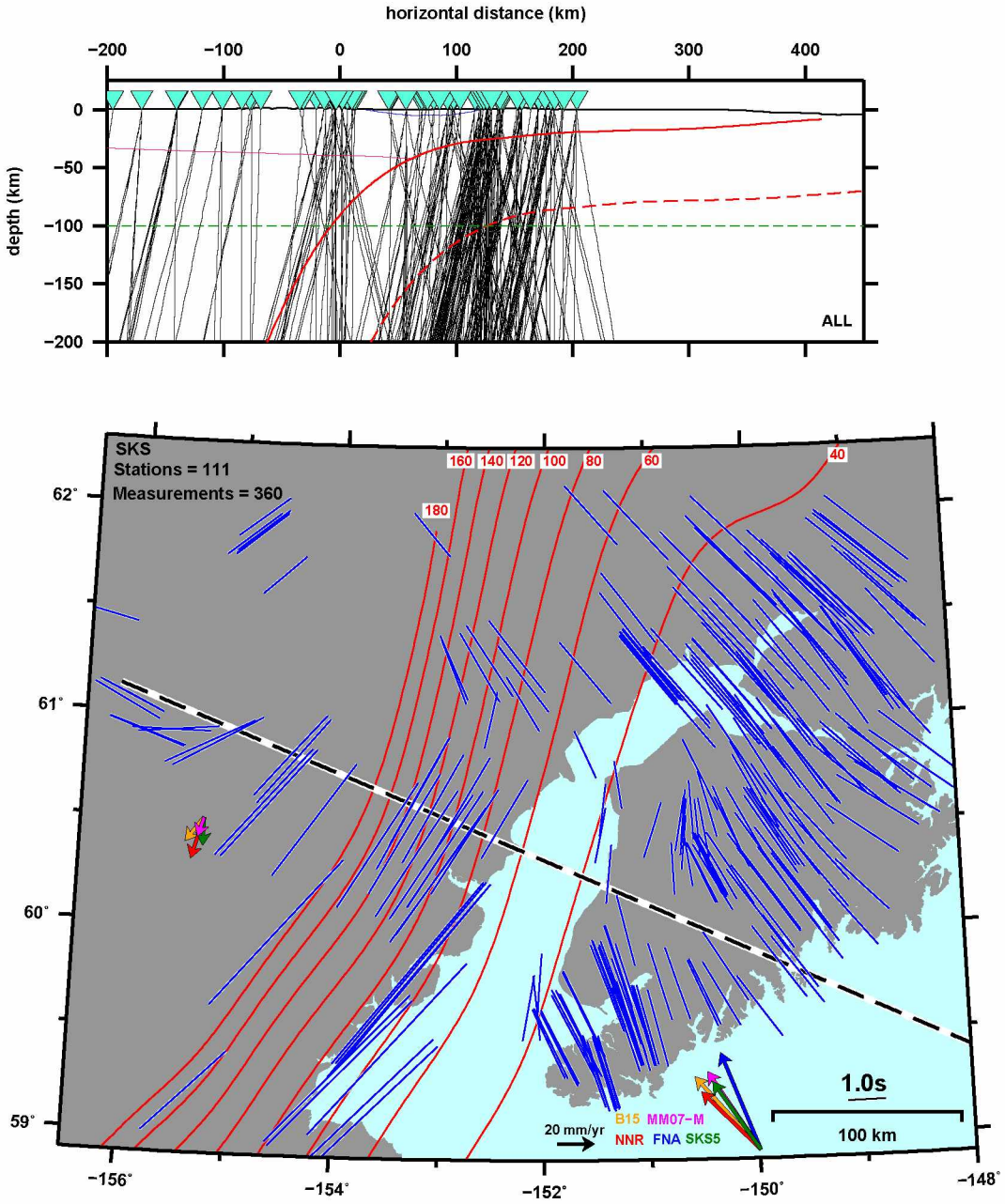

Figure 2.21: Spatially averaged SKS splititng measurements projected to 100 km depth with strong smoothing.

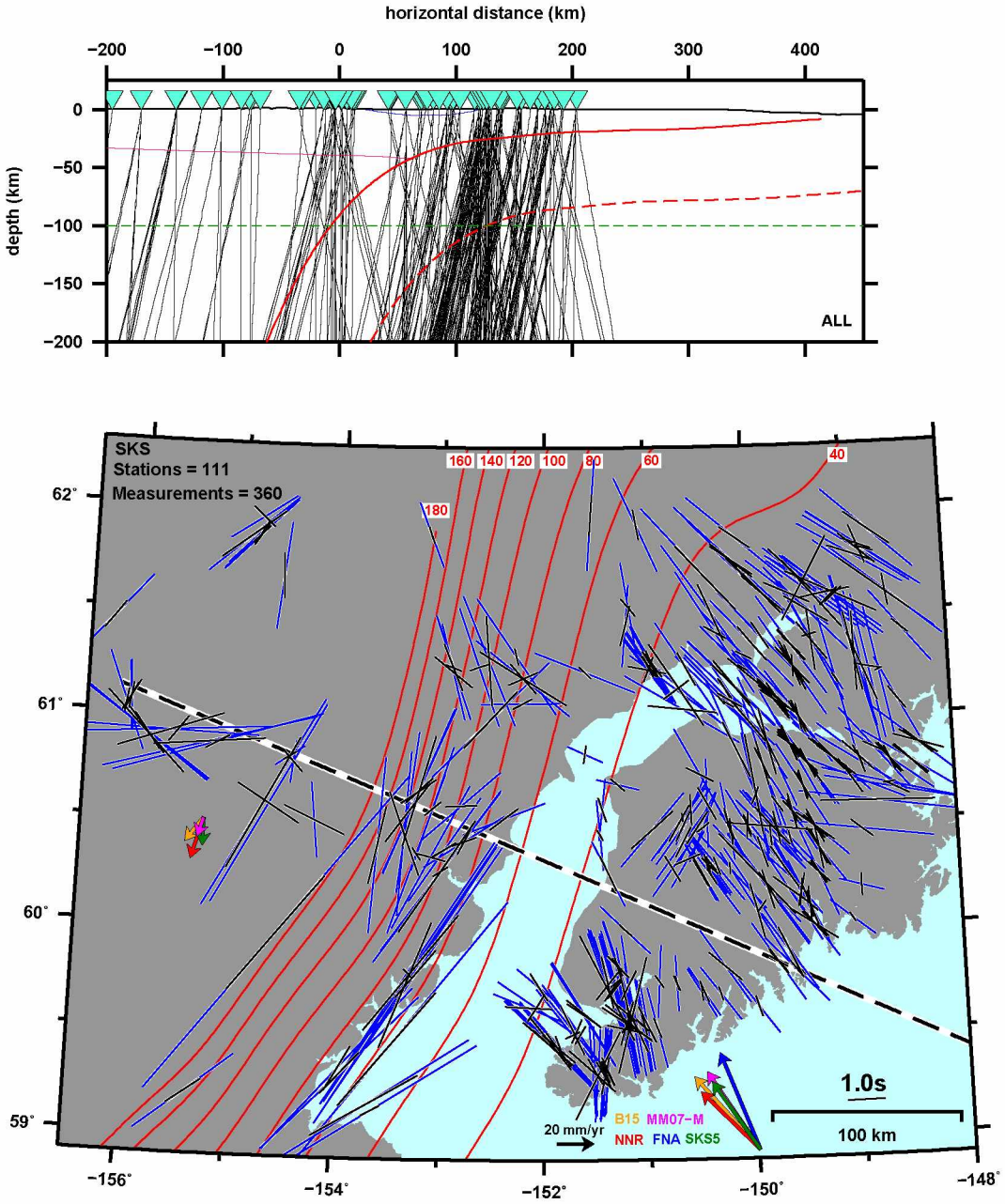

Figure 2.22: Spatially averaged SKS splitting measurements in blue and data in black. The measurements are projected to 100 km depth.

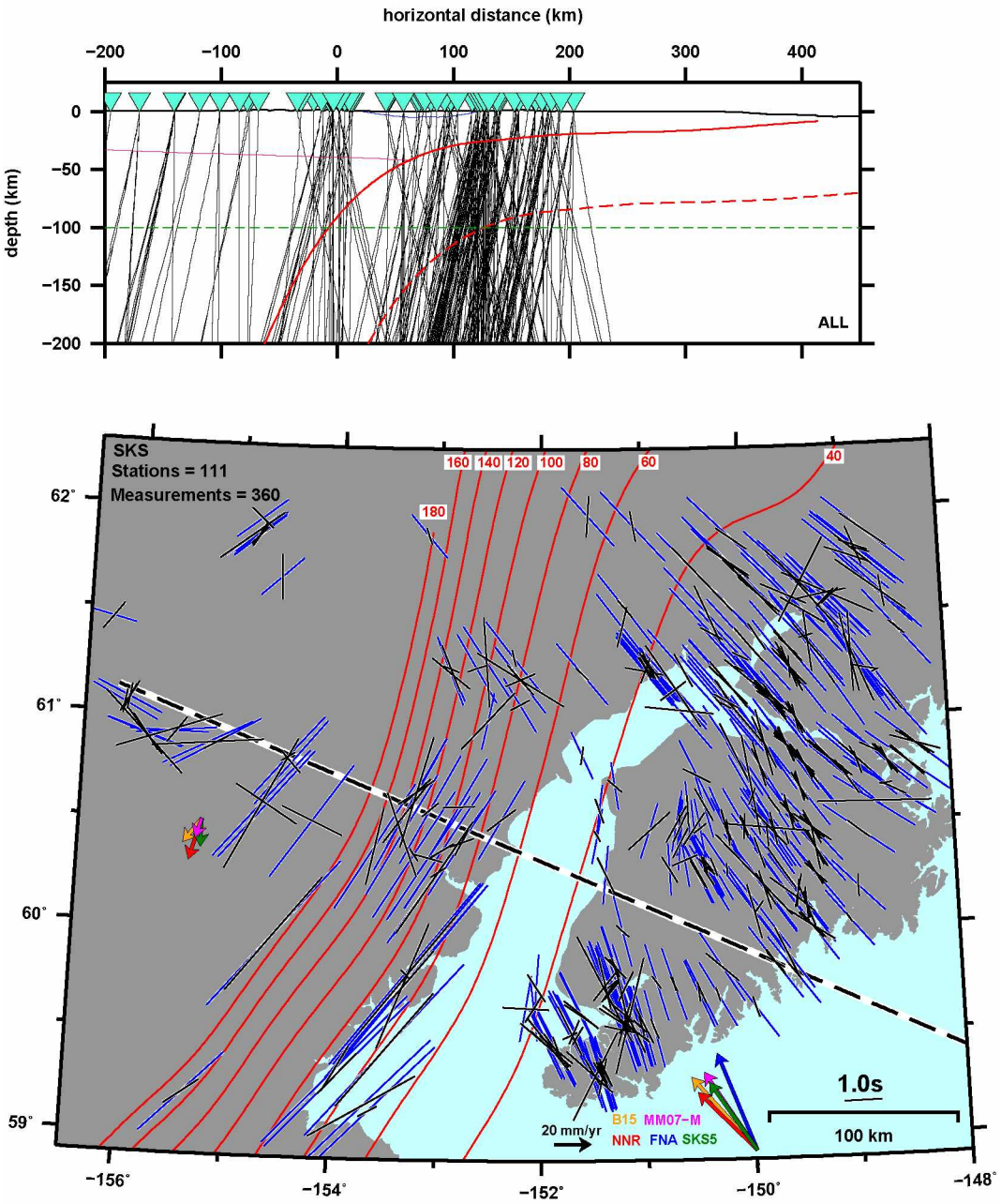

Figure 2.23: Spatially averaged SKS splitting measurements in blue and data in black. The measurements are projected to 100 km depth and the smoothing is strong.

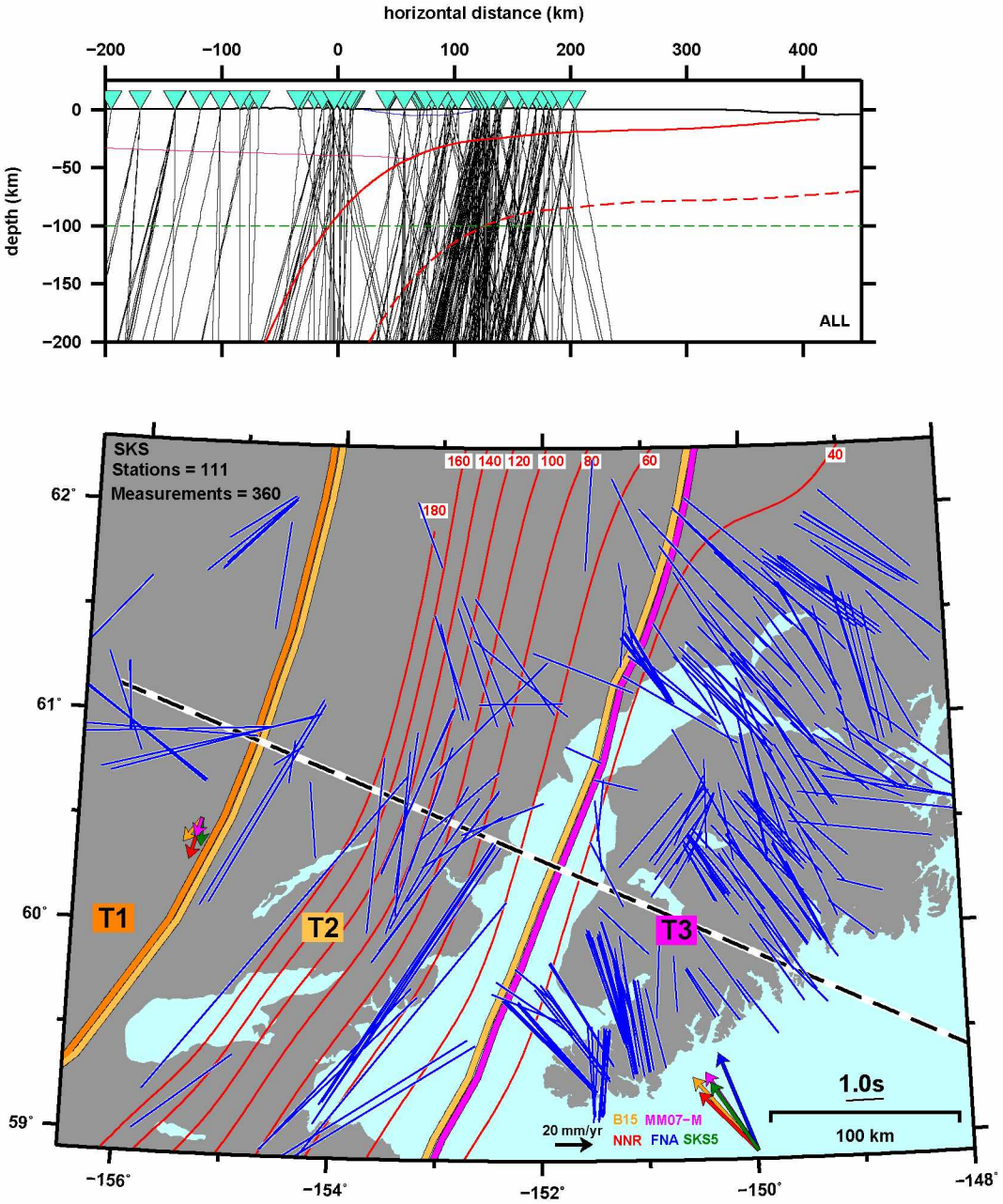

Figure 2.24: Spatially averaged SKS splitting measurements with interpreted splitting regions defined.

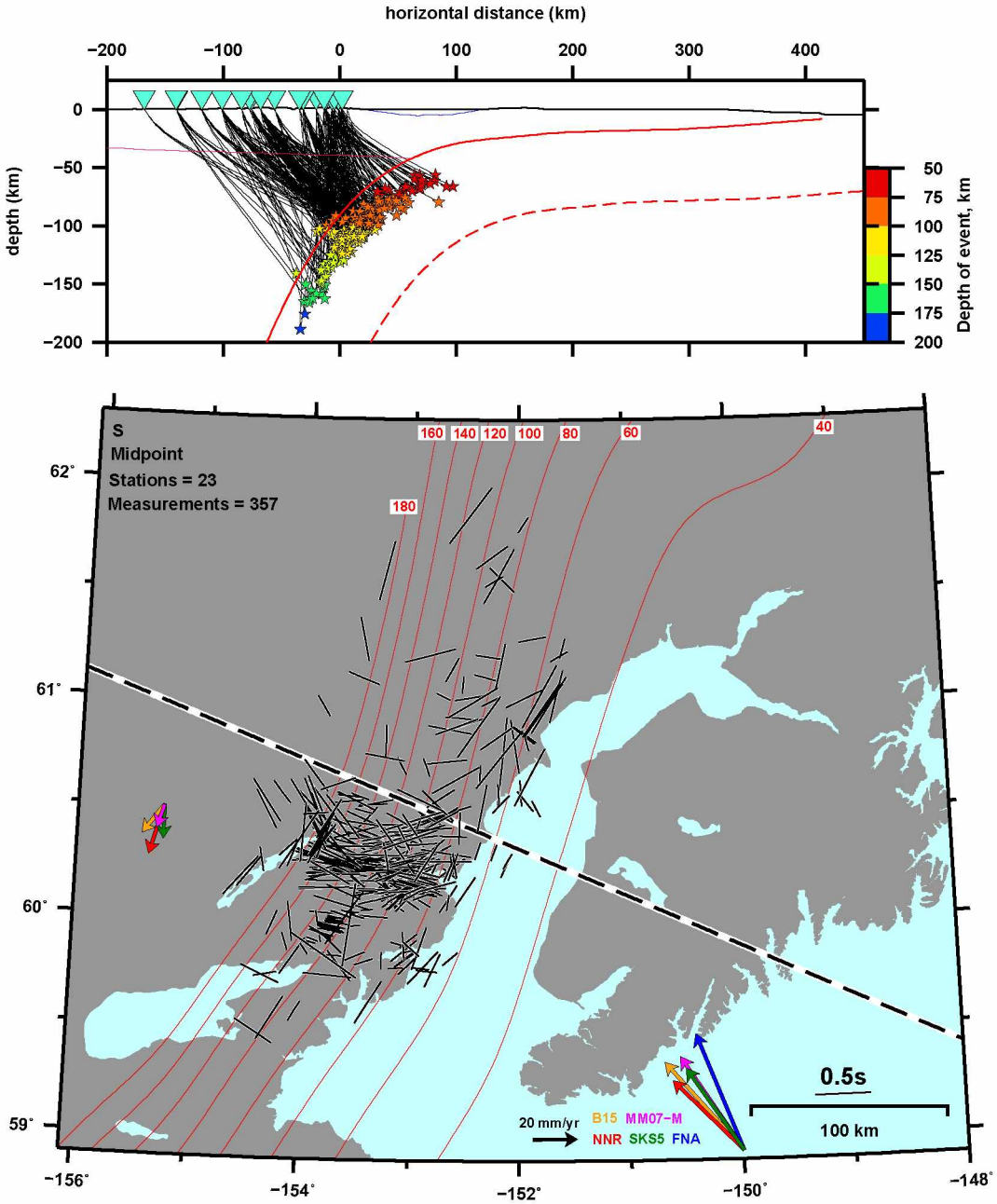

Figure 2.25: Midpoint projection for all stations with ≥ 50 km of underlying mantle. Note the trench-perpendicular fast directions for ray paths in the wedge and convergence parallel measurements in the furthest west backarc.

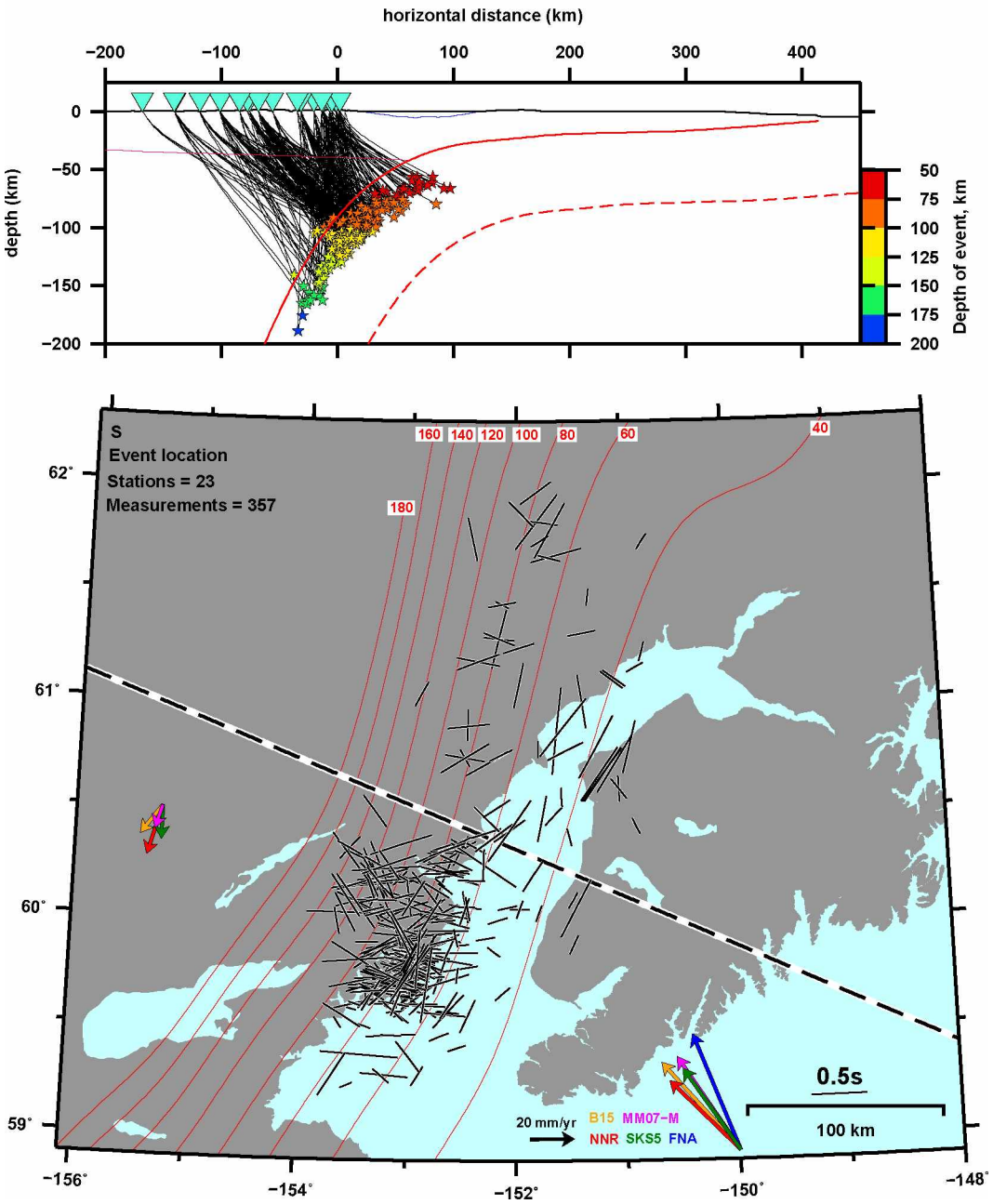

Figure 2.26: Event location projection for all stations with ≥ 50 km of underlying mantle. Note the trench-parallel fast directions east of the 60 km subduction interface contour with ray paths in the mantle nose.

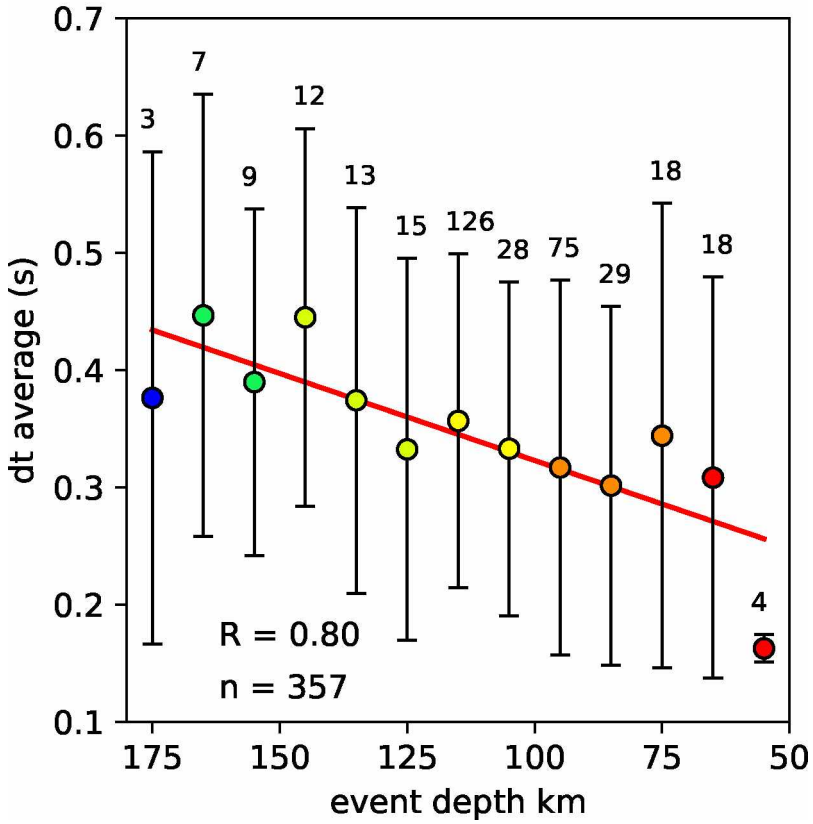

Figure 2.27: Depth vs dt for stations with at least ~50 km of wedge beneath them. Depths are binned in 10 km bins and an average for each bin is taken. The average δt is plotted for each bin along with error bars showing the standard deviation. All measurements and the depth color scale used in this plot are shown in Figure 2.26 and Figure 2.25. The correlation between depth and δt suggests that the mantle wedge is anisotropic.

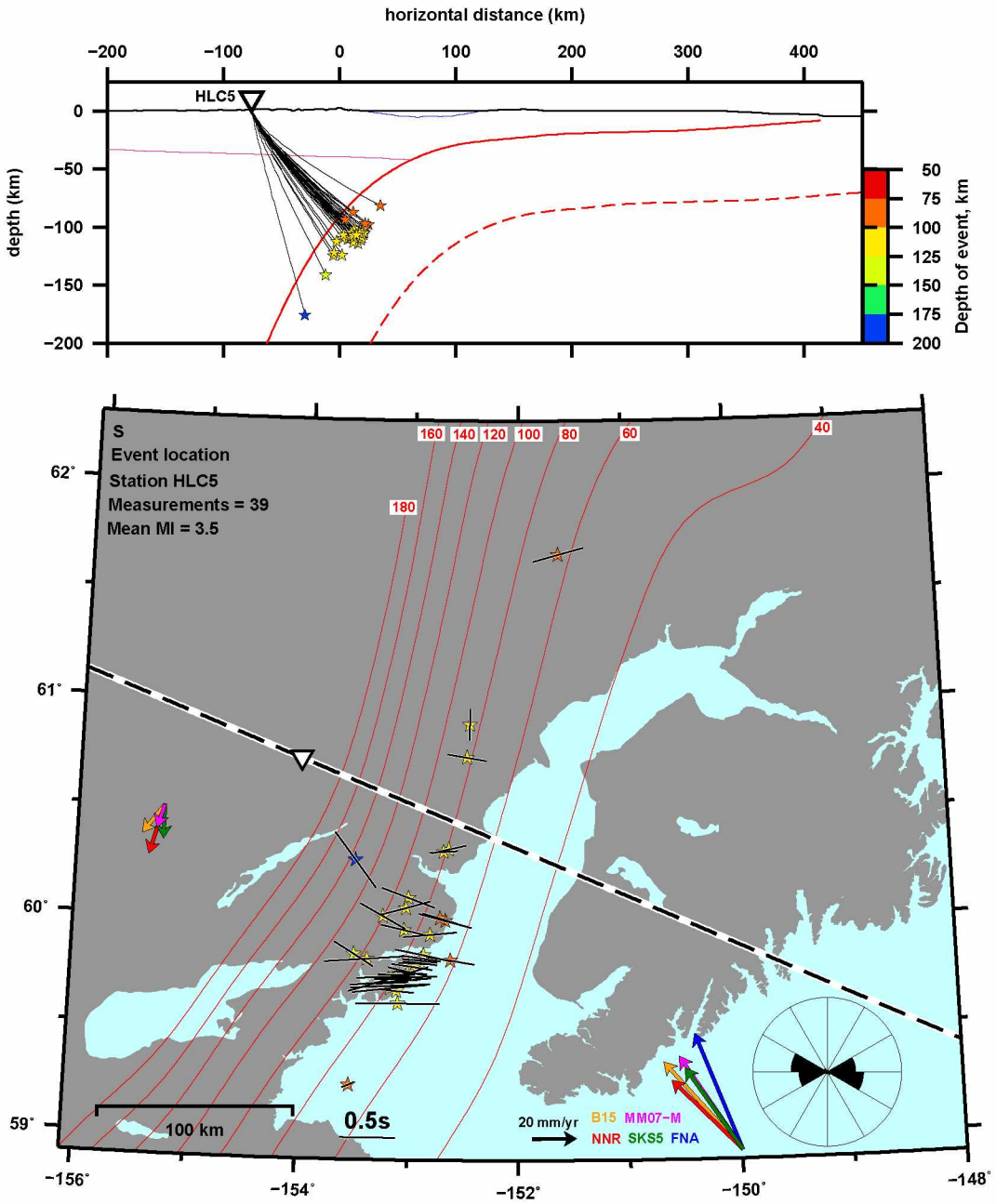

Figure 2.28: Event location projection for station ZE.HLC5 displays a trench-perpendicular splitting pattern and a single plate convergence parallel measurement for the 175 km deep event. Rose diagram displaying fast directions is shown in the bottom right corner.

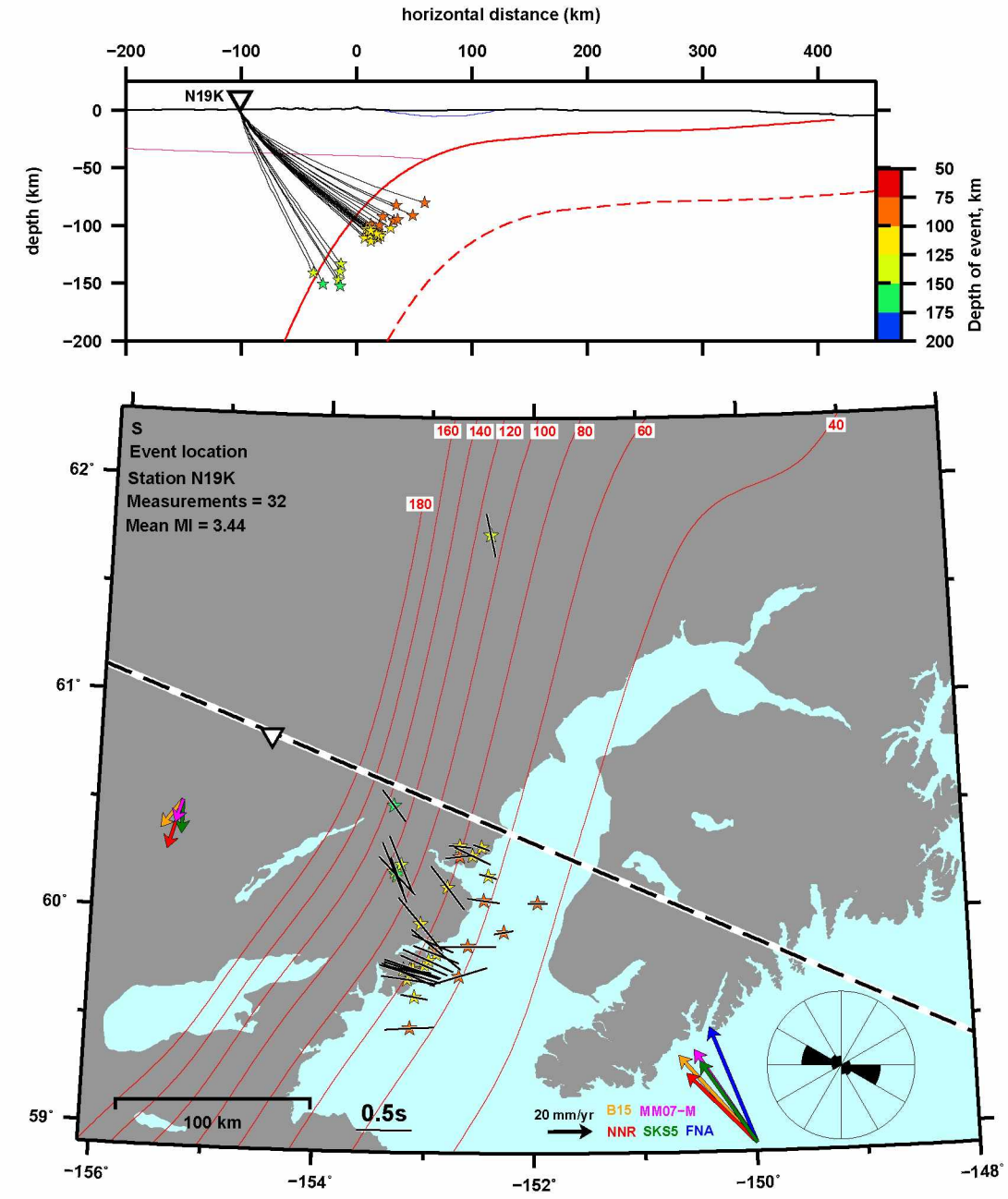

Figure 2.29: Event location projection for station TA.N19K displays a trench-perpendicular splitting pattern with convergence parallel measurements for the deepest events.

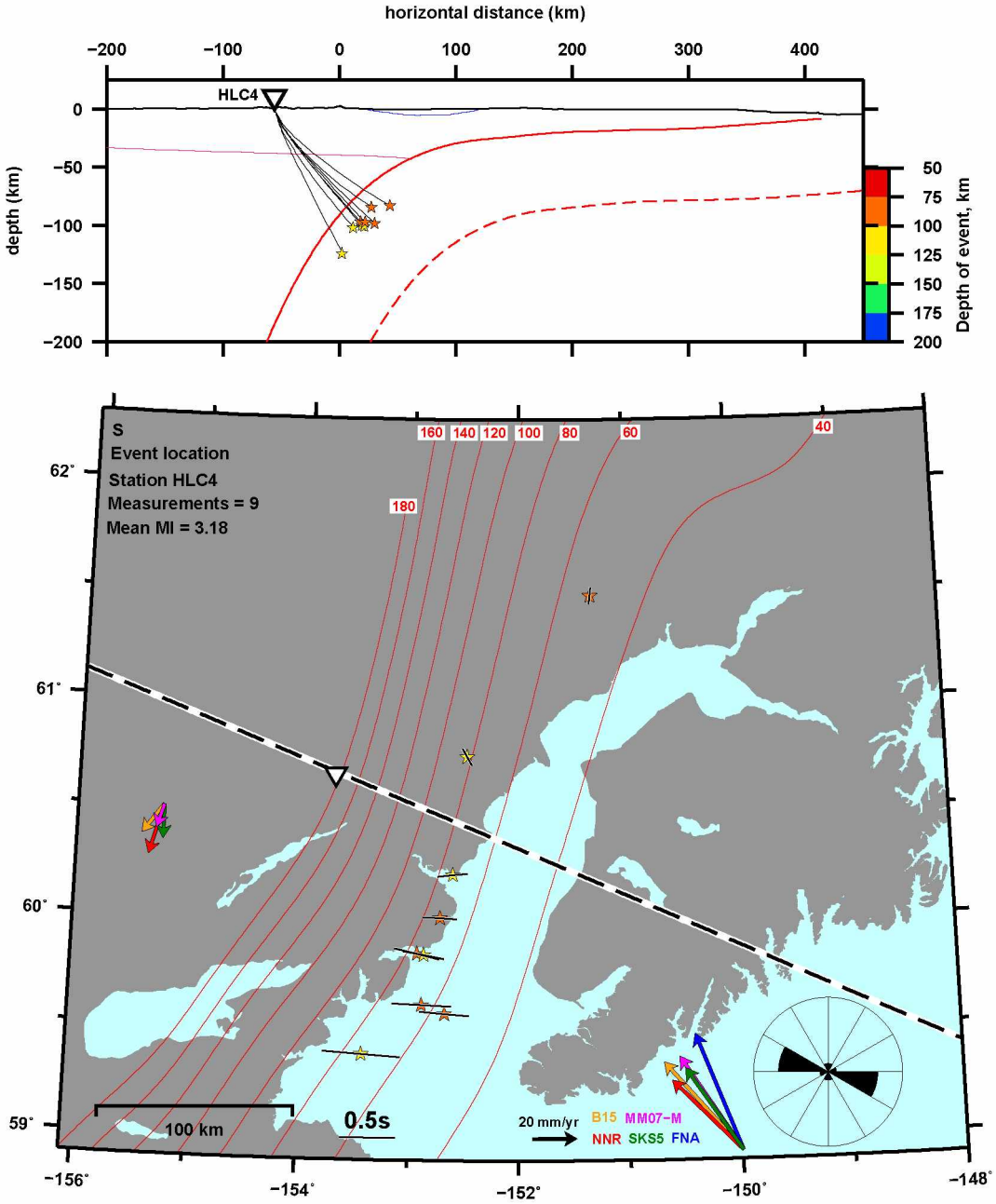

Figure 2.30: Event location projection for station ZE.HLC4 displays a trench-perpendicular splitting pattern.

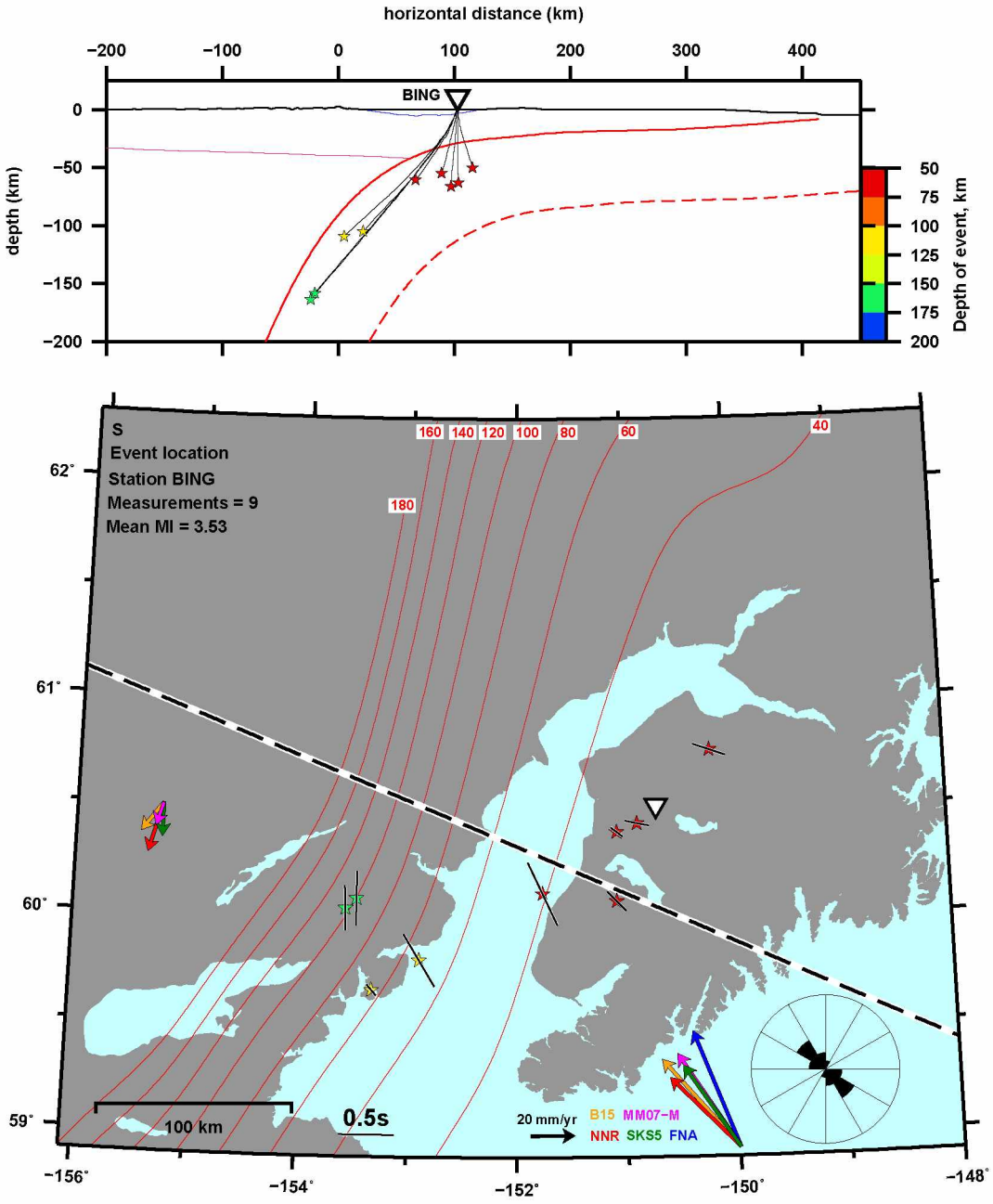

Figure 2.31: Event location projection for station ZE.BING displays a plate-convergence splitting pattern and has ray paths that sample the subducting slab and overriding plate.

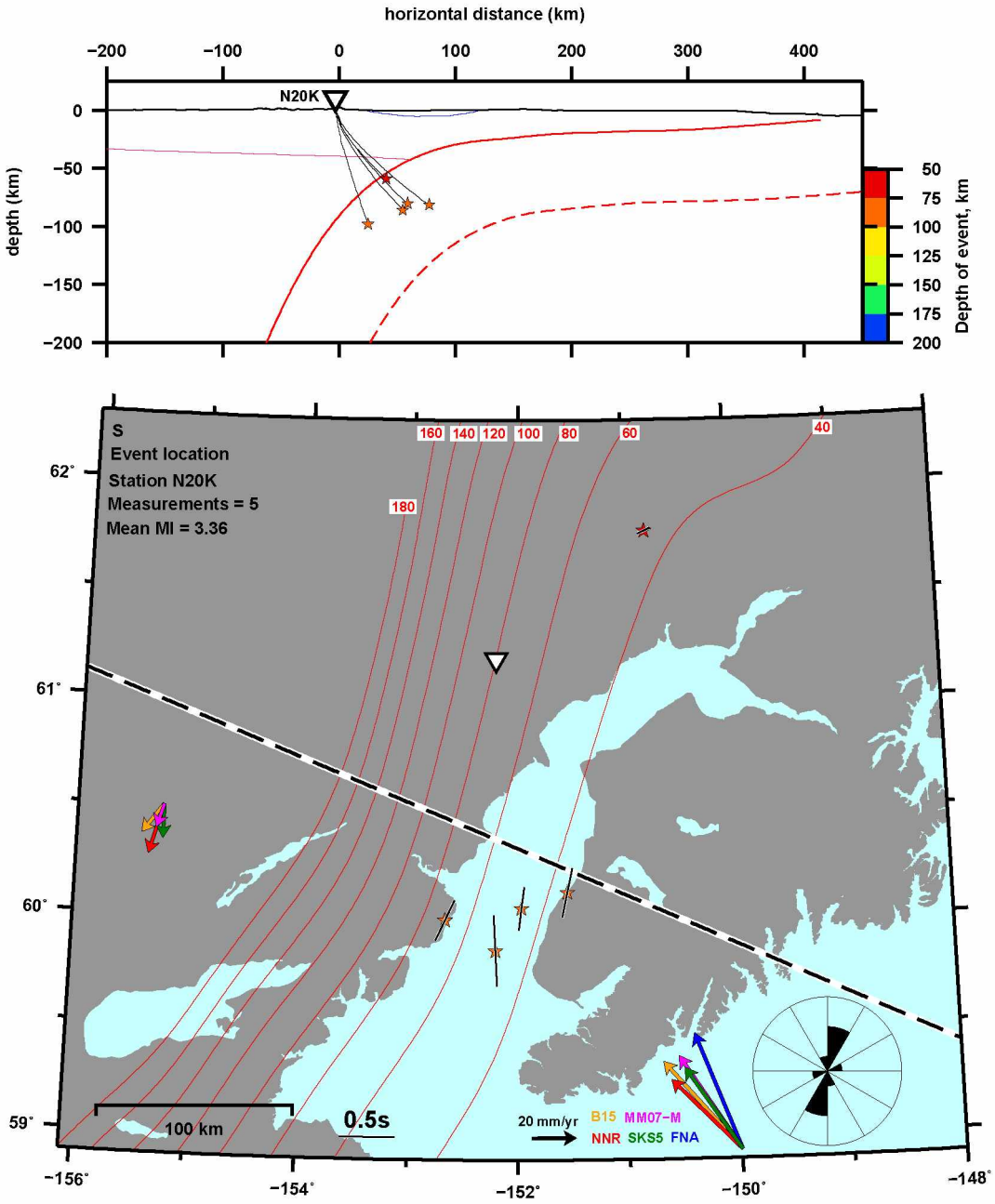

Figure 2.32: Event location projection for station TA.N20K displays a trench-parallel pattern and has ray paths that sample the mantle nose.

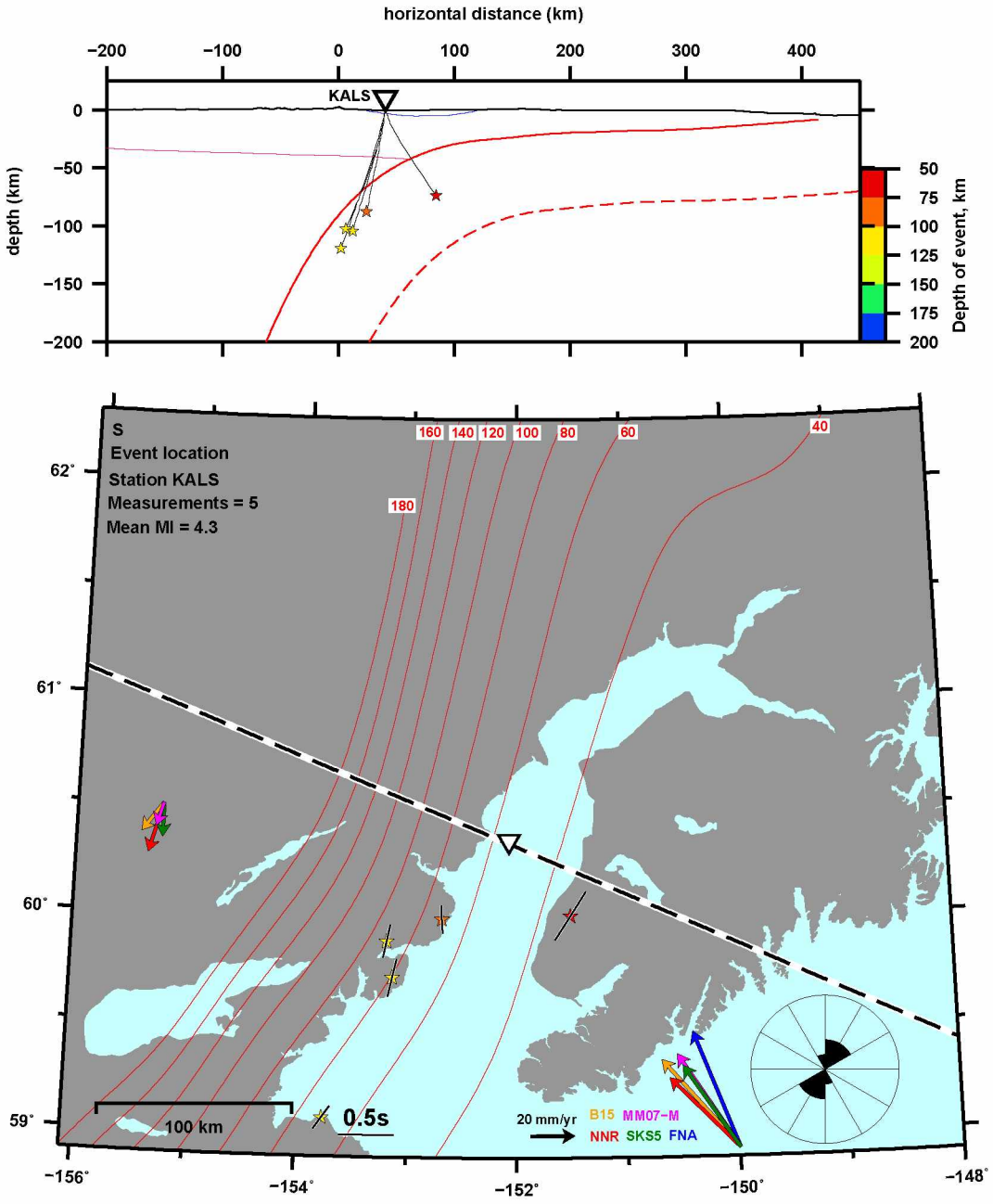

Figure 2.33: Event location projection for station ZE.KALS displays a trench-parallel pattern and has ray paths that sample the mantle nose.

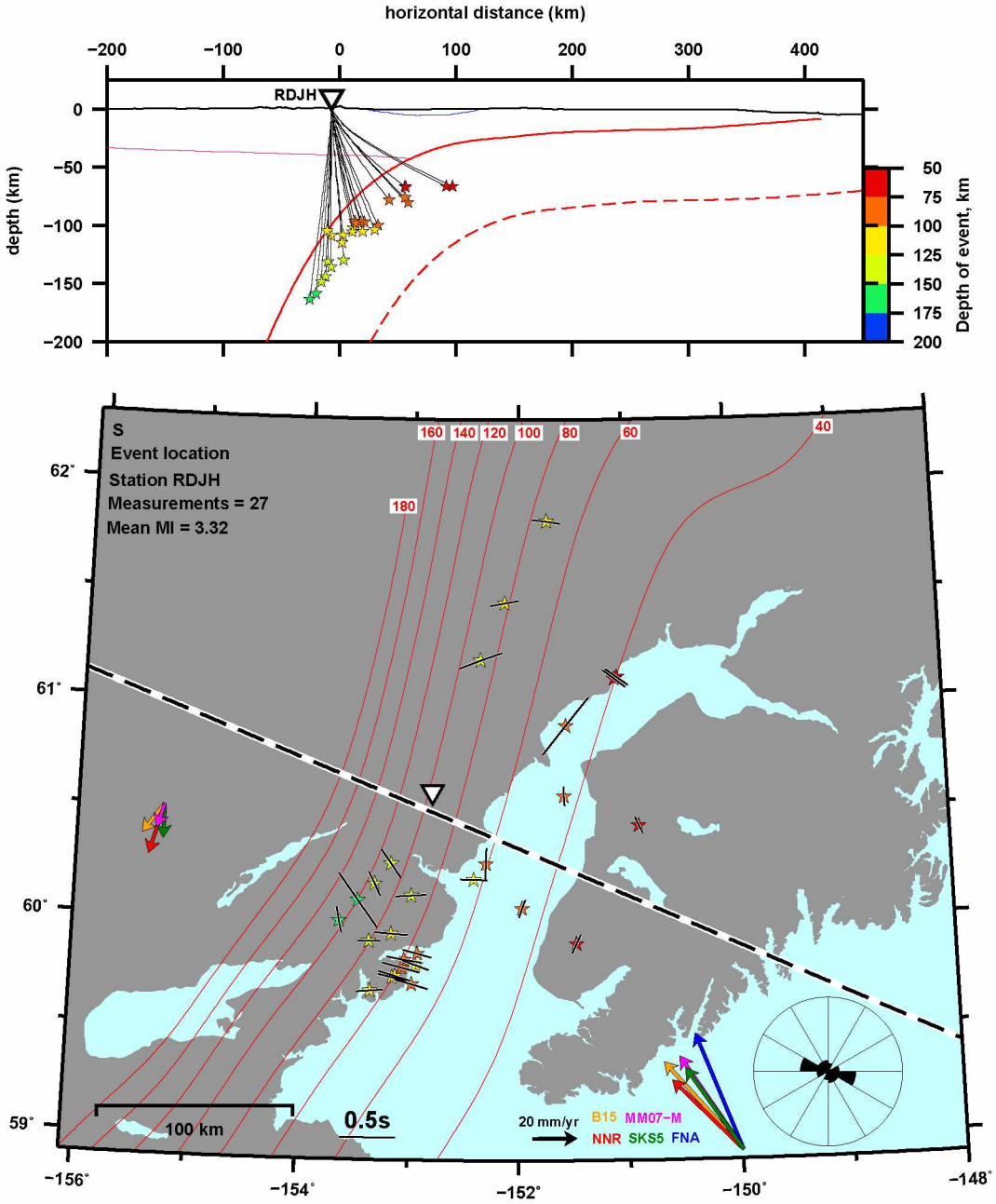

Figure 2.34: Event location projection for station AV.RDJH displays coherent patterns from each splitting region (L1b,L1a,L2,L3).

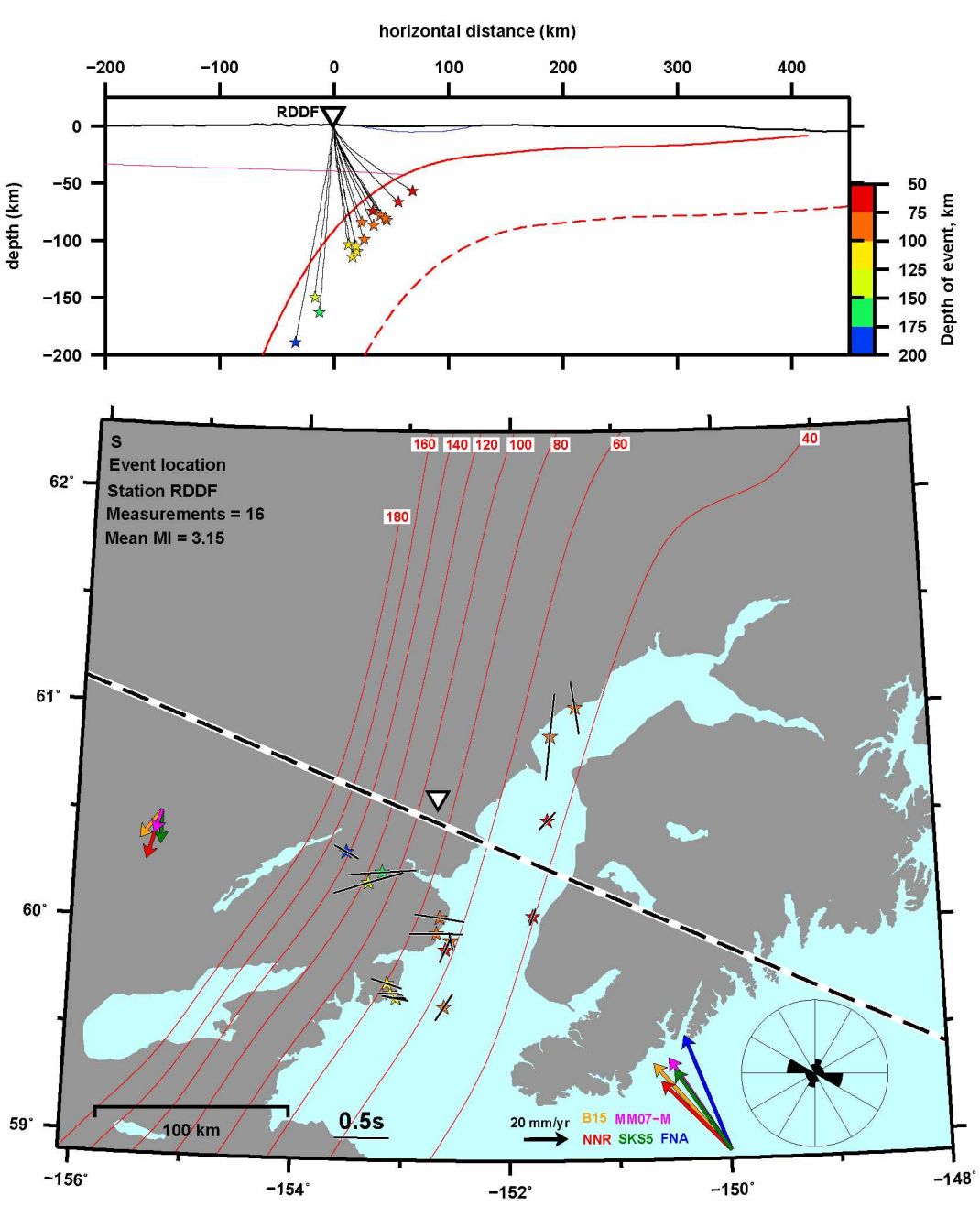

Figure 2.35: Event location projection for station AV.RDDF displays coherent patterns from splittings regions L1a and L2.

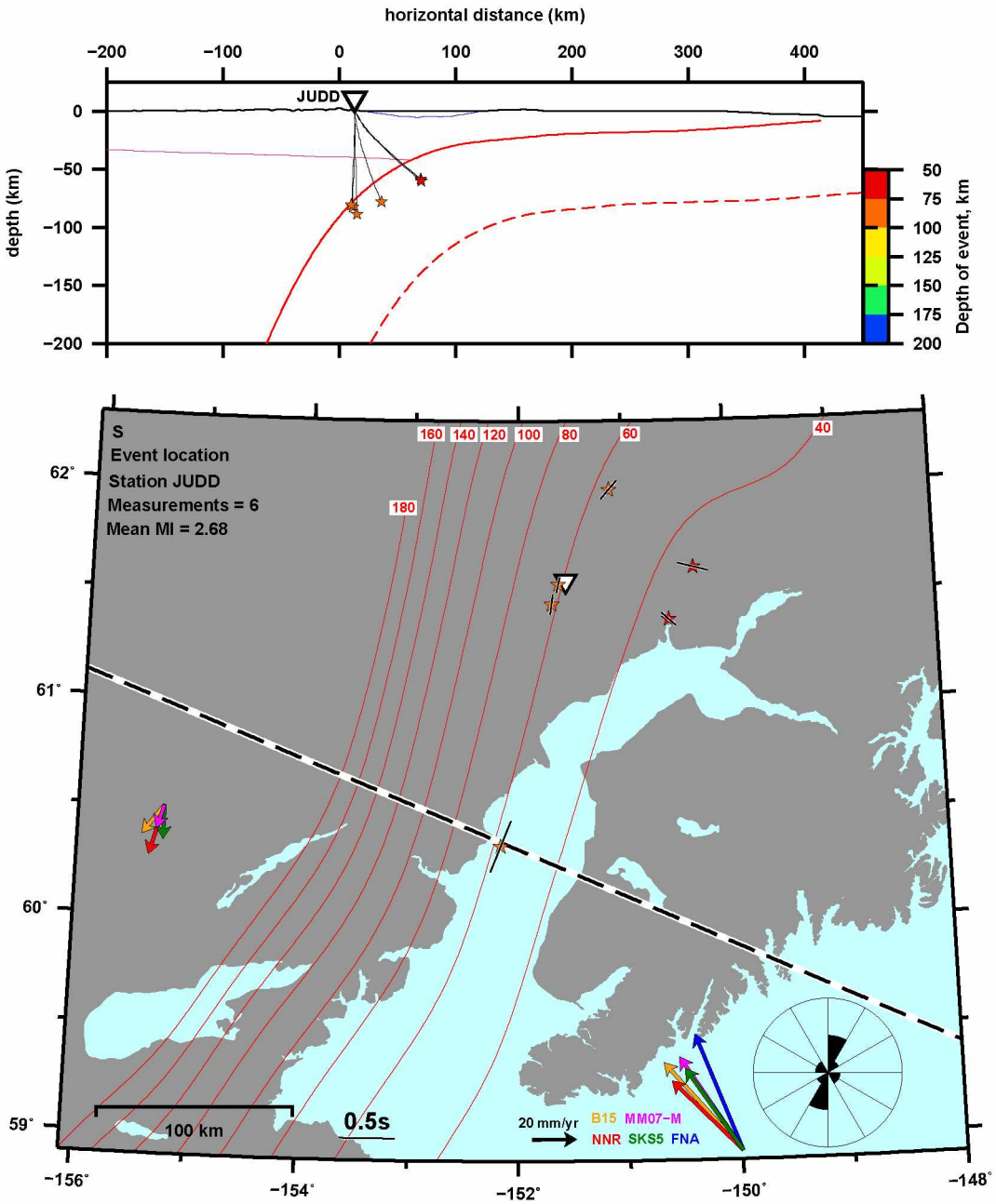

Figure 2.36: Event location projection for station ZE.JUDD displays trench-parallel splitting for paths in the mantle nose and northwest-south east splitting for paths in the subducting slab and overriding plate. Note that this sharp transition has been shown in SKS splitting studies.

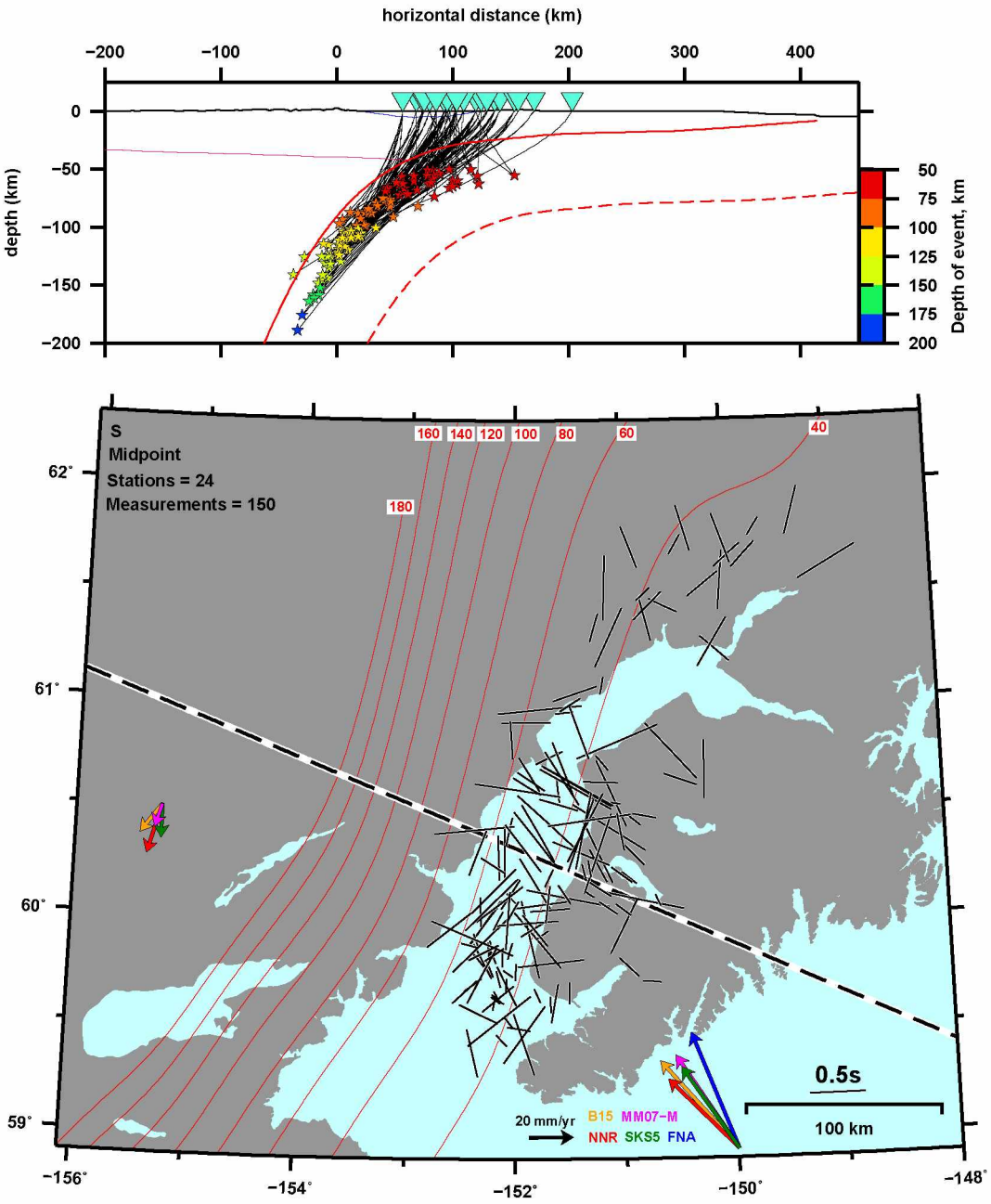

Figure 2.37: Midpoint projection for events to all stations that have most of their ray paths in the slab. While there seems to be some coherence in the north, the splitting pattern is complex. However, we observe large delay times for many of the measurements, indicating that the slab is anisotropic.

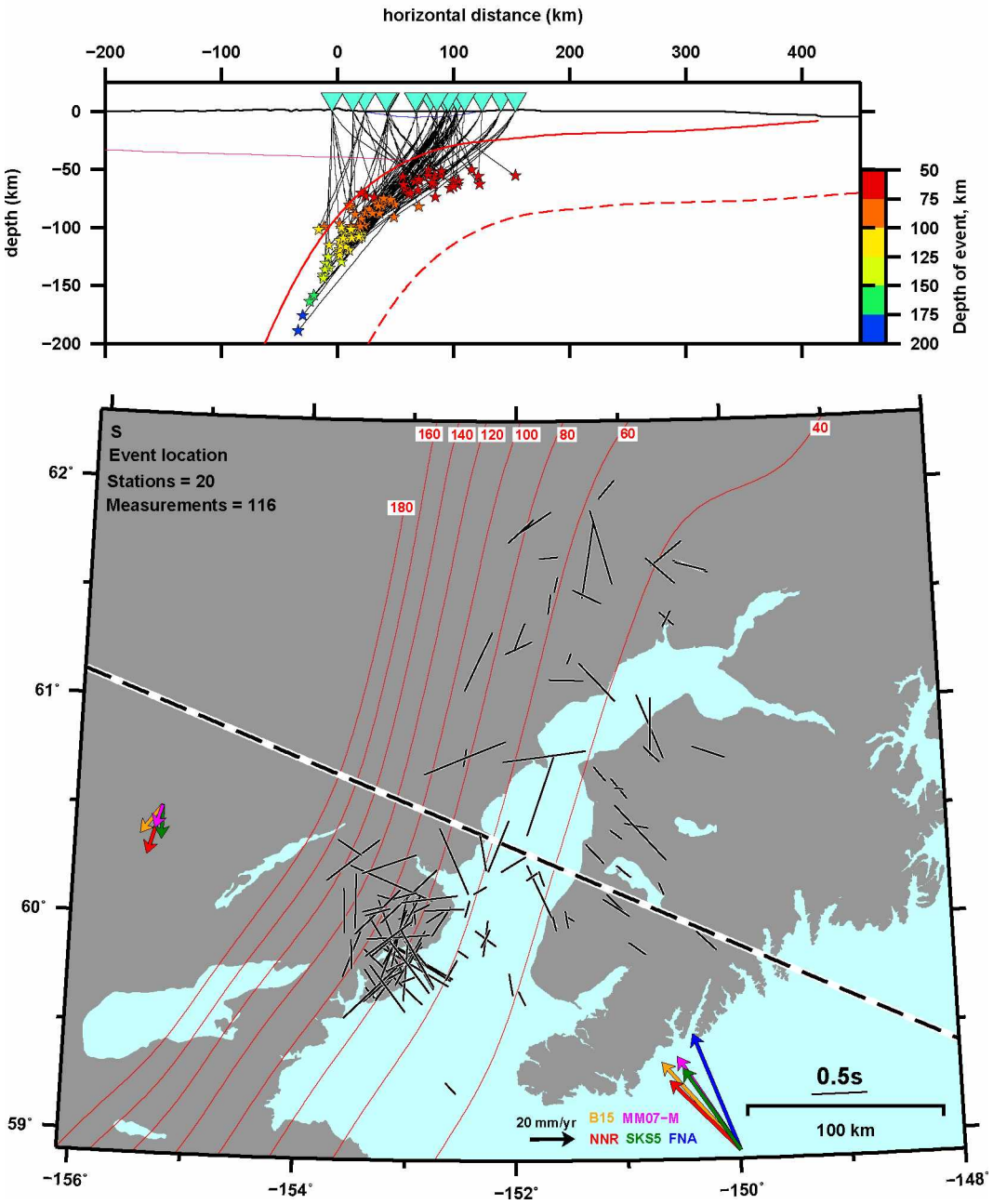

Figure 2.38: Event location projection for stations that have events originating under the Kenai Peninsula. Note the consistent northwest-southeast splitting pattern for the Kenai Peninsula. This patterns matches well with SKS splitting from this study and previous studies.

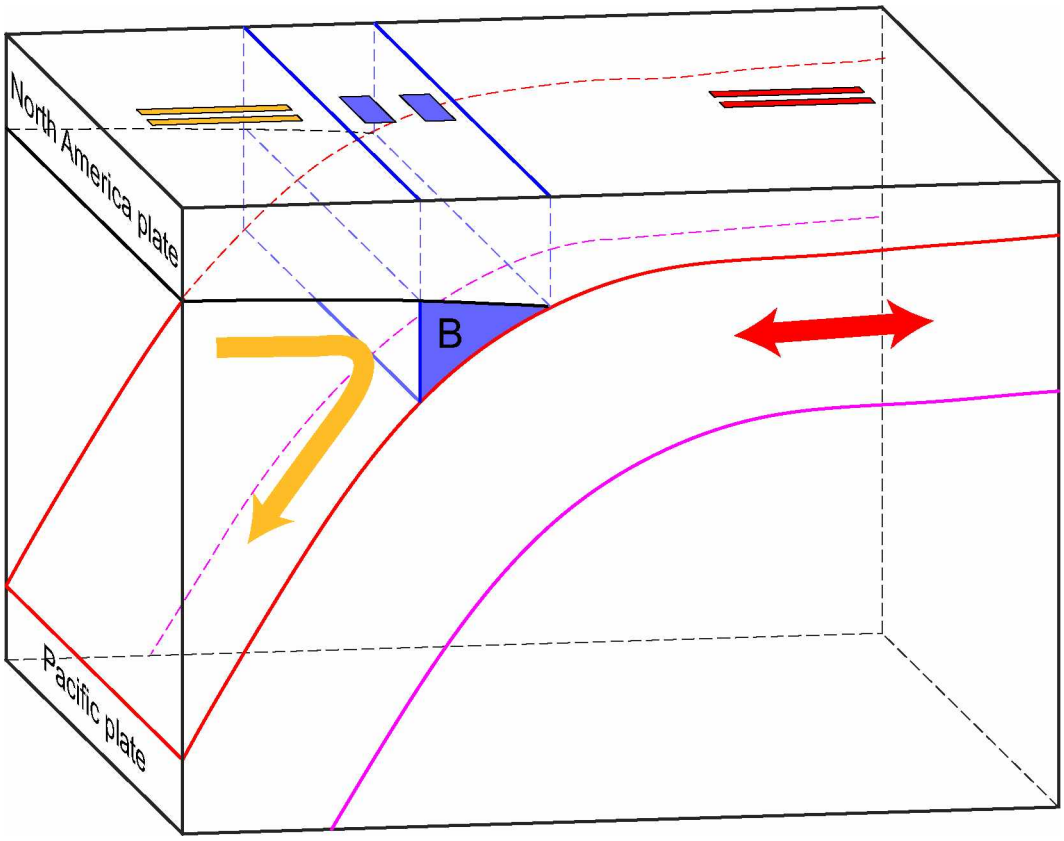

Figure 2.39: 3D Cartoon of the Cook Inlet subduction segment that depicts the observed local splitting patterns and interpreted anisotropic structures. The red arrows represent anisotropy in the subducting Pacific lithosphere. The overlying red bars represent local splitting observations that correspond to the red arrows and thus anisotropy in the slab lithosphere. The backarc shows 2D corner flow (orange curved arrow) with B-type olivine in the mantle nose (blue triangle) and the overlying orange and blue bars are observed splitting patterns that correspond to anisotropy in their underlying and same colored regions. The 2D transect shown in Figure 2.1 and Figure 2.6 was used to interpolate to 3D from a cross-section. The continental Moho is from Miller & Moresi (2018); the top of Pacific plate is from slab 2.0 (Hayes et al., 2018). The bottom of the mantle nose ("B") is drawn at the 80 km depth of the Pacific plate.

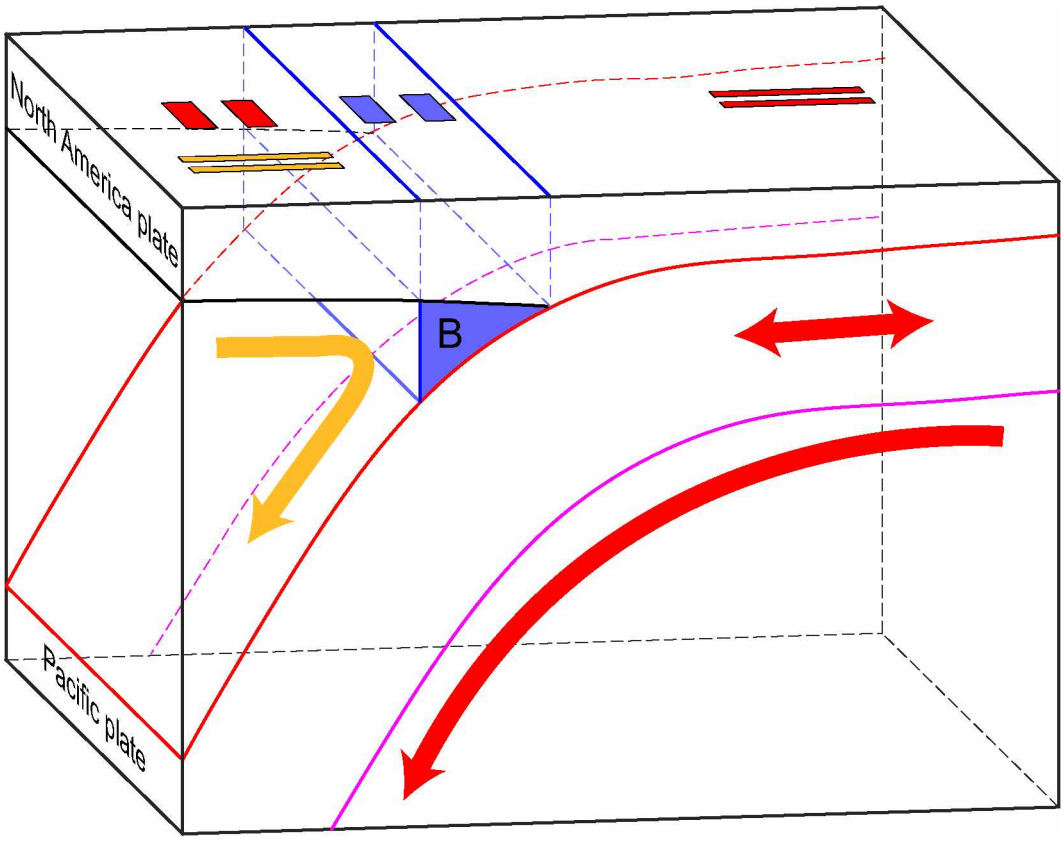

Figure 2.40: Our overall favored model to explain both the local S and SKS splitting patterns. The red arrows represent anisotropy in the slab lithosphere and subslab asthenospheric flow. The overlying red bars (right) represent both local and SKS splitting observations that correspond to the red arrows and thus anisotropy in the slab lithosphere and subslab asthenosphere. The backarc shows 2D corner flow (orange curved arrow) with B-type olivine in the mantle nose (blue triangle) and the overlying orange and blue bars are observed local splitting patterns that correspond to anisotropy in their underlying and same colored regions. The red bars (left) in the backarc are SKS splitting measurements that correspond to the subslab asthenospheric flow and not to the mantle wedge. Note that the 90° change in observed SKS splitting is due to the change in dip of the subslab asthenospheric anisotropy (Song & Kawakatsu, 2013). The 2D transect shown in Figure 2.1 and Figure 2.6 was used to interpolate to 3D from a cross-section. The continental Moho is from Miller & Moresi (2018); the top of Pacific plate is from slab 2.0 (Hayes et al., 2018). The bottom of the mantle nose ("B") is drawn at the 80 km depth of the Pacific plate.

2.8 Tables

Table 2.1: 1D structural model scak used for calculating incidence angles, SKS arrivals, and ray tracing. For all depths below 66 km the model is identical to ak135.

top of layer, km	bottom of layer, km	thickness km	V_S m/s	V_P m/s	density kg/m^3	Q_S	Q_P
0	4	4	3010	5300	2520	300	600
4	9	5	3180	5600	2610	300	600
9	14	5	3520	6200	2780	300	600
14	19	5	3920	6900	2970	300	600
19	24	5	4200	7400	3120	300	600
24	33	9	4370	7700	3200	300	600
33	49	16	4490	7900	3260	300	600
49	66	17	4600	8100	3320	300	600
66	–	–	4720	8300	3370	300	600

2.9 References

Abt, D. L., Fischer, K. M., Abers, G. A., Strauch, W., Protti, J. M., & González, V., 2009. Shear wave anisotropy beneath Nicaragua and Costa Rica: Implications for flow in the mantle wedge, *Geochem. Geophy. Geosyst.*, **10**(5), Q05S15, doi: 10.1029/2009GC002375.

Argus, D. F., Gordon, R. G., & DeMets, C., 2011. Geologically current motion of 56 plates relative to the no-net-rotation reference frame, *Geochem. Geophy. Geosyst.*, **12**, Q11001, doi: 10.1029/2011GC003751.

Bamford, D. & Crampin, S., 1977. Seismic anisotropy – the state of the art, *Geophysical Journal International*, **49**(1), 1–8, doi: 10.1111/j.1365-246X.1977.tb03697.x.

Becker, T. W., Schaeffer, A. J., Lebedev, S., & Conrad, C. P., 2015. Toward a generalized plate motion reference frame, *Geophys. Res. Lett.*, **42**, 3188–3196, doi: 10.1002/2015GL063695.

Chen, K., Tseng, Y.-L., Furumura, T., & Kennett, B., 2015. Anisotropy in the subducting slab: Observations from philippine sea plate events in taiwan, *Geophysical Research Letters*, **42**, 10248–10255, doi: 10.1002/2015GL066227.

Christensen, D. H. & Abers, G. A., 2010. Seismic anisotropy under central Alaska from SKS splitting observations, *J. Geophys. Res.*, **115**, B04315, doi: 10.1029/2009JB006712.

Christensen, D. H., Abers, G. A., & McKnight, T. L., 2003. Mantle anisotropy beneath the Alaska range inferred from *S*-wave splitting observations: Results from BEAAR, in *Eos Trans. Am. Geophys. Un.*, vol. 84(46), Abstract S31C-0782.

Crampin, S. & Peacock, S., 2008. A review of the current understanding of seismic shear-wave splitting in the Earth's crust and common fallacies in interpretation, *Wave Motion*, **45**, 675–722.

Crampin, S., Chesnokov, E. M., & Hipkin, R. G., 1984. Seismic anisotropy — the state of the art: II, *Geophysical Journal International*, **76**(1), 1–16, doi: 10.1111/j.1365-246X.1984.tb05017.x.

Crotwell, H. P., Owens, T. J., & Ritsema, J., 1999. The TauP Toolkit: Flexible Seismic travel-time and ray-path utilities, *Seismol. Res. Lett.*, **70**(2), 154–160.

Doubrovine, P. V., Steinberger, B., & Torsvik, T. H., 2012. Absolute plate motions in a reference frame defined by moving hot spots in the Pacific, Atlantic, and Indian oceans, *J. Geophys. Res.*, **117**, B09101, doi: 10.1029/2011JB009072.

Eberhart-Phillips, D., Christensen, D. H., Brocher, T. M., Hansen, R., Ruppert, N. A., Haeussler, P. J., & Abers, G. A., 2006. Imaging the transition from Aleutian subduction to Yakutat collision in central Alaska, with local earthquakes and active source data, *J. Geophys. Res.*, **111**, B11303, doi: 10.1029/2005JB004240.

Favier, N. & Chevrot, S., 2003. Sensitivity kernels for shear wave splitting in transverse isotropic media, *Geophys. J. Int.*, **153**, 312–228, doi: 10.1046/j.1365-246X.2003.01894.x.

Fouch, M. & Rondenay, S., 2006. Seismic anisotropy beneath stable continental interiors, *Physics of the Earth and Planetary Interiors*, **158**, 292–320, doi: 10.1016/j.pepi.2006.03.024.

Freymueller, J. T., Woodard, H., Cohen, S. C., Cross, R., Elliott, J., Larsen, C. F., Hreinsdóttir, S., & Zweck, C., 2008. Active deformation processes in Alaska, based on 15 years of GPS measurements, in *Active Tectonics and Seismic Potential of Alaska*, vol. 179 of **Geophysical Monograph**, pp. 1–42, eds Freymueller, J. T., Haeussler, P. J., Wesson, R., & Ekström, G., Am. Geophys. Un., Washington, D.C.

Fu, Y. & Freymueller, J. T., 2013. Repeated large Slow Slip Events at the south central Alaska subduction zone, *Earth Planet. Sci. Lett.*, **375**, 303–311.

Hacker, B. R. & Abers, G. A., 2012. Subduction Factory 5: Unusually low Poisson's ratios in subduction zones from elastic anisotropy of peridotite, *J. Geophys. Res.*, **117**, B06308, doi: 10.1029/2012JB009187.

Hall, C., Fischer, K., Parmentier, E. M., & Blackman, D., 2000. The influence of plate motions on three-dimensional back arc mantle flow and shear wave, *Journal of Geophysical Research*, **105**, 28009–28034, doi: 10.1029/2000JB900297.

Hammond, J. O. S., Wookey, J., Kaneshima, S., Inoue, H., Yamashina, T., & Harjadi, P., 2010. Systematic variation in anisotropy beneath the mantle wedge in the Java–Sumatra subduction system from shear-wave splitting, *Phys. Earth Planet. Inter.*, **178**, 189–201.

Hanna, J. & Long, M. D., 2012. SKS splitting beneath Alaska: Regional variability and implications for subduction processes at a slab edge, *Tectonophysics*, **530-531**, 272–285.

Hayes, G. P., Moore, G. L., Portner, D. E., Hearne, M., Flamme, H., Furtney, M., & Smoczyk, G. M., 2018. Slab2, a comprehensive subduction zone geomety model, *Science*, doi: 10.1126/science.aat4723.

Jadamec, M. A. & Billen, M. I., 2010. Reconciling surface plate motions with rapid three-dimensional mantle flow around a slab edge, *Nature*, **465**, 338–342, doi: 10.1038/nature09053.

Karato, S., Jung, H., Katayama, I., & Skemer, P., 2008. Geodynamic significance of seismic anisotropy of the upper mantle: New insights from laboratory studies, *Annu. Rev. Earth Planet. Sci.*, **36**, 59–95.

Kaula, W. M., 1975. Absolute plate motions by boundary velocity minimizations, *J. Geophys. Res.*, **80**(2), 244–248.

Kneller, E., van Keken, P., Karato, S.-i., & Park, J., 2005. B-type olivine fabric in the mantle wedge: Insights from high-resolution non-newtonian subduction zone models, *Earth and Planetary Science Letters*, **237**, 781–797, doi: 10.1016/j.epsl.2005.06.049.

Koehler, R. D., Farrell, R.-E., Burns, P. A. C., & Combellick, R. A., 2012. Quaternary faults and folds in Alaska: A digital database, Alaska Div. Geol. Geophys. Surv. Miscellaneous Publication 141, 31 p., 1 sheet, scale 1:3,700,000.

León Soto, G. & Valenzuela, R. W., 2013. Corner flow in the Isthmus of Tehuantepec, Mexico inferred from anisotropy measurements using local intraslab earthquakes, *Geophysical Journal International*, **195**(2), 1230–1238, doi: 10.1093/gji/ggt291.

Li, S., Freymueller, J., & McCaffrey, R., 2016. Slow slip events and time-dependent variations in locking beneath Lower Cook Inlet of the Alaska-Aleutian subduction zone, *J. Geophys. Res. Solid Earth*, **121**, 1060–1079, doi: 10.1002/2015JB012491.

Lliboutry, L., 1974. Plate movement relative to rigid lower mantle, *Nature*, **250**, 298–300.

Long, M. D. & Silver, P. G., 2008. The subduction zone flow field from seismic anisotropy: A global view, *Science*, **319**, 315–318.

Long, M. D. & van der Hilst, R. D., 2006. Shear wave splitting from local events beneath the ryukyu arc: Trench-parallel anisotropy in the mantle wedge.

Long, M. D. & van der Hilst, R. D., 2006. Shear wave splitting from local events beneath the Ryukyu arc: Trench-parallel anisotropy in the mantle wedge, *Phys. Earth Planet. Inter.*, **155**, 300–312.

Long, M. D. & Wirth, E. A., 2013. Mantle flow in subduction systems: The mantle wedge flow field and implications for wedge processes, *J. Geophys. Res. Solid Earth*, **118**, 583–606, doi: 10.1002/jgrb.50063.

Long, M. D., de Hoop, M. V., & van der Hilst, R. D., 2008. Wave-equation shear wave splitting tomography, *Geophys. J. Int.*, **172**, 311–330.

Marson-Pidgeon, K. & Savage, M. K., 1997. Frequency-dependent anisotropy in Wellington, New Zealand, *Geophys. Res. Lett.*, **24**(24), 3297–3300.

McPherson, A., Christensen, D. H., Abers, G. A., Tape, C., & Moore-Driskell, M. M., 2017. Shear Wave Splitting and Mantle Flow in Alaska, in *AGU Fall Meeting Abstracts*, vol. 2017, pp. DI43B–0365.

McPherson, A. M., Christensen, D. H., Abers, G. A., & Tape, C., 2020. Shear wave splitting and mantle flow beneath Alaska, *J. Geophys. Res. Solid Earth*, **123**, doi: 10.1029/2019JB018329.

Mehl, L., Hacker, B. R., Hirth, G., & Kelemen, P. B., 2003. Arc-parallel flow within the mantle wedge: Evidence from the accreted Talkeetna arc, south central Alaska, *J. Geophys. Res.*, **108**(B8), 2375, doi: 10.1029/2002JB002233.

Miller, M. S. & Moresi, L., 2018. Mapping the Alaska Moho, *Seismol. Res. Lett.*, **89**(6), 2430–2436, doi: 10.1785/0220180222.

Minster, J. B. & Jordan, T. H., 1978. Present-day plate motions, *J. Geophys. Res.*, **83**(B11), 5331–5354.

Morgan, W. J. & Morgan, J. P., 2007. Plate velocities in the hotspot reference frame, in *Plates, plumes, and planetary processes*, pp. 65–78, eds Foulger, G. R. & Jurdy, D. M., Geol. Soc. Am., Boulder, Colo., USA, Special Paper 430.

Nakajima, J. & Hasegawa, A., 2004. Shear-wave polarization anisotropy and subduction-induced flow in the mantle wedge of northeastern Japan, *Earth Planet. Sci. Lett.*, **225**, 365–377.

Naugler, F. P. & Wageman, J. M., 1973. Gulf of Alaska: Magnetic Anomalies, Fracture Zones, and Plate Interaction, *GSA Bulletin*, **84**(5), 1575–1584, doi: 10.1130/0016-7606(1973)84<1575:GOAMAF>2.0.CO;2.

Nuttli, O., 1961. The effect of the earth's surface on the S wave particle motion, *Bulletin of the Seismological Society of America*, **51**(2), 237–246.

Ohta, Y., Freymueller, J. T., Hreinsdóttir, S., & Suito, H., 2006. A large slow slip event and the depth of the seismogenic zone in the south central Alaska subduction zone, *Earth Planet. Sci. Lett.*, **247**, 108–116.

Okaya, D., Christensen, N. I., Ross, Z. E., & Wu, F. T., 2016. Terrane-controlled crustal shear wave splitting in Taiwan, *Geophys. Res. Lett.*, **43**, 556–563, doi: 10.1002/2015GL066446.

Perttu, A., Christensen, D., Abers, G., & Song, X., 2014. Insights into mantle structure and flow beneath Alaska based on a decade of observations of shear wave splitting, *J. Geophys. Res. Solid Earth*, **119**, 8366–8377, doi: 10.1002/2014JB011359.

Richards, C., 2020. Shear-wave splitting observations from local and teleseismic earthquakes recorded in Alaska, ScholarWorks@UA at http://hdl.handle.net/11122/11004 (last accessed April 2020): descriptor file and four sets of figures for S and SKS splitting.

Richards, C., Tape, C., & Ross, Z., 2020. Anisotropy in the alaska subduction zone: shear-wave splitting observations from local and teleseismic earthquakes, *Earth and Planetary Science Letters*.

Ross, Z. E., White, M. C., Vernon, F. L., & Ben-Zion, Y., 2016. An improved algorithm for real-time *S*-wave picking with application to the (augmented) ANZA network in southern California, *Bull. Seismol. Soc. Am.*, **106**(5), 2013–2022, doi: 10.1785/0120150230.

Savage, M. K., 1999. Seismic anisotropy and mantle deformation: What have we learned from shear wave splitting, *Rev. Geophys.*, **37**(1), 65–106.

Savage, M. K., Wessel, A., Teanby, N. A., & Hurst, A. W., 2010. Automatic measurement of shear wave splitting and applications to time varying anisotropy at Mount Ruapehu volcano, New Zealand, *J. Geophys. Res.*, **115**, B12321, doi: 10.1029/2010JB007722.

Schlaphorst, D., Kendall, J.-M., Baptie, B., Latchman, J., & Tait, S., 2017. Gaps, tears and seismic anisotropy around the subducting slabs of the antilles, *Tectonophysics*, **698**, doi: 10.1016/j.tecto.2017.01.002.

Shellenbaum, D. P., Gregersen, L. S., & Delaney, P. R., 2010. Top Mesozoic unconformity depth map of the Cook Inlet Basin, Alaska, Alaska Div. Geol. Geophys. Surv. Report of Investigation 2010-2, 1 sheet, scale 1:500,000, available at http://www.dggs.alaska.gov/pubs/id/21961 (last accessed 2016-10-30).

Sieminski, A., Paulssen, H., Trampert, J., & Tromp, J., 2008. Finite-frequency *SKS* splitting: Measurement and sensitivity kernels, *Bull. Seismol. Soc. Am.*, **98**(4), 1797–1810.

Silver, P. G., 1996. Seismic anisotropy beneath the continents: Probing the depths of geology, *Annual Review of Earth and Planetary Sciences*, **24**(1), 385–432, doi: 10.1146/annurev.earth.24.1.385.

Silver, P. G. & Chan, W. W., 1991. Shear wave splitting and subcontinental mantle deformation, *J. Geophys. Res.*, **96**(B10), 16,429–16,454.

Solomon, S. C. & Sleep, N. H., 1974. Some simple physical models for absolute plate motion, *J. Geophys. Res.*, **79**(17), 2557–2567.

Song, T. A. & Kawakatsu, H., 2012. Subduction of oceanic asthenosphere: Evidence from sub-slab seismic anisotropy, *Geophys. Res. Lett.*, **39**, L17301, doi: 10.1029/2012GL052639.

Song, T.-R. A. & Kawakatsu, H., 2013. Subduction of oceanic asthenosphere: A critical appraisal in central Alaska, *Earth Planet. Sci. Lett.*, **367**, 82–94.

Tape, C., Musé, P., Simons, M., Dong, D., & Webb, F., 2009. Multiscale estimation of GPS velocity fields, *Geophys. J. Int.*, **179**, 945–971, doi: 10.1111/j.1365-246X.2009.04337.x.

Tape, C., Plesch, A., Shaw, J. H., & Gilbert, H., 2012. Estimating a continuous Moho surface for the California Unified Velocity Model, *Seismol. Res. Lett.*, **83**(4), 728–735.

Teanby, N. A., Kendall, J.-M., & van der Baan, M., 2004. Automation of shear-wave splitting measurements using cluster analysis, *Bull. Seismol. Soc. Am.*, **94**(2), 453–463, doi: 10.1785/0120030123.

van Keken, P. E., 2003. The structure and dynamics of the mantle wedge, *Earth and Planetary Science Letters*, **215**(3), 323 – 338, doi: https://doi.org/10.1016/S0012-821X(03)00460-6.

Venereau, C., Martin-Short, R., Bastow, I., Allen, R., & Kounoudis, R., 2019. The role of variable slab dip in driving mantle flow at the eastern edge of the alaskan subduction margin: insights from sks shear-wave splitting, *Geochemistry, Geophysics, Geosystems*, doi: 10.1029/2018GC008170.

Wei, M., McGuire, J. J., & Richardson, E., 2012. A slow slip event in the south central Alaska Subduction Zone and related seismicity anomaly, *Geophys. Res. Lett.*, **39**, L15309, doi: 10.1029/2012GL052351.

Wessel, A., 2010. Automatic shear wave splitting measurements at mt. ruapehu volcano, new zealand.

Wiemer, S., Tytgat, G., Wyss, M., & Duenkel, U., 1999. Evidence for shear-wave anisotropy in the mantle wedge beneath south central Alaska, *Bull. Seismol. Soc. Am.*, **89**(5), 1313–1322.

Wirth, E. & Long, M. D., 2010. Frequency-dependent shear wave splitting beneath the Japan and Izu-Bonin subduction zones, *Phys. Earth Planet. Inter.*, **181**, 141–154, doi: 10.1016/j.pepi.2010.05.006.

Yang, X., Fischer, K., & Abers, G., 1995. Seismic anisotropy beneath shumagin island segment of the aleutian-alaska subduction zone, *Journal of Geophysical Research*, **100**, doi: 10.1029/95JB01425.

Chapter 3
General Conclusion

We have performed shear-wave splitting analyses in the Cook Inlet region of the Alaska subduction zone for both local S waves from intraslab earthquakes and teleseismic SKS waves. This constitutes the first comprehensive local splitting study in Alaska comprised of a large collection of seismic networks, including SALMON, MOOS, TA, AVO, and permanent stations. This study greatly improves the data coverage for local splitting in Alaska and helps elucidate the competing interpretations regarding mantle flow and anisotropy in the Alaska subduction zone.
The new constraints and clarifications brought forth by this study include:

- 2D corner flow in the anisotropic mantle wedge interpreted from strongly coherent trench-perpendicular local splitting fast directions in the backarc. This refutes and is orthogonal to the direction of flow that has been suggested by the previous SKS studies.
- B-type olivine in the nose suggested by the sharp transition to trench-parallel splitting fast directions in the forearc.
- The subducting lithosphere is significantly anisotropic and deserves to be considered in interpreted anisotropic subduction zone models.
- The subducting slab's structure and motion appear to be the dominant influence on anisotropy and mantle flow regimes.

The dominantly trench-parallel backarc splitting fast directions in the SKS datasets are well explained by the predictions of Song & Kawakatsu (2012, 2013) invoking subslab asthenospheric flow rather than trench-parallel mantle wedge flow (Christensen & Abers, 2010; Perttu et al., 2014; McPherson et al., 2017; Venereau et al., 2019; Hanna & Long, 2012). While there are some trench-perpendicular SKS fast directions for measurements with ray paths in the wedge, overall the SKS datasets do not display the same dominant trench-perpendicular splitting pattern as seen in the local S dataset. The differences in the two phases' splitting patterns and interpreted mantle dynamics here sheds light on the importance of combining local and teleseismic datasets when studying subduction zone anisotropy. It also emphasizes the need for a better understanding of the frequency dependence of splitting measurements and sensitivities of each phase. The improvements in depicting mantle flow and anisotropic structures around the globe is ever-evolving. The interpretations in this study are drawn from ray tracing in cross-sections, plotting splitting measurements on maps, other splitting and geophysical studies, and relatively simple subduction zone system cartoon models. While we are confident that our interpretations provide a good general approximation of the anisotropic structures and geodynamic processes here, the ultimate goal

would be to perform shear-wave splitting tomography in Alaska. This kind of tomography is difficult, requires major computational resources, and has only been applied twice (Abt et al., 2009; Monteiller & Chevrot, 2011). The continued improvement and growth in splitting datasets is encouraging and ought to set up the possibility for a future shear-wave splitting tomographic study in Alaska.

3.1 References

Abt, D. L., Fischer, K. M., Abers, G. A., Strauch, W., Protti, J. M., & González, V., 2009. Shear wave anisotropy beneath Nicaragua and Costa Rica: Implications for flow in the mantle wedge, *Geochem. Geophy. Geosyst.*, **10**(5), Q05S15, doi: 10.1029/2009GC002375.

Christensen, D. H. & Abers, G. A., 2010. Seismic anisotropy under central Alaska from SKS splitting observations, *J. Geophys. Res.*, **115**, B04315, doi: 10.1029/2009JB006712.

Hanna, J. & Long, M. D., 2012. SKS splitting beneath Alaska: Regional variability and implications for subduction processes at a slab edge, *Tectonophysics*, **530-531**, 272–285.

McPherson, A., Christensen, D. H., Abers, G. A., Tape, C., & Moore-Driskell, M. M., 2017. Shear Wave Splitting and Mantle Flow in Alaska, in *AGU Fall Meeting Abstracts*, vol. 2017, pp. DI43B–0365.

Monteiller, V. & Chevrot, S., 2011. High-resolution imaging of the deep anisotropic structure of the San Andreas Fault system beneath southern California, *Geophys. J. Int.*, **186**, 418–446, doi: 10.1111/j.1365-246X.2011.05082.x.

Perttu, A., Christensen, D., Abers, G., & Song, X., 2014. Insights into mantle structure and flow beneath Alaska based on a decade of observations of shear wave splitting, *J. Geophys. Res. Solid Earth*, **119**, 8366–8377, doi: 10.1002/2014JB011359.

Song, T. A. & Kawakatsu, H., 2012. Subduction of oceanic asthenosphere: Evidence from sub-slab seismic anisotropy, *Geophys. Res. Lett.*, **39**, L17301, doi: 10.1029/2012GL052639.

Song, T.-R. A. & Kawakatsu, H., 2013. Subduction of oceanic asthenosphere: A critical appraisal in central Alaska, *Earth Planet. Sci. Lett.*, **367**, 82–94.

Venereau, C., Martin-Short, R., Bastow, I., Allen, R., & Kounoudis, R., 2019. The role of variable slab dip in driving mantle flow at the eastern edge of the alaskan subduction margin: insights from sks shear-wave splitting, *Geochemistry, Geophysics, Geosystems*, doi: 10.1029/2018GC008170.